UNIVERSITY OF SOUTHAMPTON

FACULTY OF ENGINEERING AND APPLIED SCIENCES

Department of Electronics and Computer Science

Feature Extraction in Volumetric Images

by

Thamer S. Alathari

Thesis for the degree of Doctor of Philosophy

Supervisor: Prof. Mark S. Nixon

April-2015

UNIVERSITY OF SOUTHAMPTON

ABSTRACT

FACULTY OF ENGINEERING AND APPLIED SCIENCES DEPARTMENT OF ELECTRONICS AND COMPUTER SCIENCES

Computer Vision

Thesis for the degree of Doctor of Philosophy

FEATURE EXTRACTION IN VOLUMETRIC IMAGES

Thamer Alathari

The increased interest in volumetric images in recent years requires new feature extraction methods for 3D image interpretation. The aim of this study is to provide algorithms that aid the process of detecting and segmenting geometrical objects from volumetric images. Due to high computational expense, such methods have yet to be established in the volumetric space. Only few have tackled this problem using shape descriptors and key-points of a specific shape; those techniques can detect complex shapes rather than simple geometric shapes due to the well-defined key-points.

Simplifying the data in the volumetric image using a surface detector and surface curvature estimation preserves the important information about the shapes at the same time reducing the computational expense. Whilst the literature describes only the template of the three-dimensional Sobel operator and not its basis, we present an extended version of the Sobel operator, which considers the gradients of all directions to extract an object's surface, and with clear basis that allows for development of larger operators. Surface curvature descriptors are usually based on geometrical properties of a segmented object rather than on the change in image intensity. In this work, a new approach is described to estimate the surface curvature of objects using local changes of image intensity. The new methods have shown reliable results on both synthetic and on real volumetric images.

The curvature and edge data are then processed in two new techniques for evidence gathering to extract a geometrical shape's main axis or centre point. The accumulated data are taken directly from voxels' geometrical locations rather than the surface normals as proposed in literature. The new approaches

have been applied to detect a cylinder's axis and spherical shapes. A new 3D line detection based on origin shifting has also been introduced. Accumulating, at every voxel, the angles resulting from a coordinate transform of a Cartesian to spherical system successfully indicates the existence of a 3D line in the volumetric image.

A novel method based on using an analogy to pressure is introduced to allow analysis/ visualisation of objects as though they have been separated, when they were actually touching in the original volumetric images. The approach provides a new domain highlighting the connected areas between multiple touching objects. A mask is formed to detach the interconnected objects and remarkable results are achieved. This is applied successfully to isolate coins within an image of a Roman hoard of coins, and other objects. The approach can fail to isolate objects when the space between them appears to be of similar density to the objects themselves. This motivated development of an operator extended by high-pass filtering and morphological operations. This led to more accurate extraction of coins within the Roman hoard, and to successful isolation of femurs in a database of scanned body images enabling better isolation of hip components in replacement therapy.

Table of Contents

List of tables

List of figures

DECLARATION OF AUTHORSHIP

I, Thamer S. Alathari

declare that this thesis and the work presented in it are my own and has been generated by me as the result of my own original research.

Feature Extraction in Volumetric Images

I confirm that:

1. This work was done wholly or mainly while in candidature for a research degree at this University;
2. Where any part of this thesis has previously been submitted for a degree or any other qualification at this University or any other institution, this has been clearly stated;
3. Where I have consulted the published work of others, this is always clearly attributed;
4. Where I have quoted from the work of others, the source is always given. With the exception of such quotations, this thesis is entirely my own work;
5. I have acknowledged all main sources of help;
6. Where the thesis is based on work done by myself jointly with others, I have made clear exactly what was done by others and what I have contributed myself;
7. Parts of this work have been published as:
   (Abuzaina, Alathari, Nixon, & Carter, 2013; Alathari & Nixon, 2013, 2014)

Signed: Thamer S. Alathari

Date: 12-Dec-2014

Acknowledgements

To my advisor, teacher and friend professor Mark Nixon thank you. My greatest gratitude for your care, time and support. I am very glad that my academic research journey starts with you.

Stress and pressure are always major factors in any degree study, however thanks to the Public Authority for Applied Education and Training (PAAET) in Kuwait and their generous funding a large load has been lifted and for that I am very thankful.

My father, you will always be in my mind, in my memories, and resting in my heart. My mother, my first love, thank you for being there beside me and I hope my weekly interruption of your favourite program does not bother you. All I want is to see you healthy and happy. My lovely wife, thank you for keeping up with my mood swings and improving my life, it is now much happier and much easier with you, it is an absolute joy to spend my life with you. My passed away brother Fathi, your smile and your incredible sense of humour still live with me. My brothers Fawaz, Haitham, Naser and Yousef, My sisters Sausan and Aisha, I miss each and every single one of you. My Nephew Saleh, I still cannot believe that you are married now!

My colleagues, Anas Abuzaina, Mus'ab Sahrim and Ari Rheum, thank you for the small talks we have between every now and then throughout the day, it is great to feel human again after being a zombie for few hours.

Chapter 1: Background

1.1 Context

The use of automatic detection of geometric objects in two-dimensional space (2D) has been given much attention in the recent years due to the rapid increase in computer power, availability of high performance sensors and the low cost of memory. On the other hand, the three-dimensional (3D) space lacks such techniques. The current increase of interest in the 3D imaging systems heightened the need for these techniques. In recent years, there has been much development on them especially the computed tomography scanners (CT) in fields such as health, national safety, archaeology and industrial sectors.

There is a dedicated centre for CT scanning services called Muvis (Muvis, 2014) at the University of Southampton, which is available to support the multiple disciplines offered by the university. The centre is an example for the current popularity due to the valuable information provided by such modality. In Figure 1.1, a CT scanned jar full with ancient Roman coins (Franklin, 2012) is derived from collaborative work between the Muvis centre and the archaeology department by giving researchers the ability to identify findings using a non-destructive imaging method.

The major benefit of using CT scanners resides in the increased amount of the qualitative and quantitative information provided compared to standard 2D sectional images (Russ, 2006). Such information could be valuable for the current advances in science applications such as 3D printing of organs or choosing a properly sized implant. However, the scanners produce intensity volumetric images that are large in terms of memory size and suffer from noise and some variant artefacts. The images require pre-processing to prepare them for object extraction. Another major problem in the volumetric images is the large amount of orientation and location possibilities for the

object in 3D space. Figure 1.1 gives an excellent example of a complex case where many objects exist in the scene with different orientations.

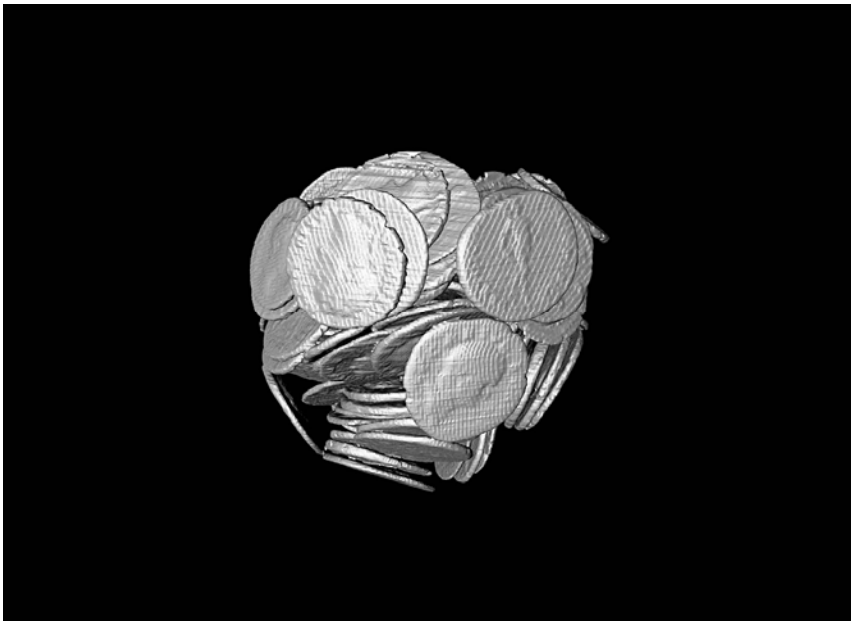

Figure 1.1 CT scan of a jar filled with ancient roman coins

Much current research focuses on finding objects in 2.5D data, given the proliferation of Kinect devices and laser scanners providing point cloud images (Rabbani & Heuvel, 2005; Camurri, Vezzani, & Cucchiara, 2014). The availability of such devices at a low cost made them popular in the in past few years. Those devices provide a view of the surface whereas a volumetric image shows can reveal internal content. Some research has tended to focus on the automatic extraction of objects from volumetric images (Krcah, Szekely, & Blanc, 2011a; Wang, Gillibert, Flin, & Coeurjolly, 2012).

Beyond the techniques already described, there appears little work in the extension of planar image operators to volumetric images. This is noted in one recent work (Gregory Flitton, Breckon, & Megherbi, 2010), which extends the SIFT operator to volumetric images and (Knopp, Prasad, Willems, Timofte, & Van Gool, 2010), which also extends the Speeded Up Robust Features (SURF) detection to 3D in conjunction with Hough transform to classify 3D shapes. The absence of available technique might arise due to the fact that many expositions of planar images omit a theoretical basis for the techniques whereas the basis is actually available (M. Nixon & Aguado, 2012) as will be discussed in the next chapter. It is of note that this applies to the Sobel edge

detection operator, though the Wikipedia entry (Wikipedia, 2012) describes the Sobel as a volumetric operator, this is little found in the literature (Y. J. Zhang, 1993; Wählby & SINTORN, 2004; Palu, He, & Lu, 2006; Avinash, 2009) and these works only describe a *3x3x3* operator, without further details. The same is also correct in the case of 3D curvature extraction based on light intensity, which is essential for making use of the information provided by the image scanner instead of relying on a surface provided by edge or segmentation method.

More modern approaches to image analysis deploy interest point detection with machine learning, especially for tasks such as image retrieval and recognition by image content (Greg Flitton, Mouton, & Breckon, 2015). Volumetric scans are principally used in the area of engineering sciences and thus often deployed for measurement purposes. The modern approaches to image analysis appear less suited to implementation in this manner given not only the volume of the data, but also the reliance on databases for analysis of performance. Currently, 3D volumetric scanning has only just reached a point where automated scanning of multiple objects can be achieved. The difficulty of segmenting and identifying multiple geometrical shapes increases with change in their parameters, location and orientation in the volumetric image. A more established image interpretation approach appears suitable, using properties that can be directly attributed to image content and directly related to the underlying nature and arrangement of the shapes contained within the volumetric scan, and which can address and reduce the data storage and processing consistent with volumetric scanning.

This thesis will describe new approaches to low-level and high-level 3D volumetric image interpretation. The low-level operations concern surface detection and surface curvature estimation; the high-level operations concern shape detection and shape analysis. Since there is not yet a plethora of established work in each of these fields, we shall describe the prior work to each in tandem with the new approaches, rather than consolidate the material here.

1.2 Contributions

The main contributions of this thesis are:

i. A method for 3D volumetric-image edge extraction based on extension of the Sobel operator to three dimensions.
ii. Estimation of curvature again by extension of a standard 2D approach to three dimensions in volumetric images.
iii. Development of evidence gathering methods based on Hough transform to detect lines, spheres and cylindrical objects based on voxel information rather than surface normals.
iv. A new approach to separate touching objects in volumetric scans. This is based on using an analogy to pressure as an image operator, which appears totally new to image analysis.

The Sobel edge detector is simple and efficient, which makes it an ideal candidate for surface detection. By extending 2D theory (M. Nixon & Aguado, 2012; Sobel, 2014a), we can achieve a new 3D approach. The new Sobel templates address the increase in dimensionality by taking into account the gradient value and direction of every dimension of the three dimensions for every voxel. As a result, the proposed templates have reliably extracted the surface of the objects in the volumetric images.

The calculated gradients from the new Sobel operator are later employed in a new method for curvature estimation based on (Kass, Witkin, & Terzopoulos, 1988). The new curvature estimation is based on the set of surface gradients rather than faces and vertices resulted from thresholded edge operator and marching cube algorithm. The curvature outcome can be used to add more detail into the object description to help minimise the information to be processed by removing undesirable data within the volume.

Three new evidence-gathering techniques based on Hough transform are presented to overcome the dependence on surface normal (Bhattacharya, Liu, Rosenfeld, & Thompson, 2000; Rabbani & Heuvel, 2005; Ogundana, Coggrave, Burguete, & Huntley, 2007). The first technique is called a template searcher

that uses a spherical template to look for evidence of existence of a cylinder axis or a sphere. The other technique is called point-sphere searcher, which is an extension of an earlier Hough transform for detecting circles (Illingworth & Kittler, 1987). A comparison is made between the two techniques in terms of speed and accuracy. The last technique is a new line detection algorithm based on origin shifting. The new method is similar to (Bhattacharya et al., 2000) but with a new approach where voxel perspective is changed to describe lines in volumetric images including the length parameter with tolerance to gaps. The literature lacks such technique even though it is very well established in the 2D image world (Duda & Hart, 1972; Illingworth & Kittler, 1987).

Finally, a novel approach to separate touching objects in 3D space is elucidated. A physical analogy similar to the proposed in (Mark S Nixon, Liu, Direko, & Hurley, 2009) has been used to liken a small cubic of the volumetric image background to a cube filled with ideal gas. The ideal gas would exert a pressure on the object of interest with an inverse relation with the volume of the background, which helps in creating a new domain called the pressure domain, which is used to form a mask that is employed to separate connected objects. Using mapping and edge information to achieve improved results has enhanced the method. The results have been compared with the manually segmented data and full analysis on the results has been presented.

The structure of this thesis is to expose these areas of contributions in separate chapters. As each of these chapters covers a major area of contribution, the literature review material is to be found in each chapter, rather than collated as a single literature review. This research has already led to one workshop and two conference papers listed below and some papers that are in preparation.

- Anas Abuzaina, Thamer Alathari, Mark S. Nixon, Detecting Moving Spheres in 3D Point Clouds via the 3D Velocity Hough, 11th IEEE IVMSP Workshop: 3D Image/Video Technologies and Applications, June 2013.

- Thamer Alathari, Mark S. Nixon, Segmenting Objects in 3D Images by Volumetric Analysis, Proc. ISVC 2013, LNCS, 8033, September 2013.

- Thamer Alathari, Mamadou Bah, Mark S. Nixon, Femur Bone Segmentation using a Pressure Analogy, 22nd International Conference on Pattern Recognition, August 2014.

Chapter 2: Low Level Feature Extraction

2.1 Surface Detection

Edge detection is a fundamental image processing operation, which extracts valuable information hidden within the borders of an object. The process is conventionally formulated in two-dimensional space to analyse planar images. It delivers simplified analysis of images by dramatically reducing the amount of data to be processed. The strength of detected edges is represented by the rate of change in image intensity between a pixel and its surrounding window. The gradients are calculated in every dimension by a specific template or equation describing the rate of change of intensity. Edge detection does not require prior knowledge about the shape and depends mainly on the local features.

There are many standard edge detection operators such as Prewitt, Sobel and Canny (Russ, 2006). The Sobel operator (Sobel, 1970, 2014b) is now in routine use in image analysis, though its development appears obscure. As such this Chapter repeats some basic material, which appears standard in 2D image analysis and then extends it for use in 3D image analysis, to make clear the precise nature of the operators used as a basis for later developments.

Two-dimensional operators have been applied to three-dimensional volumetric images without consideration for the third dimension, since the approximation appeared to yield satisfactory results (Zhu, Cochoff, & Sukalac, 2012). The problem with this approximation is the omission of the information that can be derived from a volume rather than from a plane (Yu-Qian, Wei-Hua, Zhen-Cheng, Jing-Tian, & Ling-Yun, 2005). A 3D operation considers edges to be surfaces whereas a 2D approximation depends on its plane of action; surface detection is independent of the direction and can give more reliable information for later processing.

There are several edge detectors in literature, which deal with surface detection using different approaches such as deformable model (Ma, Tavares, Jorge, & Mascarenhas, 2010), contour reconstruction (Cong & Parvin, 2001) and 3D edge operators (Brejl & Sonka, 2000). The most frequently used are the 3D edge operators due to their relative balance between memory demand and accuracy. Some of the operators provided by literature (Palu et al., 2006; Avinash, 2009; Itk.org, 2014) lack the rationale underlying the selection of the template coefficients.

This section extends the basics of the 2D Sobel edge operator to deliver a new 3D surface operator that is simple, non-recursive and less demanding in terms of memory. Later in this chapter we also extend an established curvature operator to provide a new 3D operator, which is again an extension of 2D material to precisely define the 3D operator, which is used later in this thesis.

2.1.1 Sobel Operator

Sobel is a first-order edge detection operator, which consists of two template masks to calculate the vertical and the horizontal gradients (Figure 2.1). The creation of the templates is based on smoothing in one direction and differencing in the other, usually given as:

$$\begin{bmatrix} 1 & 0 & -1 \\ 2 & 0 & -2 \\ 1 & 0 & -1 \end{bmatrix} \qquad \begin{bmatrix} 1 & 2 & 1 \\ 0 & 0 & 0 \\ -1 & -2 & -1 \end{bmatrix}$$

(a) (b)

Figure 2.1 Sobel 3x3 templates (a) Horizontal Gradient Template and (b) Vertical Gradient Template.

Pascal's triangle forms a basis for calculating of the template coefficients for smoothing and differencing (M. Nixon & Aguado, 2012). For a window size of 3, Pascal's triangle results in two vectors: one for smoothing (Eqn. 2.1) and another for differencing (Eqn. 2.2).

$$\boldsymbol{Smoothing\ Vector} = [\mathbf{1} \quad \mathbf{2} \quad \mathbf{1}] \tag{2.1}$$

$$\boldsymbol{Differencing\ Vector} = [\mathbf{1} \quad \mathbf{0} \quad \mathbf{-1}] \tag{2.2}$$

Larger operators can be derived in this way. The templates in Figure 2.1 have been created using the two vectors in equations Eqn. 2.1 and Eqn. 2.2. The horizontal gradient template creation takes place by smoothing the vertical direction perpendicular to the derivative direction and difference in the derivative direction and vice versa for the vertical template Figure 2.2.

Horizontal Template (*x*-axis)= Smooth *y* * difference *x*

$$= \begin{bmatrix} 1 \\ 2 \\ 1 \end{bmatrix} * \begin{bmatrix} 1 & 0 & -1 \end{bmatrix} = \begin{bmatrix} 1 & 0 & -1 \\ 2 & 0 & -2 \\ 1 & 0 & -1 \end{bmatrix} \quad \text{(a)}$$

Vertical Template (*y*-axis)= difference *y* * smooth *x*

$$= \begin{bmatrix} 1 \\ 0 \\ -1 \end{bmatrix} * \begin{bmatrix} 1 & 2 & 1 \end{bmatrix} = \begin{bmatrix} 1 & 2 & 1 \\ 0 & 0 & 0 \\ -1 & -2 & -1 \end{bmatrix} \quad \text{(b)}$$

Figure 2.2 Creating Sobel templates (a) Horizontal Template [*x*-axis] , (b) Vertical Template [*y*-axis]

The templates are then convolved with the image to give two components at every pixel: gradient in the vertical direction $\boldsymbol{G_y}$ and gradient in the horizontal direction $\boldsymbol{G_x}$. Those gradients are then used to calculate the gradient vector magnitude Eqn. 2.3 and its direction Eqn. 2.4 as in Figure 2.3

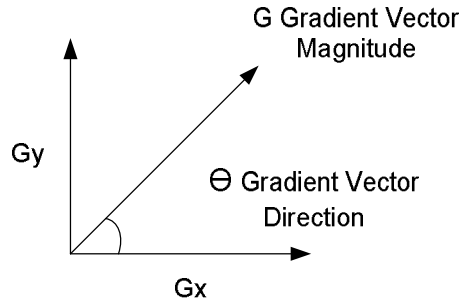

Figure 2.3 Vector notation of the 2D gradient vector

$$\boldsymbol{G = \sqrt{G_x^2 + G_y^2}} \quad \textbf{where } \boldsymbol{G \textit{ is the gradient magnitude}} \qquad 2.3$$

$$\boldsymbol{\theta = tan^{-1}\left(\frac{G_y}{G_x}\right)} \quad \textbf{where } \boldsymbol{\theta \textit{ is the gradient direction}} \qquad 2.4$$

2.1.1 Surface Operator

The Sobel operator can be extended to three dimensions to operate on voxel data. Voxel data is a stack of cross-sectional image slices taken using a CT scan of a scene, or object. The creation of the volume template is derived from smoothing and differencing operations with the consideration of the new additional dimension. The main concept remains the same, difference the investigated dimension and smooth the other two (as shown in Figure 2.5), resulting in three templates.

The templates are then convolved with the three dimensional data at each voxel. The gradient vector magnitude and angles are then calculated as shown in Figure 2.4 using Eqn. 2.5 and Eqn. 2.6

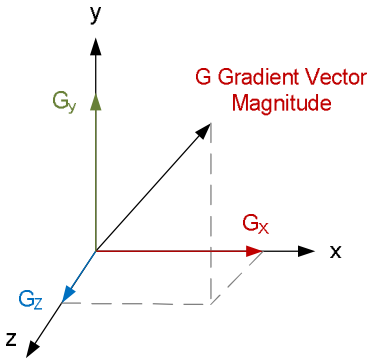

Figure 2.4 Vector notation of the 3D gradient vector

$$\mathbf{G} = \sqrt{\mathbf{G}_x^2 + \mathbf{G}_y^2 + \mathbf{G}_z^2} \qquad 2.5$$

$$\boldsymbol{\beta} = \boldsymbol{tan}^{-1}\left(\frac{\boldsymbol{G_x}}{\boldsymbol{G_z}}\right); \quad \boldsymbol{\gamma} = \boldsymbol{tan}^{-1}\left(\frac{\boldsymbol{G_z}}{\boldsymbol{G_y}}\right); \quad \boldsymbol{\alpha} = \boldsymbol{tan}^{-1}\left(\frac{\boldsymbol{G_y}}{\boldsymbol{G_x}}\right) \qquad 2.6$$

As with the planar Sobel operator, larger volumetric Sobel operators can be derived by extension of Pascal's triangle in the manner of Eqn. 2.1 and 2.2.

a) The gradient in the x-direction

$$G_x = Smooth_y \cdot Difference_x \cdot Smooth_z$$

$$= \begin{bmatrix}1\\2\\1\end{bmatrix}.[-1 \quad 0 \quad 1].\begin{bmatrix}1\\2\\1\end{bmatrix} = \begin{bmatrix}-1 & 0 & 1\\-2 & 0 & 2\\-1 & 0 & 1\end{bmatrix}.\begin{bmatrix}1\\2\\1\end{bmatrix} \leftarrow \text{z-direction scalar}$$

$$= \begin{cases} \begin{bmatrix}-1 & 0 & 1\\-2 & 0 & 2\\-1 & 0 & 1\end{bmatrix} * 1 \rightarrow \begin{bmatrix}-1 & 0 & 1\\-2 & 0 & 2\\-1 & 0 & 1\end{bmatrix} \\ \begin{bmatrix}-1 & 0 & 1\\-2 & 0 & 2\\-1 & 0 & 1\end{bmatrix} * 2 \rightarrow \begin{bmatrix}-2 & 0 & 2\\-4 & 0 & 4\\-2 & 0 & 2\end{bmatrix} \\ \begin{bmatrix}-1 & 0 & 1\\-2 & 0 & 2\\-1 & 0 & 1\end{bmatrix} * 1 \rightarrow \begin{bmatrix}-1 & 0 & 1\\-2 & 0 & 2\\-1 & 0 & 1\end{bmatrix} \end{cases}$$

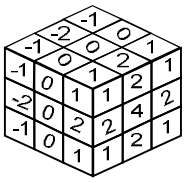

The resulting template for calculating G_x

b) The gradient in the y-direction

$$G_y = Difference'_y.Smooth_x\,.Smooth'_z$$

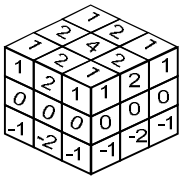

The resulting template for calculating G_y

c) The gradient in the z-direction

$$G_z = Smooth'_y.Smooth_x\,.Difference'_z$$

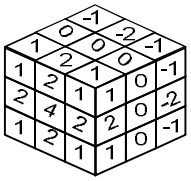

The resulting template for calculating G_z

Figure 2.5 Sobel operator templates used to calculate gradient in (a) x-direction, (b) y-direction, and (c) z-direction.

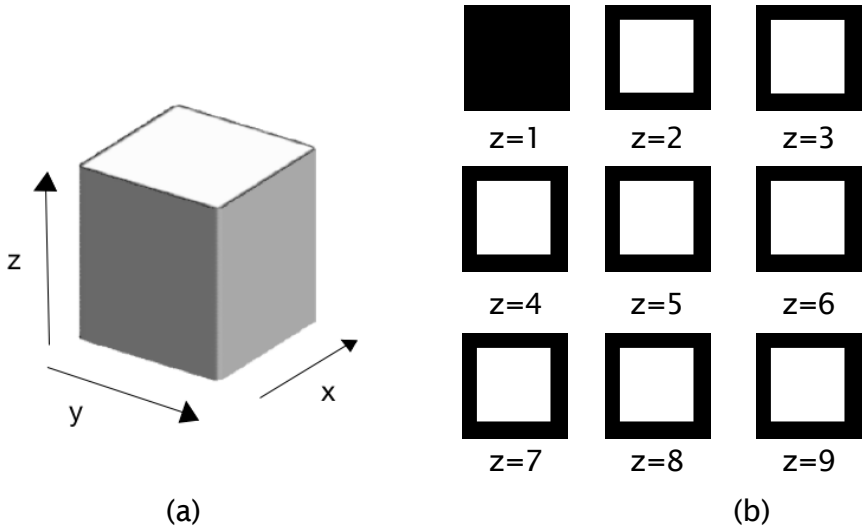

Figure 2.6 Synthetic cube (a) Rendered cube, (b) The first 9 image slices through the cube volume

2.1.2 Application

The 2D Sobel operator does not take into account the change or the gradient in the direction normal to the plane where the 2D Sobel is applied. On the other hand, using the operator described above, all the dimensions were considered in the process of gradient calculation and proper description for the edge information was calculated. Consider the synthetic cube in Figure 2.6 that would be an ideal simple example to validate the proposed method. Applying the 2D operator to the cube would result in slices in Figure 2.7a that have omitted the top surface. On the other hand, the volumetric operator preserves the top surface as in Figure 2.7b, which implies that the 3D Sobel operator correctly preserves object surfaces.

A CT scanned engine block (Figure 2.8) has been examined to show the validity of the proposed operator on a CT volumetric image. The results were compared to the 2D Sobel operator, as mentioned earlier the proposed method considered the effect of increased dimensionality by preserving the top plane of the engine as in Figure 2.9. Please note the 2D Sobel result have been processed with skeletonization to obtain thin edges, on the other hand, the same can not be done for the 3D Sobel operator due to the effect of skeletonization in 3D space.

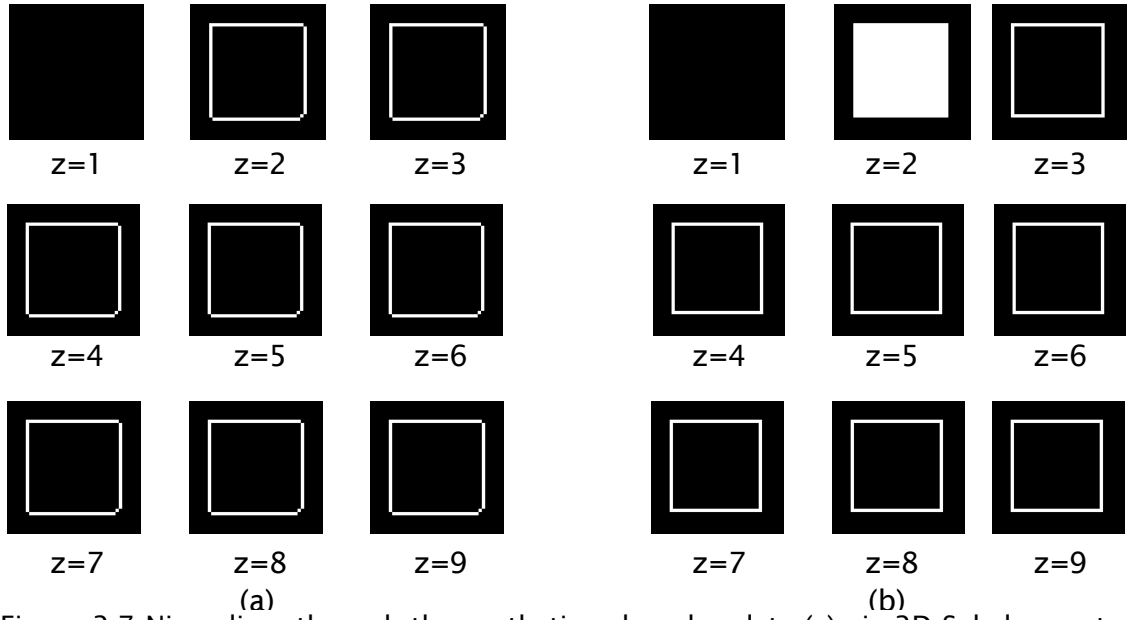

Figure 2.7 Nine slices through the synthetic cube edge data (a) via 2D Sobel operator and (b) via 3D surface operator.

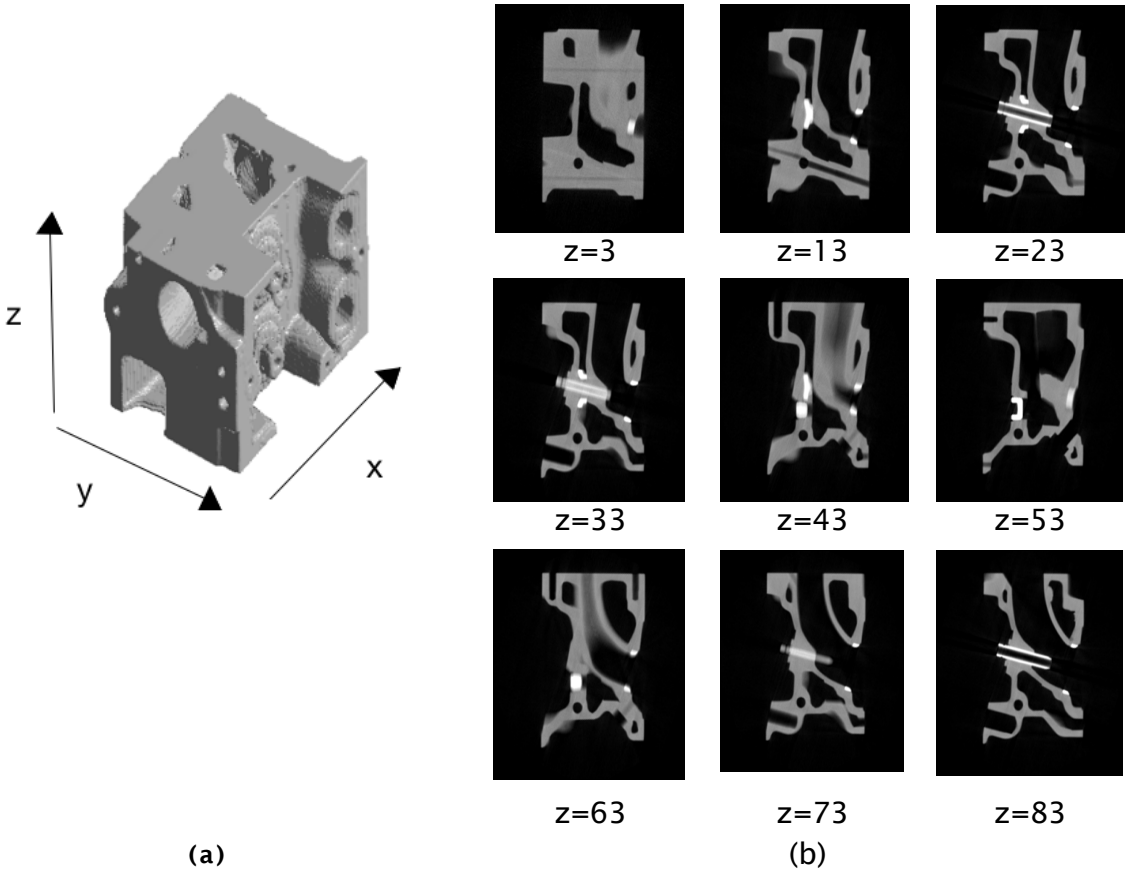

Figure 2.8 CT scan of block engine (a) 3D render, (b) Nine slices through the block engine volume

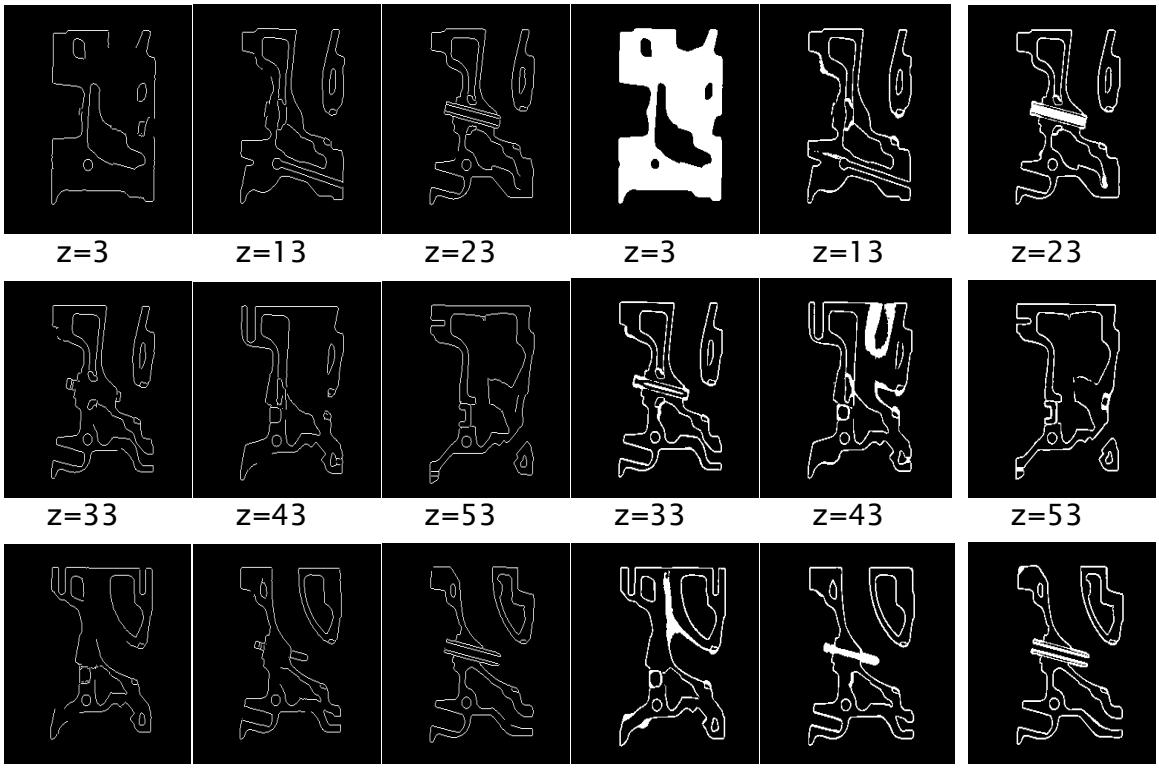

Figure 2.9 Nine slices through the block engine edge data (a) via 2D Sobel operator and (b) via 3D surface operator

By this, a new 3D Sobel operator, suited to application on volumetric images and which has a basis consistent with the formulation of the original 2D operator, which successfully detects surfaces rather than edge.

2.2 On Deriving Estimates of Curvature from Image and Volume Data

Curvature is another important property that helps to reveal important information about a shape, especially in images of the built environment, and has seen much development in literature. The most popular methods rely on geometrical analysis of shape surface to give every vertex a curvature value (M. P. Do Carmo, 1976; Stevens, 1981). The curvature components in this relation are mainly based on the projections of the segmented object in 3D space.

In order for those approaches to work, a prior segmentation is required. Usually two steps have to be performed on the CT image; surface detection

and marching cubes. The curvature values are extracted geometrically based on the faces and vertices rather than local change in image intensity gradients (Gao, Wu, Mao, & Wang, 2014). The use of the gradients would provide direct curvature estimation but the lack of curvature descriptor based on the gradients presents an obstacle.

Here we extend a basic approach, which derives planar curvature from 2D image data similar to the one introduced by (Kass et al., 1988), to provide a new approach, which derives curvature by a 3D volumetric operator, so that corners can be detected in surfaces. Unlike previous works that estimate curvature from projected range image (Colombo et al. 2006) or from the geometric properties, the new operator is applied directly to the 3D volume. The simplest definition of curvature is the ratio of the change of tangential angle $d\varphi(t)$ to the change in arc length $ds(t)$.

$$\boldsymbol{k(t) = \frac{d\varphi(t)}{ds(t)}} \qquad 2.7$$

To study the curvature definition more closely, let the parametric equation of a point in an image be represented by the following location vector:

$$\boldsymbol{s(t) = x(t) + y(t)} \quad \text{where } \mathbf{x} \text{ and } \mathbf{y} \text{ present location at time } \mathbf{t} \qquad 2.8$$

Consider that this point is moving in the image then the change in the position is:

$$\boldsymbol{\frac{ds(t)}{dt} = \frac{dx(t)}{dt} + \frac{dy(t)}{dt}} \qquad 2.9$$

The magnitude of this change in location is given by:

$$\boldsymbol{\left\| \frac{ds(t)}{dt} \right\| = \sqrt{\frac{dx(t)^2}{dt} + \frac{dy(t)^2}{dt}} = \sqrt{x'^2 + y'^2}} \qquad 2.10$$

The angle of the location vector is given by:

$$\boldsymbol{\varphi(t) = \tan^{-1}\left(\frac{dy(t)}{dx(t)}\right) = \tan^{-1}\left(\frac{y'}{x'}\right)} \qquad 2.11$$

And

$$\frac{d\varphi(t)}{dt} = \frac{x'y'' + y'x''}{x'^2 + y'^2} \qquad 2.12$$

By substituting Eqn. 2.10 and Eqn. 2.12 into Eqn. 2.7, the following definition for the curvature k is obtained:

$$k(t) = \frac{x'y'' + y'x''}{(x'^2 + y'^2)^{\frac{3}{2}}} \qquad 2.13$$

2.2.1 Planar curvature detection from image intensity

Curvature detection using image intensity values is based on detecting the angular changes in the image. Representing a curve as

$$x(t) = x + t\cos(\varphi(x,y)); \quad y(t) = y + t\sin(\varphi(x,y)) \qquad 2.14$$

where x and y present location at time t

The change in direction in relation to the magnitude

$$k(t) = \frac{d\varphi(x,y)}{ds(x,y)} = \left(\frac{d\varphi(x,y)}{dx}\cdot\frac{dx(x)}{dt} + \frac{d\varphi(x,y)}{dy}\cdot\frac{dy(t)}{dt}\right) \Big/ \left(\frac{ds(x,y)}{dx}\cdot\frac{dx(x)}{dt} + \frac{ds(x,y)}{dy}\cdot\frac{dy(t)}{dt}\right) \qquad 2.15$$

And

$$\frac{x(t) - x}{t} = cos(\varphi(x,y)); \quad \frac{y(t) - y}{t} = sin(\varphi(x,y)) \qquad 2.16$$

By substituting Eqn. 2.16 in Eqn. 2.15.

$$k(x,y) = \frac{\left(\frac{d\varphi(x,y)}{dx}\cos(\varphi(x,y)) + \frac{d\varphi(x,y)}{dy}\sin(\varphi(x,y))\right)}{\left(\frac{ds(x,y)}{dx}\cos(\varphi(x,y)) + \frac{ds(x,y)}{dy}\sin(\varphi(x,y))\right)} \qquad 2.17$$

Using the gradients:

$$\cos(\varphi(x,y)) = \frac{-My}{\sqrt{Mx^2 + My^2}}; \quad \sin(\varphi(x,y)) = \frac{Mx}{\sqrt{Mx^2 + My^2}} \qquad 2.18$$

Where $\boldsymbol{Mx}$ is the gradient in the x-axis direction

Where $\boldsymbol{My}$ is the gradient in the y-axis direction

Then

$$\frac{\boldsymbol{d}}{\boldsymbol{dx}}\boldsymbol{tan}\big(\boldsymbol{\varphi}(\boldsymbol{x},\boldsymbol{y})\big) = \boldsymbol{sec}^{\boldsymbol{2}}\big(\boldsymbol{\varphi}(\boldsymbol{x},\boldsymbol{y})\big).\frac{\boldsymbol{d}}{\boldsymbol{dx}}\,\boldsymbol{\varphi}(\boldsymbol{x},\boldsymbol{y}) \tag{2.19}$$

So

$$\frac{\boldsymbol{d}}{\boldsymbol{dy}}\,\boldsymbol{\varphi}(\boldsymbol{x},\boldsymbol{y}) = \frac{-\boldsymbol{My}\frac{\boldsymbol{dMx}}{\boldsymbol{dy}} + \boldsymbol{Mx}\frac{\boldsymbol{dMy}}{\boldsymbol{dy}}}{\boldsymbol{My}^{\boldsymbol{2}} + \boldsymbol{Mx}^{\boldsymbol{2}}} \tag{2.20}$$

By substitution,

$$\boldsymbol{k}(\boldsymbol{x},\boldsymbol{y}) = \frac{\frac{\boldsymbol{1}}{(\boldsymbol{My}^{\boldsymbol{2}} + \boldsymbol{Mx}^{\boldsymbol{2}})^{\frac{\boldsymbol{3}}{\boldsymbol{2}}}} \cdot \left[\boldsymbol{My}^{\boldsymbol{2}}\frac{\boldsymbol{dMx}}{\boldsymbol{dx}} + \boldsymbol{MxMy}\frac{\boldsymbol{dMy}}{\boldsymbol{dx}} - \boldsymbol{MyMx}\frac{\boldsymbol{dMx}}{\boldsymbol{dy}} + \boldsymbol{Mx}^{\boldsymbol{2}}\frac{\boldsymbol{dMy}}{\boldsymbol{dy}}\right]}{\sqrt{\left(\frac{-\boldsymbol{My}}{\sqrt{\boldsymbol{Mx}^{\boldsymbol{2}} + \boldsymbol{My}^{\boldsymbol{2}}}}\right)^{\boldsymbol{2}} + \left(\frac{\boldsymbol{Mx}}{\sqrt{\boldsymbol{Mx}^{\boldsymbol{2}} + \boldsymbol{My}^{\boldsymbol{2}}}}\right)^{\boldsymbol{2}}}} \tag{2.21}$$

Eqn. 2.21 defines the curvature using image gradients extracted from intensity image (M. Nixon & Aguado, 2012).

2.2.2 Surface curvature detection from volumetric data

For 3D, we have three plane projections for every point.

For the x-y plane: $x(t) = x + t\,cos\big(\varphi(x,y)\big);\quad y(t) = y + t\,sin\big(\varphi(x,y)\big)$

For the x-z plane: $x(t) = x + t\,cos\big(\varphi(x,z)\big);\quad z(t) = z + t\,sin\big(\varphi(x,z)\big)$

For the z-y plane: $z(t) = z + t\cos\big(\varphi(z,y)\big);\quad y(t) = y + t\sin\big(\varphi(z,y)\big)$

The three dimensional curvature can be found using the following equations:

$$k(x,y) = \frac{\frac{1}{(My^2 + Mx^2)^{\frac{3}{2}}} \cdot \left[My^2 \frac{dMx}{dx} + MxMy\frac{dMy}{dx} - MyMx\frac{dMx}{dy} + Mx^2\frac{dMy}{dy}\right]}{\sqrt{\left(\frac{-My}{\sqrt{Mx^2 + My^2}}\right)^2 + \left(\frac{Mx}{\sqrt{Mx^2 + My^2}}\right)^2}} \quad 2.22$$

$$k(x,z) = \frac{\frac{1}{(Mz^2 + Mx^2)^{\frac{3}{2}}} \cdot \left[Mz^2 \frac{dMx}{dx} + MxMz\frac{dMz}{dx} - MzMx\frac{dMx}{dz} + Mx^2\frac{dMz}{dz}\right]}{\sqrt{\left(\frac{-Mz}{\sqrt{Mx^2 + Mz^2}}\right)^2 + \left(\frac{Mx}{\sqrt{Mx^2 + Mz^2}}\right)^2}} \quad 2.23$$

$$k(z,y) = \frac{\frac{1}{(My^2 + Mz^2)^{\frac{3}{2}}} \cdot \left[My^2 \frac{dMz}{dz} + MzMy\frac{dMy}{dz} - MyMz\frac{dMz}{dy} + Mz^2\frac{dMy}{dy}\right]}{\sqrt{\left(\frac{-My}{\sqrt{Mz^2 + My^2}}\right)^2 + \left(\frac{Mz}{\sqrt{Mz^2 + My^2}}\right)^2}} \quad 2.24$$

The final magnitude of the curvature has been as a Euclidean sum:

$$\boldsymbol{Curvature} = \sqrt{k(x,y)^2 + k(x,z)^2 + k(z,y)^2} \quad 2.25$$

The curvature in this context is defined by the rate of change in the angular movement of a voxel to the rate of change in speed in that same direction for every projection as illustrated in Figure 2.10

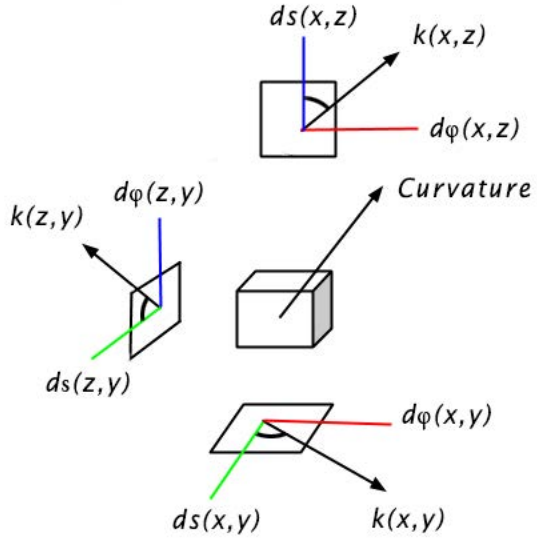

Figure 2.10 The curvature magnitude and the curvature components $\boldsymbol{k}(\boldsymbol{x},\boldsymbol{y})$, $\boldsymbol{k}(\boldsymbol{x},\boldsymbol{z})$ and $\boldsymbol{k}(\boldsymbol{z},\boldsymbol{y})$ projected on planes.

2.2.3 Application of the 3D surface curvature detection

The effectiveness of 3D curvature can be visualized by application to the synthetic cube of Figure 2.6. The result of applying curvature detection is shown in Figure 2.11a, this figure shows all the resulted curvature values. The window in which the gradients were measured introduced smaller curvature values around the sharp edges of the cube. A histogram of normalized curvature values is created to investigate the curvature strengths (the higher values mean higher curvature) Figure 2.11b. In Figure 2.11c, the corners of the cube were extracted successfully by choosing a proper threshold value using the histogram.

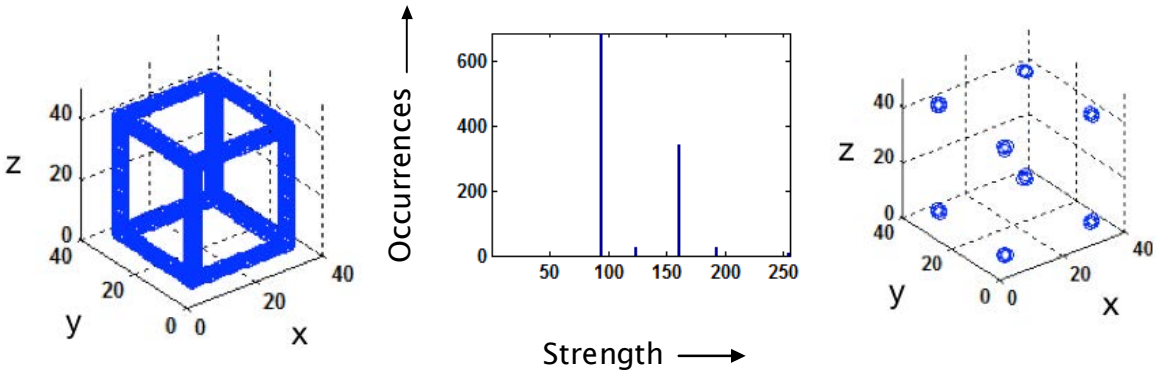

(a) (b) (c)

Figure 2.11 Curvature detection method on synthetic cube in Figure 2.6, (a) Direct result from the curvature, (b) Histogram shows the curvature occurrences according to strength and (c) After thresholding.

As the curvature extracted from the image gradient and the change of the gradient, the curvature values will be mainly be controlled by the image intensity. The part of the image where the change of intensity is high will get high curvature value as it will be identified as higher priority and will be assigned a higher curvature values than another part of the image with lower change values.

The components of the curvature magnitude, $k(x,y)$, $k(x,z)$ and $k(y,z)$ of four slices of the coin data of Figure 1.1 are shown in Figure 2.12, each shows the

curvature estimation on one plane out of the three in 3D space. The thresholded results Figure 2.13 were able to identify the surface areas where the coins are curved, which is an abstract description of the coin that is also the desired outcome to prepare the data for later processing.

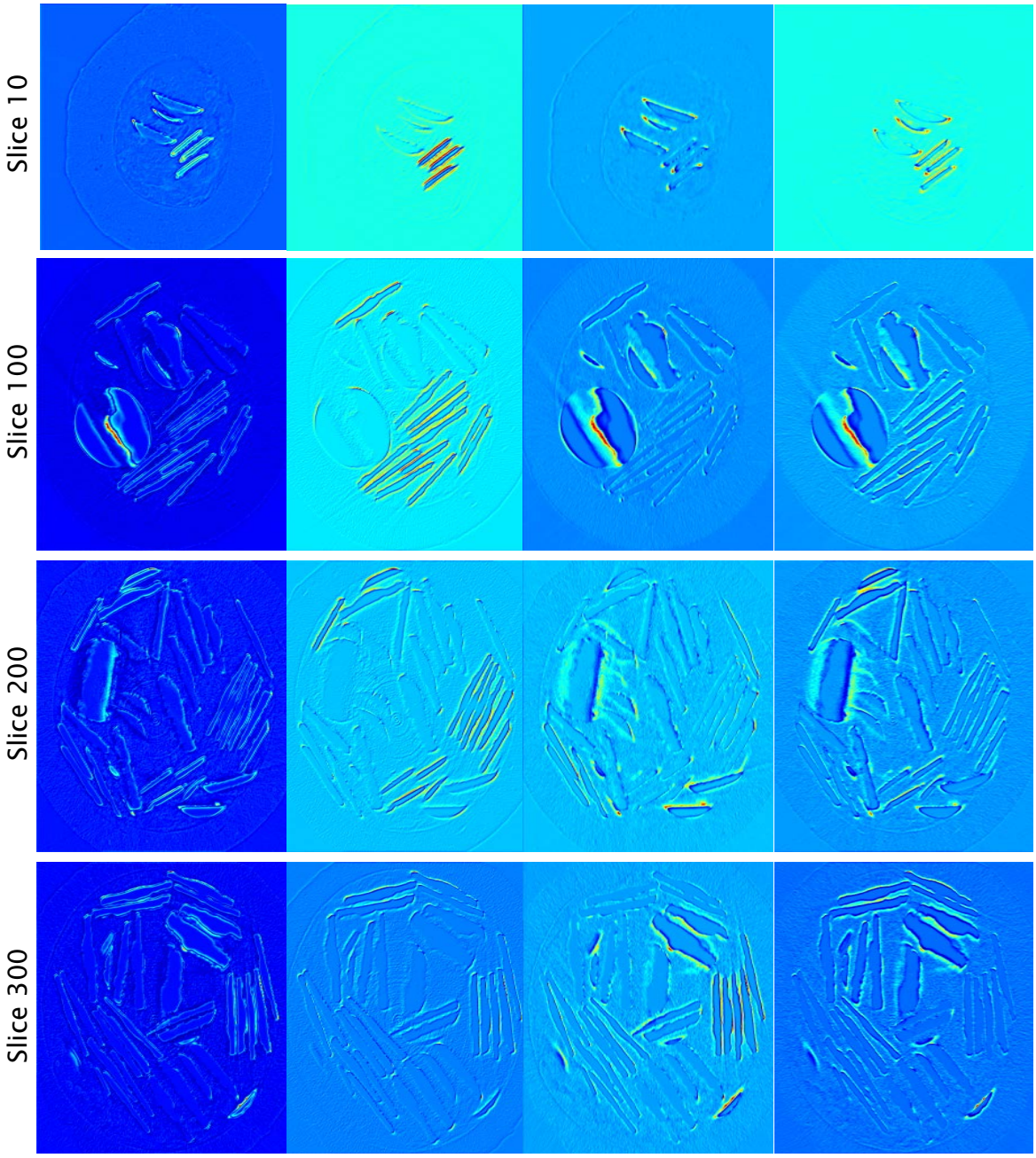

(a) Curvature Magnitude (b) $\boldsymbol{k}(\boldsymbol{x},\boldsymbol{y})$ (c) $\boldsymbol{k}(\boldsymbol{x},\boldsymbol{z})$ (d) $\boldsymbol{k}(\boldsymbol{y},\boldsymbol{z})$

Figure 2.12 Four slices through the coins in Figure 1.1 showing the curvature magnitude (a) and the curvature components $\boldsymbol{k}(\boldsymbol{x},\boldsymbol{y})$, $\boldsymbol{k}(\boldsymbol{x},\boldsymbol{z})$ and $\boldsymbol{k}(\boldsymbol{y},\boldsymbol{z})$ (b-d) respectively, for each slice.

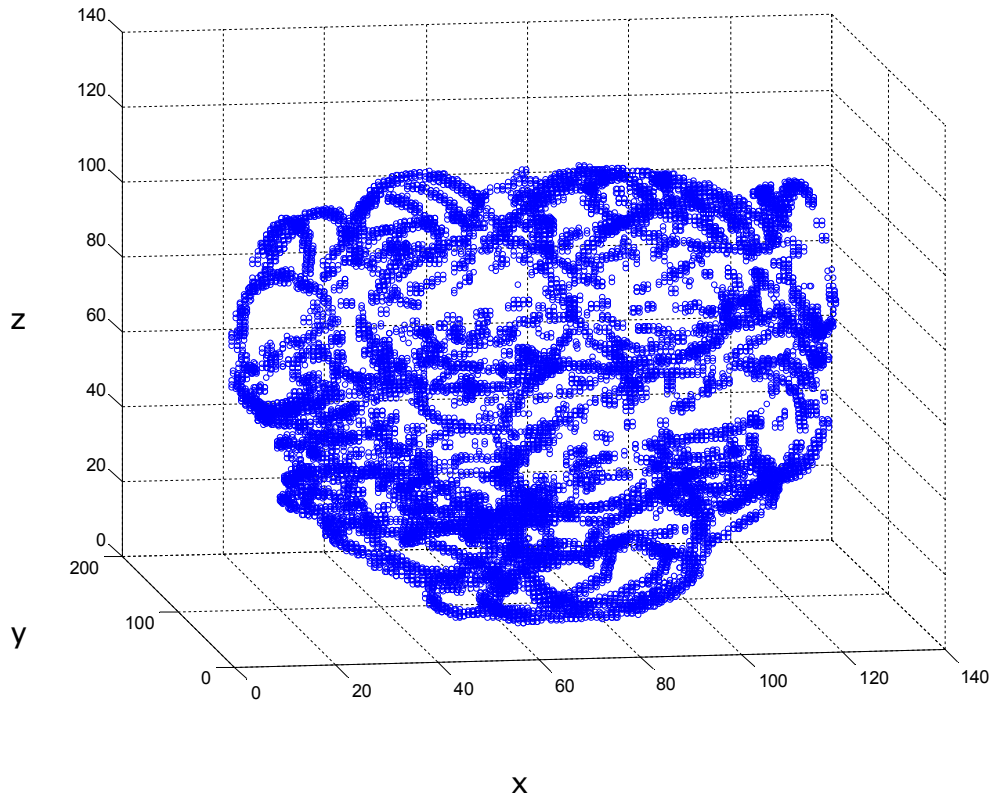

Figure 2.13 Thresholded curvature using the proposed curvature estimation of the data in Figure 1.1, showing the surface areas where the coins are curved.

Analysis of the effect of random noise is presented in Figure 2.14. The noise has been generated by random number from a normal distribution with a mean of 0.5 and standard deviations ranging from .05 to 0.2 with an increment of .05. It is then added to the image of (Figure 2.8) and normalized. The curvature magnitude is then calculated to study the effect of noise on the curvature data; a single slice from the volume is shown in Figure 2.14. In order to quantify the analysis, the curvature volumes were thresholded at the same level and the number of voxels is calculated versus the standard deviation of the noise level (Figure 2.15). The proposed method depends on the voxel intensity change as the noise variation increased the number of false curvature values introduced increased.

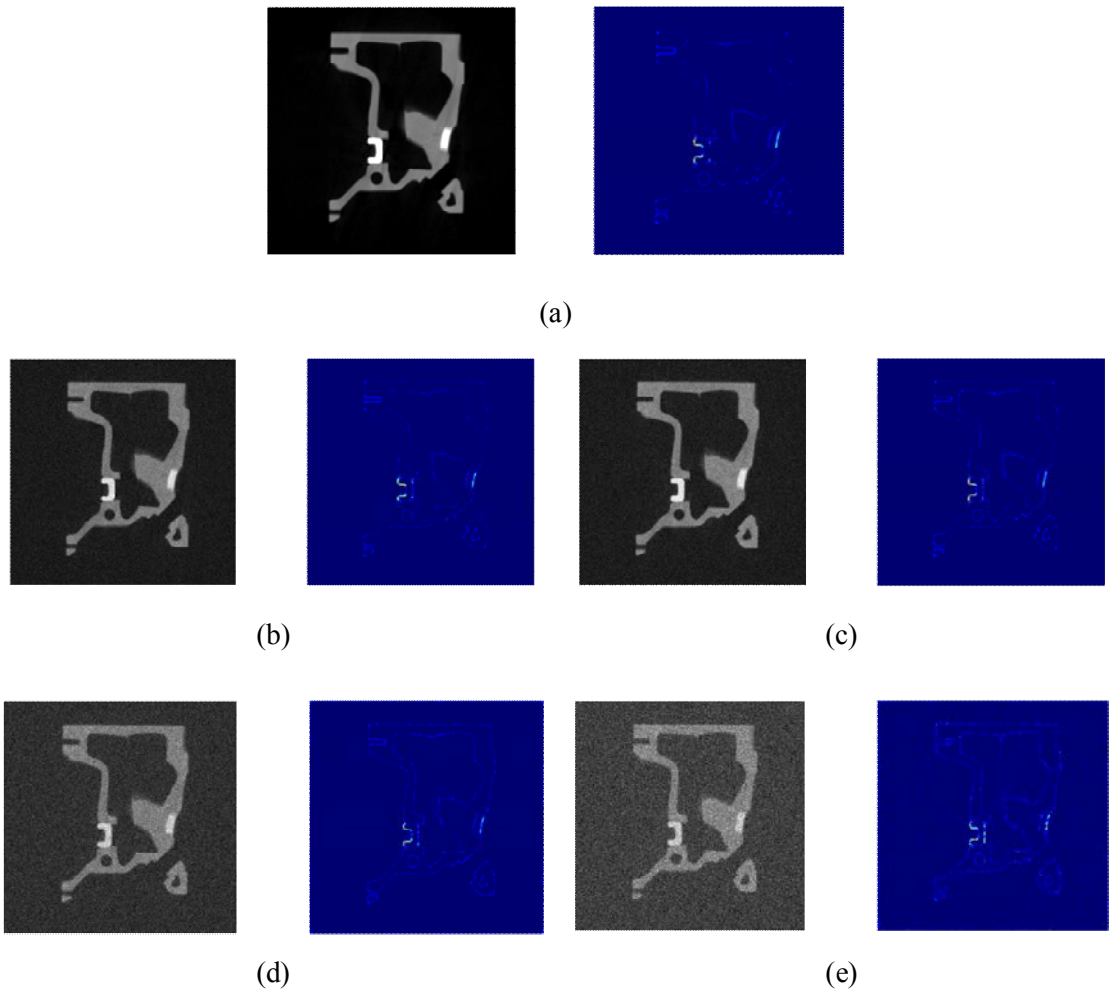

Figure 2.14 The effect of adding random normally distributed noise on the CT scan of an engine block (Figure 2.8), (a) Slice 52 without noise (left) and the corresponding curvature (right), (b) Slice 52 after adding noise on the volume with a mean of 0.5 and standard deviation 0.05 (left) and the corresponding curvature (right), (c) Slice 52 after adding noise on the volume with a mean of 0.5 and standard deviation 0.1 (left) and the corresponding curvature (right), (d) Slice 52 after adding noise on the volume with a mean of 0.5 and standard deviation 0.15 (left) and the corresponding curvature (right) and (e) Slice 52 after adding noise on the volume with a mean of 0.5 (left) and standard deviation 0.2 and the corresponding curvature (right)

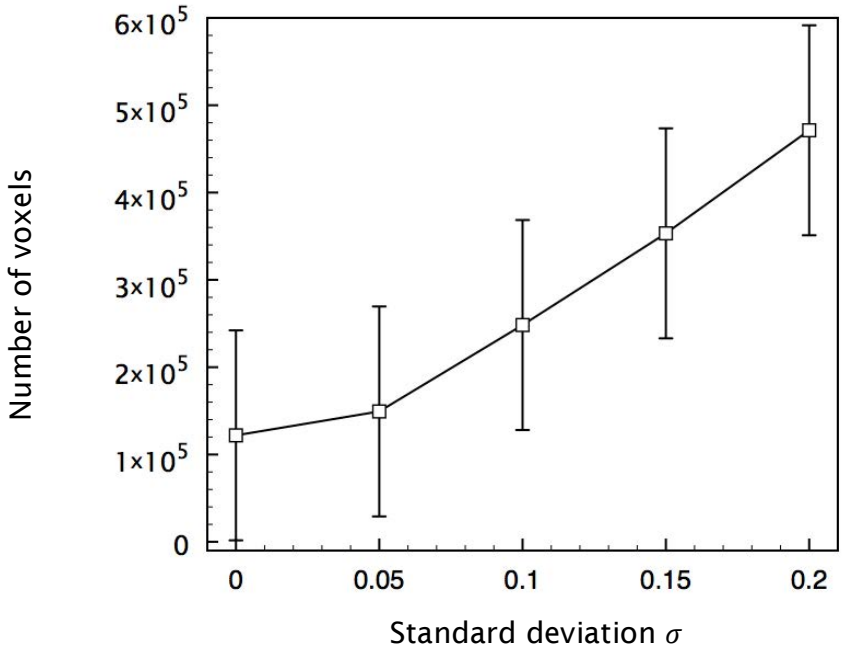

Figure 2.15 The variation in the number of curvature voxels with the change of noise standard deviation at the same threshold value.

2.3 Conclusions

The presented surface detection and surface curvature estimation methods are intuitive extensions to well-established methods in the literature. Providing the basis of extension provides a better understanding of the low level features of the volumetric image. The proposed surface operator is an extended version of Sobel operator (Sobel, 2014) but can expanded to a different window size using weights provided Pascal triangle rather than the intuitive choice as in (Palu et al., 2006; Avinash, 2009). The gradients calculated are used to calculate the curvature estimation from the image intensity as in (Kass et al., 1988) rather than from the geometric location of a mesh vertex (M. Do Carmo, 1976; Stevens, 1981). Several projected curvature values on planar projection are combined to address curvature based on intensity change. The results of the proposed methods provide primary phase for the later feature extraction techniques described in the following chapters to minimize the computational expense, save memory and processing times. The techniques enjoy a clear analytic formulation that is readily extendable to larger operators, including increased smoothing.

Chapter 3: Evidence Gathering Based on Hough Transform

3.1 Introduction

The Hough transform (HT) introduced in (Hough, 1962) is an evidence gathering method for shape detection. In its early days, it was introduced to detect simple shapes such as lines and circles in 2D images and it was later extended to more complex shapes (Duda & Hart, 1972; Kimme, Ballard, & Sklansky, 1975). It is applied to the edge data of the image, to reduce the computational load. The main advantage of using the Hough transform is revealing shapes of interest automatically determining properties of those shapes such as their centre location and the radius of a circle (Illingworth & Kittler, 1987).

In volumetric space, little attention has been given to the Hough transform due to the large amount of computation needed. In fact, a recent paper notes “Very few attempts at HT for 3D data have been presented in the literature” (Camurri et al., 2014). The current attention for volumetric imagery requires an automatic shape detection method using evidence gathering. The main problems facing this extension are the complexity of those volumetric images and that they suffer from noise, clutter and artefacts for which the ability of the Hough transform is well known. We seek to identify geometrical shapes in cluttered volumetric image from their properties using an evidence-gathering method based on the Hough transform, which proved to be robust and reliable.

In this chapter, we are interested in detecting lines, spherical and cylindrical shapes in volumetric space from their Cartesian voxel locations, since these abound in the built environment. The volumetric image may contain structures within the object, which may encompass geometrical shapes of interest rather than mesh surfaces where the normal would be sufficient to collect evidence.

(Rabbani & Heuvel, 2005; Su & Bethel, 2010) proposed a practical solution based on the fact that surface normals would create a great circle on the Gaussian sphere shaped votes accumulator hence the ability to decompose the problem of cylinder detection into multi-stage Hough transform. (Ogundana et al., 2007) also proposed another method for sphere detection, which is also based on the surface normals.

The literature falls short of methods for detecting simple geometrical shapes directly from the voxel information rather than the normals of the faces. In volumetric images, the normals depend significantly on the result of the segmentation and the method used to convert the voxels into mesh. In this work, we present different methods for detecting lines, cylinders and spheres directly from the voxel information.

3.2 Cylinder and sphere detection

The problem of detecting a cylindrical shape in 3D volumetric space is analogous to detecting a circular shape in the same space, since the cylinder consists of a stack of 2D circles. A cylinder in 3D space is defined by the following parameters: height, radius, centre location and two direction angles. A 7D Hough transform is required to detect a cylinder. Processing data in multiple stages would decrease the computational expense and makes the Hough transform more viable (Rabbani & Heuvel, 2005). In this section, we propose finding the cylinder axis, as first stage would provide good evidence about the radius of the cylinder. The second stage to process the axis would determine the length, the two directional angles and the centre location (presented by an end point within the detected axis line) that will be discussed in Section 3.3. Here we present two new vote collection techniques to determine the cylinders' major axis, it is followed by principal component analysis on thresholded votes accumulator to determine the direction accuracy of the detected axis. The resulted direction vector is transformed to spherical coordinates to yield the Azimuth and Elevation angles as in Figure 3.1.

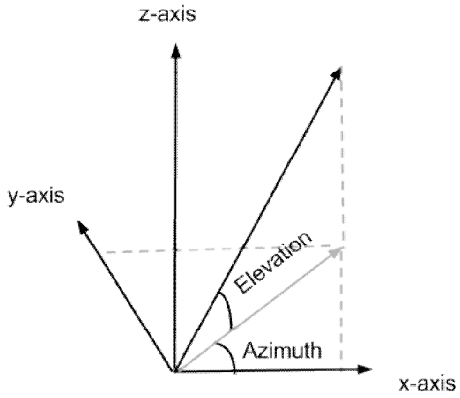

Figure 3.1 The definition of Azimuth (Az) and Elevation (El) angles for a vector to provide better understanding of the directional vector resulted from PCA analysis on detected cylinder axis.

3.2.1 Technique 1: Template Searcher

Convolving a spherical template with the curvature data at every voxel yields the number of points on the surface of the sphere, which are considered as the number of votes at that voxel. In Figure 3.2 a diagram that illustrates the movement of sphere template within a cylinder to collect votes at the central point of the template (presented by a dot) where a set of those votes would present a cylinder axis.

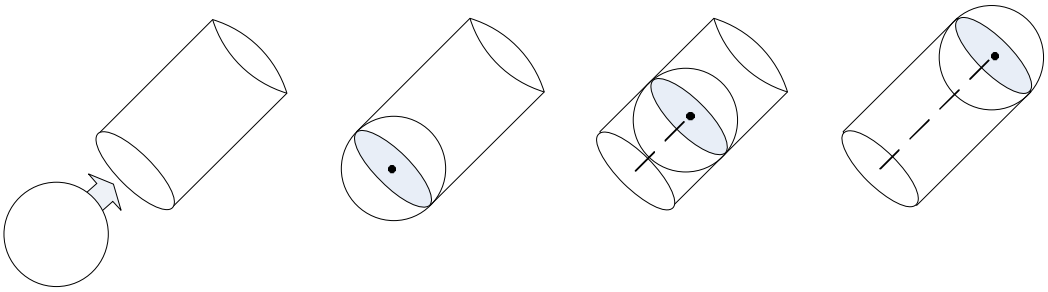

Figure 3.2 A diagram illustrates the proposed template searcher method to collect votes.

The spherical template embedded in a cubic shaped volume with each side determined by Eqn. 3.1.

$$\boldsymbol{Template\ Size\ factor = 2r + 1} \quad 3.1$$

$$\boldsymbol{where\ r\ is\ the\ desired\ radius}$$

The locations in which the template $t(x_i, y_i, z_i)$ is set to true to present a sphere are given by Eqn. 3.2, Eqn. 3.3 and Eqn. 3.4.

$$\boldsymbol{x_i = X_c + r\cos\theta\cos\alpha} \quad 3.2$$

$$\boldsymbol{y_i = Y_c + r\cos\theta\sin\alpha} \quad 3.3$$

$$\boldsymbol{z_i = Z_c + r\sin\theta} \quad 3.4$$

Where (X_c, Y_c, Z_c) represents the central location of the template, θ and α represent the Azimuth and the Elevations angles.

The template is then convolved with zero padded logical volume at every voxel. The number of votes at each voxel is then calculated using Eqn. 3.5.

$$Number\ of\ votes = \sum_{n=1}^{(2r+1)^3} t(n) \cdot volume(n) \quad 3.5$$

The number of votes is then placed into accumulating volume (ACC), which is the same size as the original volume, at the same location as the voxel.

3.2.1.1 Implementation

An upright synthetic cylinder has been created with the following dimensions 40x40x80. The central point of the cylinder was chosen to be in the x-y plane $(21, 21)$ and a radius of 18 voxels. The exact dimensions were noted to compare the result of the proposed method on the synthetic data. Pre-processing the volume with surface detection and curvature detection are shown in Figure 3.3.

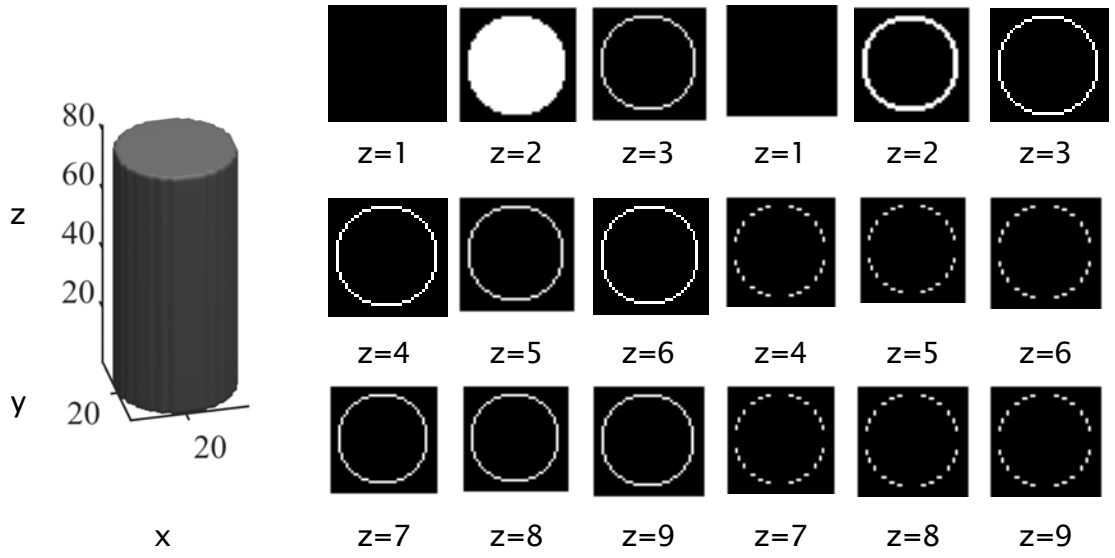

Figure 3.3 Upright synthetic solid cylinder used to assess the methodologies presented in Chapter 3, (a) 3D render of the upright cylinder, (b) Edge detected data using surface operator described in Chapter 2, and (c) Curvature data from the method defined in Chapter 2.

The result of applying the template searcher with radius equal to 18 voxels to the cylinder of Figure 3.3a is shown in Figure 3.4. The Principal components analysis (PCA) has been applied to the thresholded accumulator and it has revealed that the central axis detected is located at the same point defined, (21, 21), and revealed a directional vector of [0, 0, 1] and an angle pair (Az=0˚, El=90˚).

Another synthetic cylinder has been created with radius of 18 voxels. It has been tilted with an angle of 30° in the y-direction using rotation matrix. The volume has been Pre-processed with surface detection and curvature detection as shown in Figure 3.5. Again, the template searcher has been applied with radius 18 voxels. The PCA on the thresholded accumulator Figure 3.6 showed a directional vector of [0, 0.49, 0.86] and an angle pair (Az=90˚, El=60˚), which yields an angle of 30° away from the z-axis towards the y-axis.

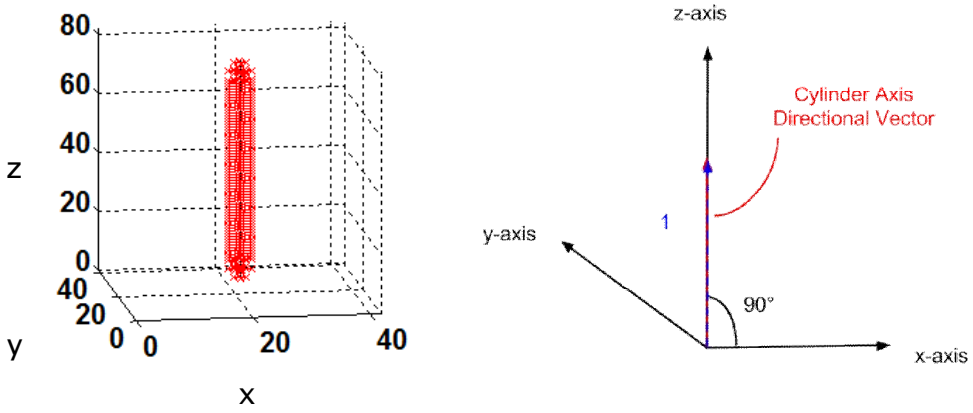

Direction Vector = [0, 0, 1]

Az=0˚, El=90˚

(a) (b)

Figure 3.4 Analysis of the thresholded votes accumulator resulted from Template Searcher applied to the upright cylinder in Figure 3.3 (a) Principal components analysis applied to the thresholded accumulator with the resulted directional vector [0, 0, 1], and (b) The angle presenting the directional vector (cylinder axis) with an Azimuth angle of 0˚ and an Elevation angle of 90˚

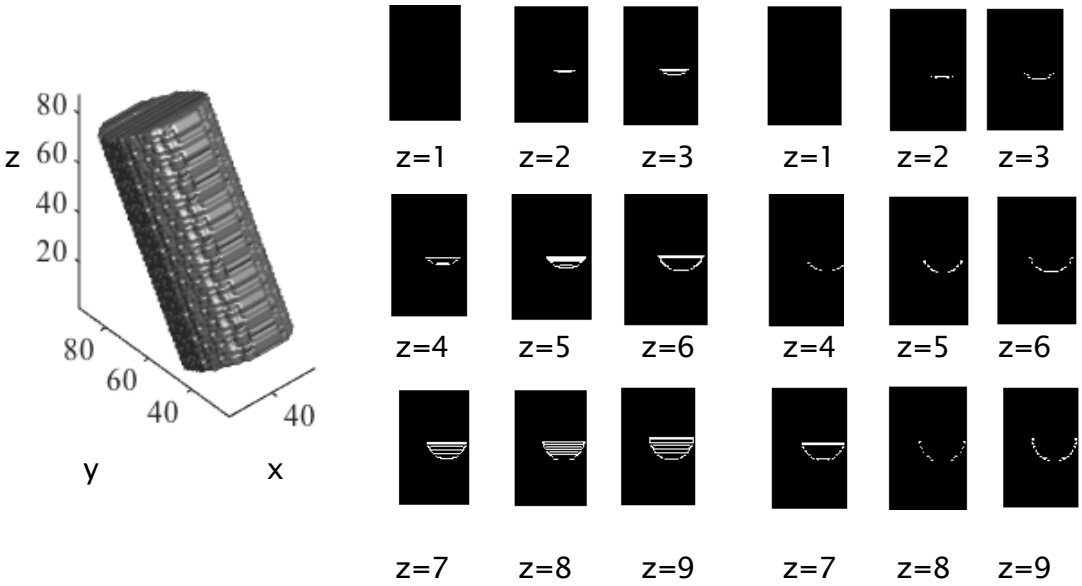

(a) (b) (c)

Figure 3.5 Tilted synthetic cylinder by 30° from the z-axis towards the y-axis, (a) 3D render of the tilted cylinder, (b) Edge detected data using surface operator described in Chapter 2, and (c) Curvature data from the method defined in Chapter 2.

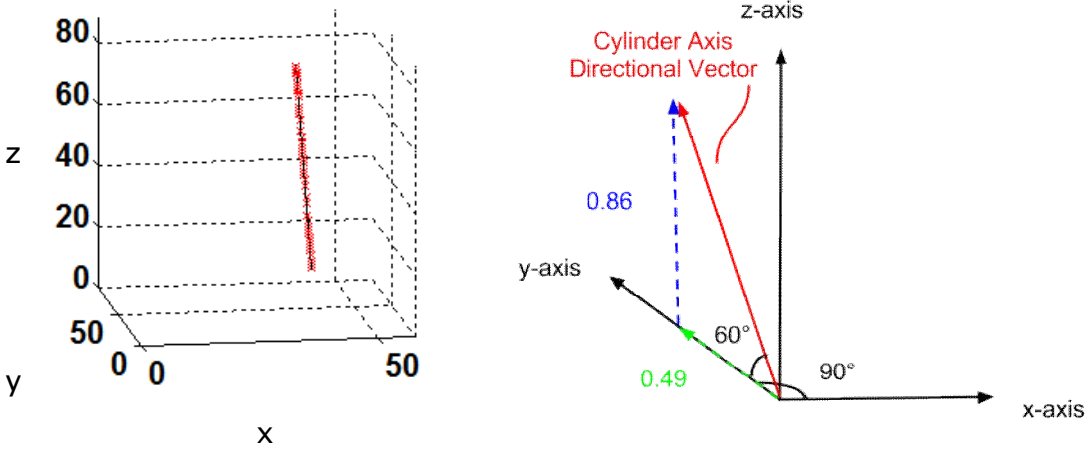

Direction Vector = [0, 0.49, 0.86]

Az=90˚, El=60˚

(a) (b)

Figure 3.6 Analysis of the thresholded votes accumulator resulted from Template Searcher applied to the titled cylinder in Figure 3.5 (a) Principal components analysis applied to the thresholded accumulator with the resulted directional vector [0, 0.49, 0.86], and (b) The angle presenting the directional vector (cylinder axis) with an Azimuth angle of 90˚ and an Elevation angle of 60˚ (which translates to 30˚ away from the z-axis towards the y-direction).

3.2.1.2 Experimental results

Applying the template searcher has shown good results in detecting the synthesized cylinders' axis. The difference between applying the method to synthetic data and real CT data is the fact that the latter has more noise. The noise here is defined by the existence of other shapes in the scene of interest. Decreasing the amount of noise is the main reason behind the surface curvature detection usage.

A segment of a two-cylinder engine block contains two cylindrical shapes with different radius values have been evaluated. By manually measuring the radius of each cylinder radius, it has been found that the large cylinder has a radius of 11 voxels and the small cylinder has a radius of 7 voxels. Slices through the original volume, edge detected volume and curvature estimated volume are also shown in Figure 3.7. From the curvature slices, we notice a fair amount of unrelated data has been removed, in comparison to the edge data.

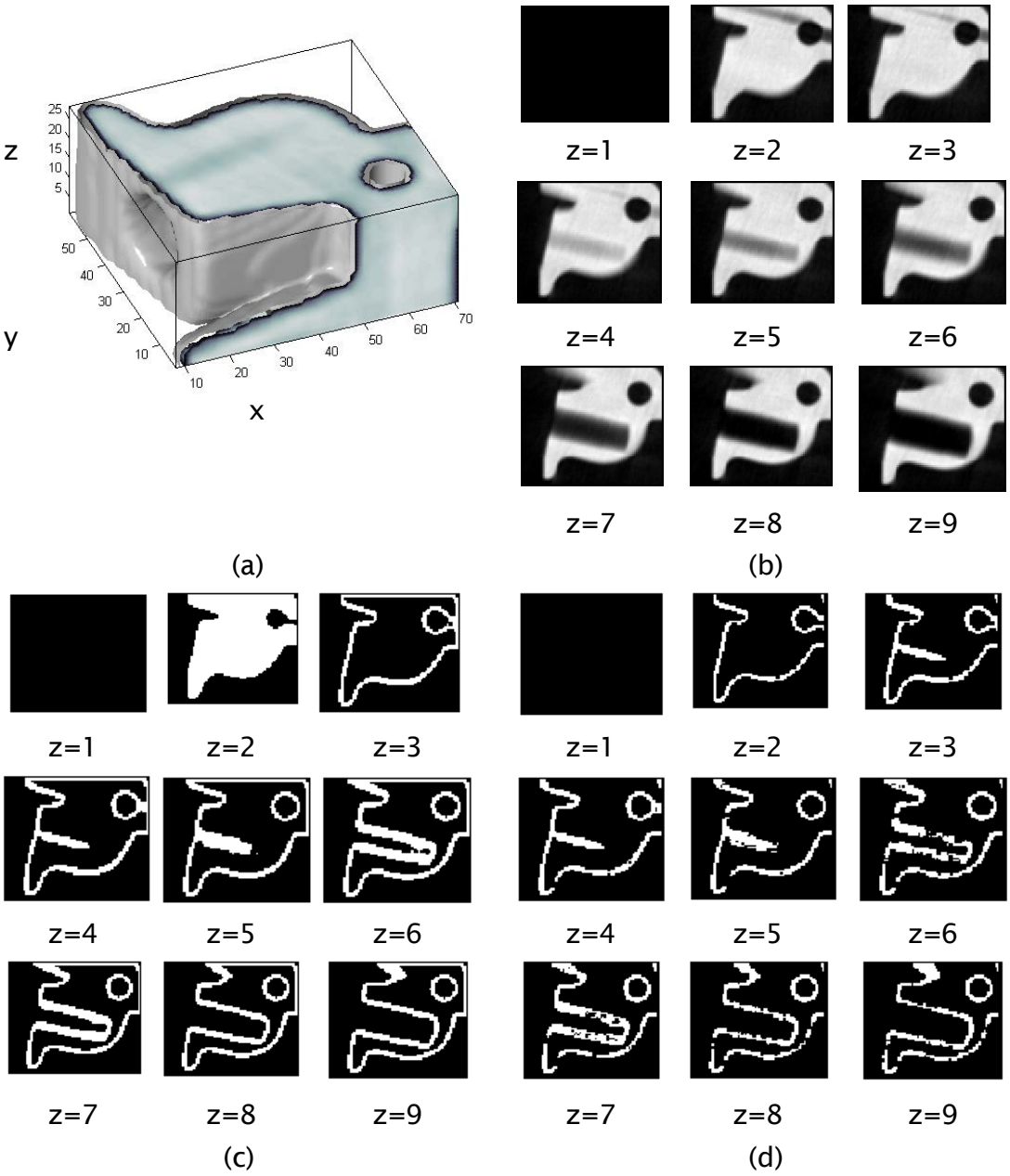

Figure 3.7 A segment of a two-cylinder engine block with two cylindrical shapes with two different radius values (a) Render of the engine segment, (b) Nine slices through the engine data, (c) Nine slices through surface data and (d) Nine slices through curvature data.

Template searcher with two different radius values r = 11 voxels and r = 7 voxels has been applied to the set of data in Figure 3.7, see Figure 3.8. The radius value has been set to decrease the computational expense and to easily identify the detection of the cylinder axis. The resulted votes have been fitted with PCA to extract the directional vectors. At radius r=11 the resulted directional vector [0.97, 0.21, 0] and an angle pair (Az=12.48˚, El=0˚) and at

radius r=7 the resulted directional vector [0, 0, 1] and an angle pair (Az=0˚, El=90˚).

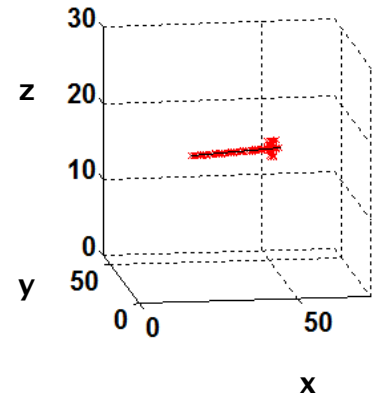

Direction Vector = [0.97, 0.21, 0]

Template searcher with radius =11

(a)

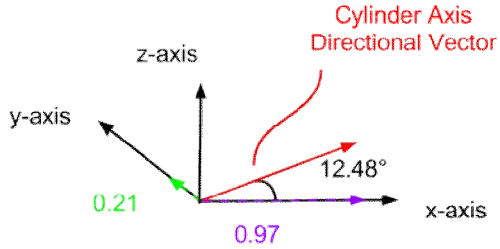

Az=12.48˚, El=0˚

(b)

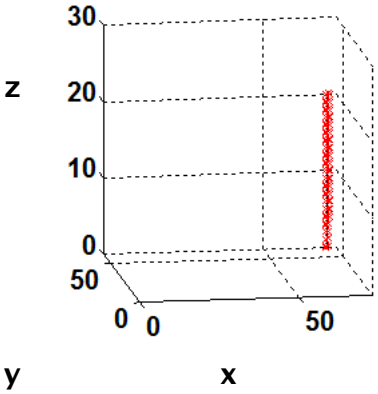

Direction Vector =[0, 0, 1]

Template searcher with radius =7

(c)

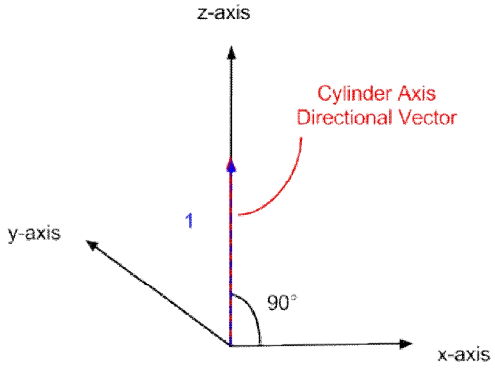

Az=0˚, El=90˚

(d)

Figure 3.8 Analysis of the thresholded votes accumulator resulted from Template Searcher applied to the engine block segment in Figure 3.7 (a) Principal components analysis applied to the thresholded accumulator where the radius was set to 11 and the resulted directional vector [0.97, 0.21 ,0], (b) The angle presenting the directional vector (cylinder axis) with an Azimuth angle of 12.48˚ and an Elevation angle of 0˚, (c) Principal components analysis applied to the thresholded accumulator where the radius was set to 7 and the resulted directional vector [0, 0, 1], and (d) The angle presenting the directional vector (cylinder axis) with an Azimuth angle of 0˚ and an Elevation angle of 90˚.

Applying the developed methods of curvature and axis detection to a single coin from the set of data presented in Figure 1.1 is shown in Figure 3.9 where a single coin is under investigation using template searcher. Since the coins are shaped more like disks or ellipsoids than cylinders, it is expected to have few votes for the coin axis, which means less accurate direction estimation. PCA fitted data in Figure 3.9 gave a directional vector of [-0.2136 , 0.5209, 0.8264] and an angle pair (Az=111.99˚, El=55.63˚).

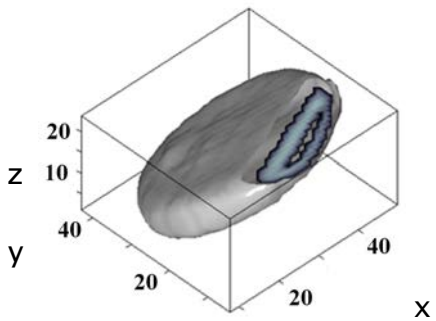

(a)

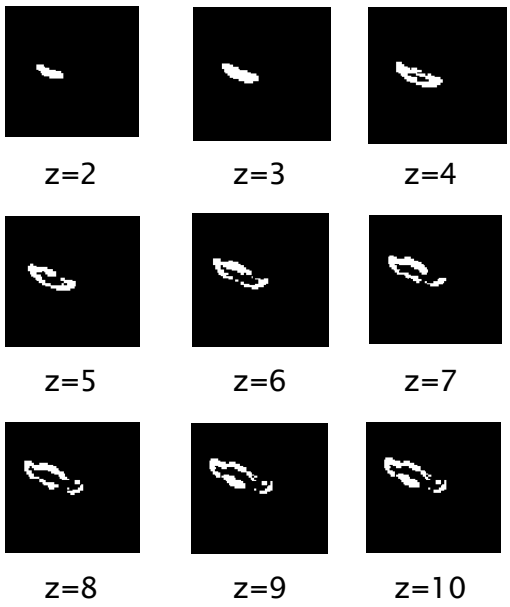

(b)

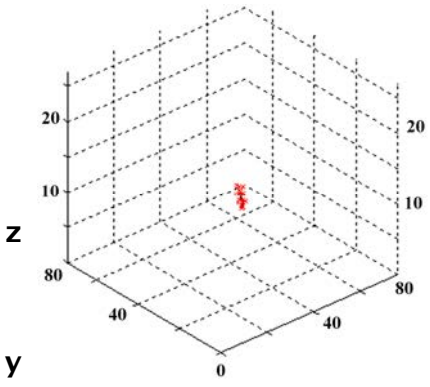

Direction Vector: [-0.21, 0.52, 0.82]

(c)

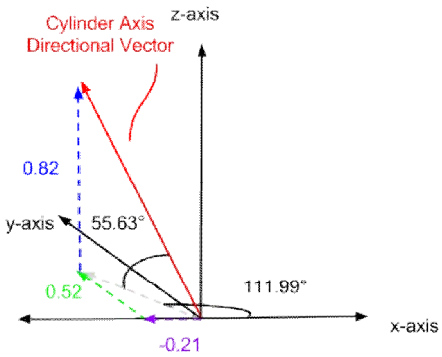

Az=111.99˚, El=55.63˚

(d)

Figure 3.9 A single coin under investigation using template searcher (a) 3D rendered single coin, (b) Nine slices through curvature data of the coin in (a), (c) PCA fitted votes after applying template searcher with radius = 18 and the resulted directional vector [0, 0, 1], and (d) The angle presenting the directional vector (cylinder axis) with an Azimuth angle of 111.99˚ and an Elevation angle of 55.63˚.

3.2.2 Technique 2: Point-sphere searcher

An alternative technique is based on the Hough transform for circles detection (Greig & Klein, 1986) and which considers that every point in curve data corresponds to a sphere in the Hough space. Figure 3.10 illustrates the vote collection using the proposed extension of Hough transform for circles presented in (Illingworth & Kittler, 1987), each voxel in the volume space that lies on the cylinder surface creates a sphere in the accumulator Hough space.

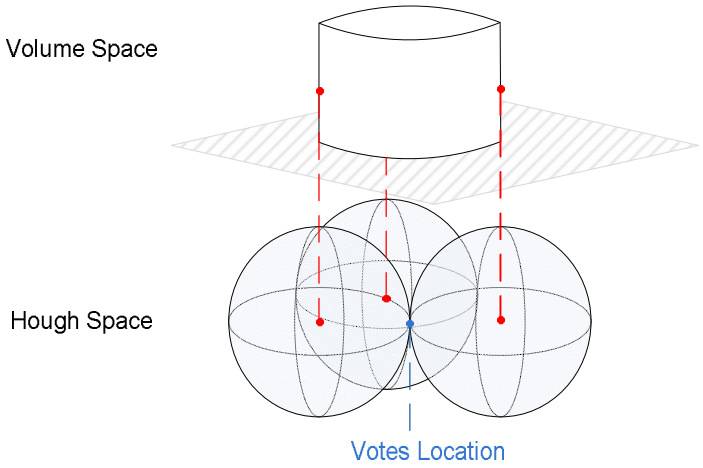

Figure 3.10 A diagram illustrates the proposed point-sphere searcher method to collect votes in Hough space.

The voting procedure is to add a sphere in the accumulator volume ($\boldsymbol{ACC}$) centralized at the each voxel location, using the spherical template $\boldsymbol{t}(x_i, y_i, z_i)$ from the previous section Eqn. 3.6.

$$\boldsymbol{ACC}(\boldsymbol{x_i}, \boldsymbol{y_i}, \boldsymbol{z_i}) = \boldsymbol{ACC}(\boldsymbol{x_i}, \boldsymbol{y_i}, \boldsymbol{z_i}) + \boldsymbol{t}(\boldsymbol{x_i}, \boldsymbol{y_i}, \boldsymbol{z_i}) | \boldsymbol{x_i}, \boldsymbol{y_i}, \boldsymbol{z_i} \in \boldsymbol{sphere} \qquad 3.6$$

This method carries the same conic property of the original method, which provides a convenient way for votes' collection.

3.2.2.1 Implementation

A point-sphere searcher with radius 18 voxels has been applied to the upright cylinder in Figure 3.3 and the tilted cylinder in Figure 3.5, as shown in Figure 3.11. For the upright cylinder the PCA on the thresholded votes accumulator revealed that the central axis detected is located at the same point defined, (21, 21), and revealed directional vector of [0, 0, 1] and an angle pair (Az=0˚,

El=90˚) on the other hand the tilted cylinder gave a direction vector of [0, 0.49, 0.86] and an angle pair (Az=90˚, El=60˚) which yields an angle of 30°.

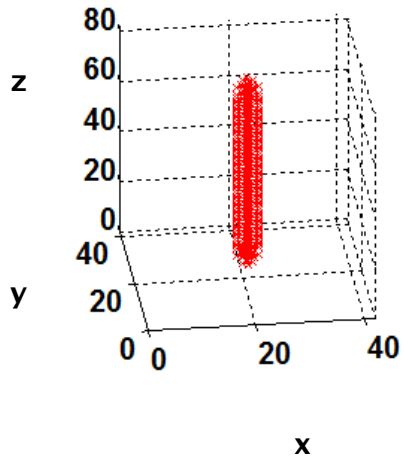

Direction Vector = [0, 0, 1]

(a)

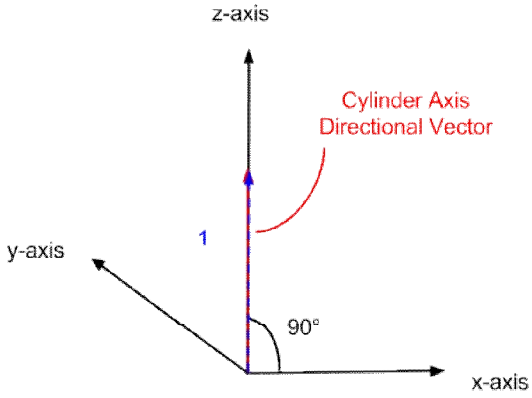

Az=0˚, El=90˚

(b)

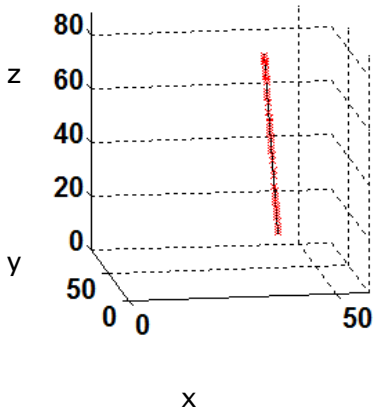

Direction Vector = [0, 0.49, 0.86]

(c)

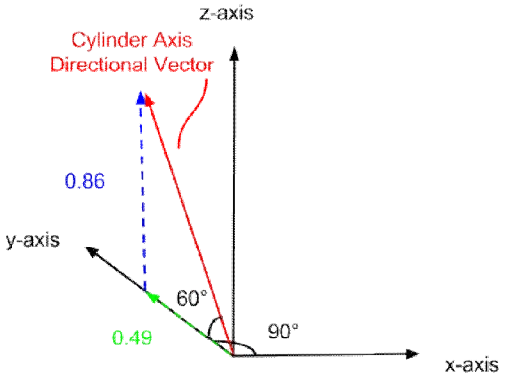

Az=90˚, El=60˚

(d)

Figure 3.11 Analysis of the thresholded votes accumulator resulting from Point-Sphere Searcher (a-b) Applied to the upright cylinder in Figure 3.3, where principal components analysis applied to thresholded accumulator resulted in directional vector [0, 0, 1] and angles presenting the directional vector (cylinder axis) with an Azimuth angle of 0˚ and an Elevation angle of 90˚, and, (a-b) Applied to the upright cylinder in Figure 3.5,where principal components analysis applied to thresholded accumulator resulted in directional vector [0, 0.4994, 0.8664] and angles presenting the directional vector (cylinder axis) with an Azimuth angle of 90˚ and an Elevation angle of 60˚ (which translates to 30˚ away from the z-axis towards the y-direction).

3.2.2.2 Experimental results

Applying point-sphere searcher to the two cylinder engine segment of Figure 3.7 with radius = 11 voxels and radius= 7 voxels to save computation time is shown in Figure 3.12, which presents two direction vectors related to the related values respectively [0.97, 0.21, 0] and an angle pair (Az=12.48˚, El=0˚) and [0, -0.01, 0.99] and an angle pair (Az=90˚, El=89.4˚).

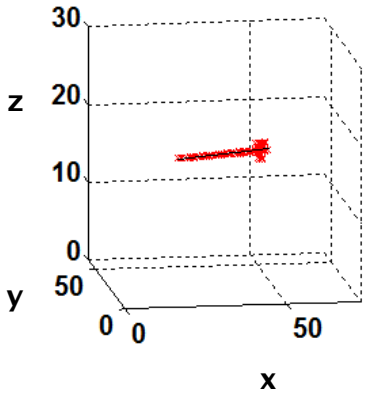

Direction Vector=[0.97, 0.21, 0]

(a)

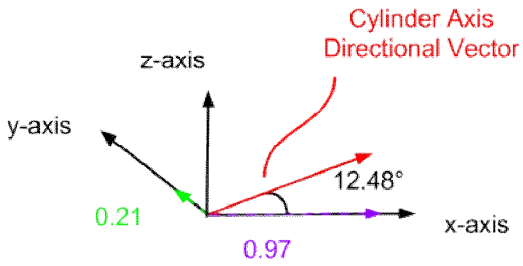

Az=12.48˚, El=0˚

(b)

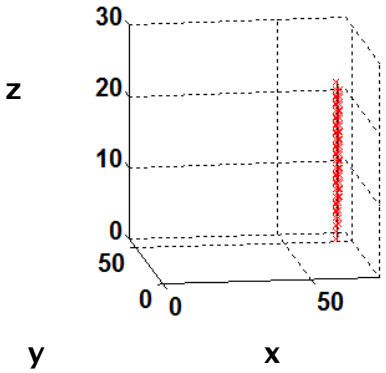

Direction Vector=[0, -0.01, 0.99]

(c)

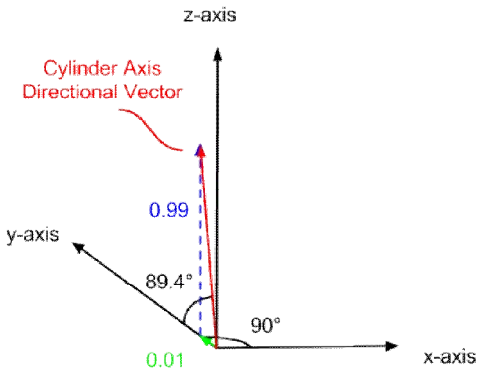

Az=90˚, El=89.4˚

(d)

Figure 3.12 Analysis of the thresholded votes accumulator resulting from Point-Sphere Searcher applied to the engine block segment in Figure 3.7 (a) Principal components analysis applied to the thresholded accumulator where the radius was set to 11 and the resulted directional vector [0.97, 0.21, 0], (b) The angle presenting the directional vector (cylinder axis) with an Azimuth angle of 12.48˚ and an Elevation angle of 0˚, (c) Principal components analysis applied to the thresholded accumulator where the radius was set to 7 and the resulted directional vector [0,-0.01,0.99], and (d) The angle presenting the directional vector (cylinder axis) with an Azimuth angle of 90˚ and an Elevation angle of 89.4˚.

In the last test, point-sphere searcher has been applied to coin data of Figure 3.9 and the resulted vector is [-0.29, 0.5, 0.81] and an angle pair (Az=120.11˚, El=54.48˚) see Figure 3.13.

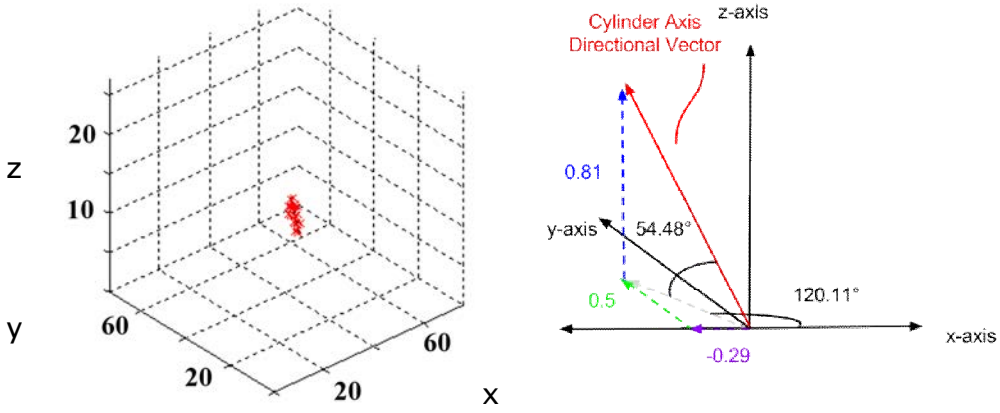

Direction Vector=[-0.29, 0.50, 0.81]

(a) (b)

Figure 3.13 Analysis of using Point-Sphere Searcher on coin of Figure 3.9 (a) PCA fitted votes after applying template searcher with radius = 18 and the resulted directional vector [-0.29,0.50,0.81], and (b) The angles presenting the directional vector (cylinder axis) with an Azimuth angle of 120.11˚ and an Elevation angle of 54.48˚.

3.2.3 Sphere detection

The spherical Hough transform would be of great aid for biomedical applications especially for the current advances in the imaging system and increased interest in studying the newly developed databases to examine changes from one generation to the next. Sphere detection using Hough is rarely tackled in literature, (Ogundana et al., 2007) used surface normal to accumulate votes, which proved to be useful in point cloud environment. The conic property of the Hough transform is not inherited using this method. In this section, we use the same proposed methods as in Sections 3.2.1 and 3.2.2 on sphere detection except this time the threshold for the accumulator is based on the largest cells of votes. In the template method, the sphere template would overlap the sphere in the volume to create a cell containing the number of overlapping voxels hence to create an accumulator cell with the largest number of votes. On the other hand, the point-sphere method would generate a cell in the accumulator with a large number of votes based on the intersection of multiple spheres generated by every voxel in the volume.

To test the validity of the proposed method, applications on a CT scan of Christmas tree shown in Figure 3.14. The accumulator is still 4D and for simplicity, the use a constant value for the sphere radius is based on a manually measured radius of ten voxels. The ground truth was done by visual inspection on the tree, which shows that eight ornaments exist. The thresholded accumulators based on the proposed methods in Figure 3.15 shows that the spherical Christmas tree ornaments hanged on the tree branches were detected. The threshold value was chosen to be 80 percent of maximum number of votes in the accumulator. The results show that the template searcher performed better for this task by detecting all the ornaments, on the other hand, the point sphere were able to detect five spheres.

Those basis of the proposed methods were used later in (Abuzaina et al., 2013) to provide a novel velocity Hough transform to reconstruct a sphere in a missing video frame. Simply by projecting the velocity at which the sphere is moving from one frame to the next, fully occluded spheres could be reconstructed with a tolerable margin of error.

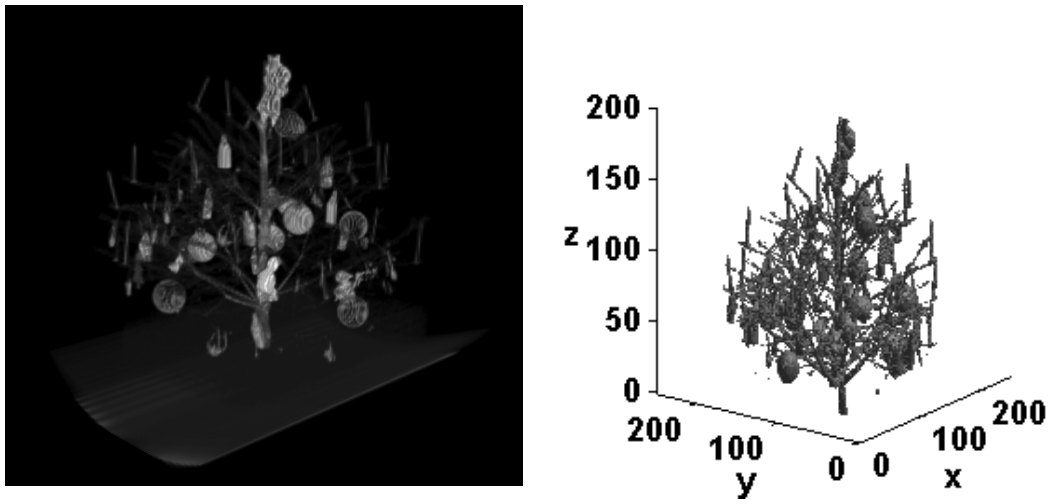

Figure 3.14 Render of CT scanned Christmas tree, showing several spherical ornaments that would be suitable to test Hough for detecting spheres.

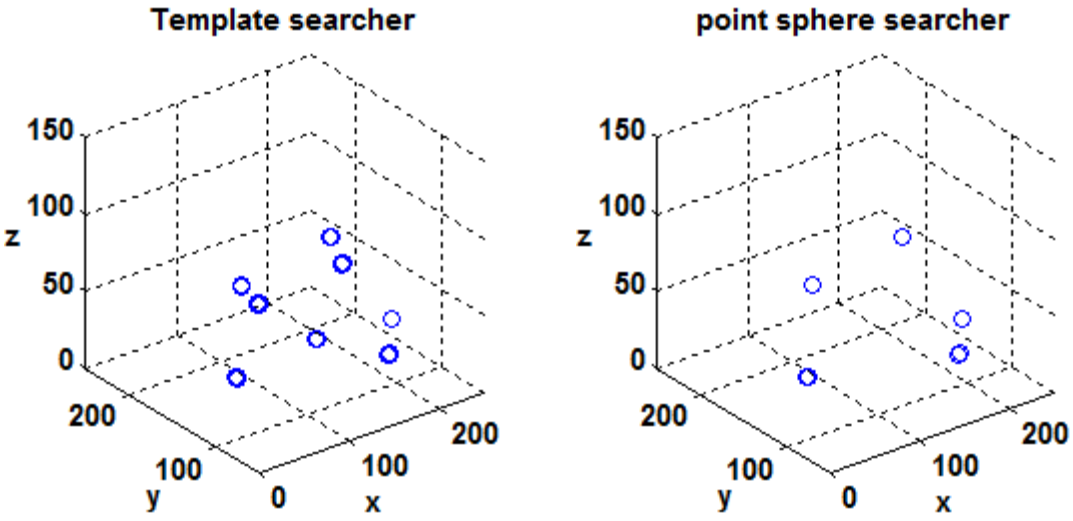

(a) (b)

Figure 3.15 Thresholded accumulators based on the 80% of the maximum number of votes using (a) Template searcher in Section 3.2.1 and (b) Point sphere searcher in Section 3.2.2 for the Christmas tree of Figure 3.14.

3.2.4 Discussion

Both approaches in sections 3.2.1 and 3.2.2 showed similar excellent results when applied to synthetic data. Table 3.1 Comparison between the direction vectors of synthetic data. The direction vectors calculated were identical the only problem was choosing a proper threshold value for the votes, which is in this case 0.7 of the maximum number of votes.

	Template searcher	Point-sphere searcher
Upright Cylinder (Az, El)	(0˚, 90˚)	(0˚, 90˚)
Tilted Cylinder (Az, El)	(90˚, 60˚)	(90˚, 60˚)

Table 3.1 Comparison between the direction vectors of synthetic data

On the other hand, the direction vectors of the engine segment showed a slight difference that is negligible (Table 3.2). Both searchers had shown approximately identical results.

	Template searcher	Point-sphere searcher
Searcher with radius 11 (Az, El)	(12.48˚, 0˚)	(12.48˚, 0˚)
Searcher with radius 7 (Az, El)	(0˚, 90˚)	(90˚, 89.4˚)

Table 3.2 Comparison between the direction vectors of the engine segment

As mentioned earlier the searchers should be able to face the challenge of the coin data presented in Chapter 1. The resulted direction vectors had shown a slight difference between the two searchers Table 3.3.

	Template searcher	Point-sphere searcher
Searcher with radius 18 (Az, El)	(111.99˚, 55.63˚)	(120.11˚, 54.48˚)

Table 3.3 Comparison between the direction vectors of the coin data

The coin exact direction is unknown as the coin data spread randomly throughout the CT volume. To determine which vector is close to the correct direction, a plane fitting through the curvature data has been used (Figure 3.16).

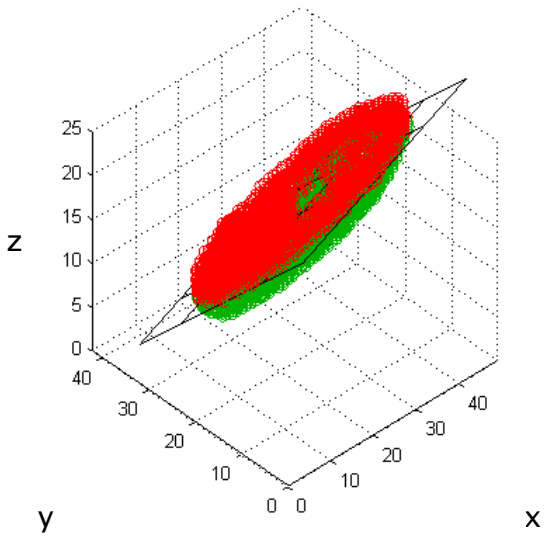

Direction Vector: [-0.2991, 0.4439, 0.8447]
Az=123.38, El=57.89

Figure 3.16 Fitted plane through the curvature data in Figure 3.9

The new direction vector [-0.2991, 0.4439, 0.8447] resulted from the direction normal to the fitted plane and an angle pair (Az=123.38˚, El=57.89˚). The error percentages of the calculated axis angles (Az, EL) using Template searcher and Point sphere searcher with ground truth based on angles found using fitting presented in Figure 3.16 are shown in Table 3.4. The point-sphere searcher showed smaller error magnitude hence better direction estimation.

	Template searcher	Point-sphere searcher
Azimuth angle error	9.3%	3.9%
Elevation angle error	2.6%	5.8%

Table 3.4 Axis calculation error using the proposed method of evidence gathering template searcher and point-sphere searcher

A speed comparison between the two searchers is shown in Figure 3.17. In terms of speed the template searcher showed superior speed compared to the point-sphere searcher. The tilted cylinder showed an increase in the processing time due to the rotation effect, which cause the surface detection to introduce extra voxels, which caused the point-sphere method to process more voxels and do extra calculations in the accumulator space.

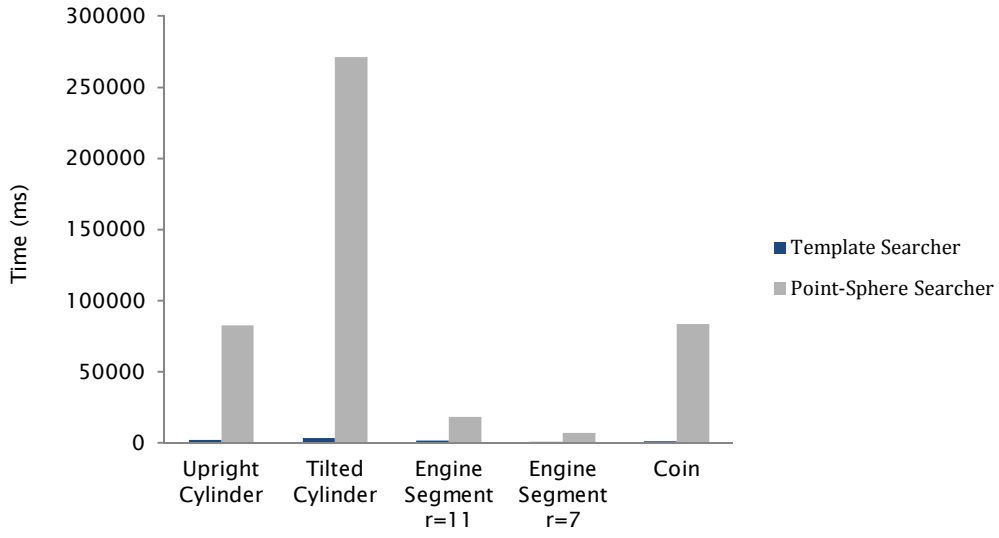

Figure 3.17 Speed comparison between template and point-sphere searchers; speed tests have been performed on a Macbook Pro machine with core due two processor 2.5GHz, 8GB ram and 256 SSD drive.

Template searcher performed better at detecting spherical shapes task by detecting all the ornaments in Figure 3.14, in contrast the point-sphere operator was able to detect only five spheres for the same value of threshold. Changing the threshold value introduced other hypothetical spheres that cannot be seen visually but there is evidence based on the selected threshold that suggests the existence of those spheres.

Applying the Hough transform to a multi-object complex scene as in Figure 1.1 produce an accumulator array that is much affected by noise arising from other shapes in the scene. Using a condition-based threshold on the number of points in the detected shape makes the method more prone to noise when used to analyse 3D data. Should the objects in 3D space be separated before application of the Hough transform, this would minimize the noise introduced by the surrounding objects and would help to gather more evidence about the existence of a circle in the 3D space.

It is also worth noting that a single cylinder axis will currently be detected by the searcher if the range of parameter values is close to the target shape. The coin shape is much deformed and the low resolution may have played a role in adding difficulty to the process.

3.3 3D line detection

The Hough transform is known to excel in detection of geometric shapes from their parameters. In two-dimensional space line detection using Hough transform has received great popularity and a wide range of literature. On the other hand the approach has not had as much attention in three-dimensional space (3D) due either to the high dimensionality required by the method or to the recent increased interest in 3D imaging systems. Line detection can provide the second stage for the methods proposed in Sections 3.2.1 and 3.2.2 for cylinder detection. Several attempts to solve line detection based on Hough transform in 3D images (Bhattacharya et al., 2000; Zhou, Qiu, Ding, & Zhang, 2008) each have their own approach. The only drawback common to these between those methods is neglecting the line length during the accumulation process, which is a fundamental parameter in line Hough detection. In the case of point cloud images many have been interested in plane detection using

surface normals and good results have been obtained (Overby, Bodum, Kjems, & Iisoe, 2004) . In volumetric images plane detection by directly expanding the original method introduced by (Duda & Hart, 1972) into 3D has not merited prior study. The expansion starts with the plane equation as follows:

$$\boldsymbol{Plane\ Equation} \rightarrow \boldsymbol{a} * \boldsymbol{x} + \boldsymbol{b} * \boldsymbol{y} + \boldsymbol{c} * \boldsymbol{z} = \boldsymbol{d} \quad 3.7$$

Where

$$\boldsymbol{d} = \boldsymbol{a} * \boldsymbol{x_o} + \boldsymbol{b} * \boldsymbol{y_o} + \boldsymbol{c} * \boldsymbol{z_o} \quad 3.8$$

$$\textbf{Normal Vector} = (\boldsymbol{a}, \boldsymbol{b}, \boldsymbol{c}) \quad 3.9$$

$$\boldsymbol{Point\ on\ the\ plane} = \boldsymbol{p_o} = (\boldsymbol{x_o}, \boldsymbol{y_o}, \boldsymbol{z_o}) \quad 3.10$$

$$\boldsymbol{a} = \boldsymbol{cos\theta} * \boldsymbol{cos\varphi} \quad 3.11$$

$$\boldsymbol{b} = \boldsymbol{sin\theta} * \boldsymbol{cos\varphi} \quad 3.12$$

$$\boldsymbol{c} = \boldsymbol{sin\varphi} \quad 3.13$$

And by following the trigonometric transform (Illingworth & Kittler, 1987), a plane in 3D can be described using the parameters defined in Figure 3.18.The parametric equation can then be described as:

$$\boldsymbol{\rho} = \boldsymbol{x} * \boldsymbol{cos\theta} * \boldsymbol{cos\varphi} + \boldsymbol{y} * \boldsymbol{sin\theta} * \boldsymbol{cos\varphi} + \boldsymbol{z} * \boldsymbol{sin\varphi} \quad 3.14$$

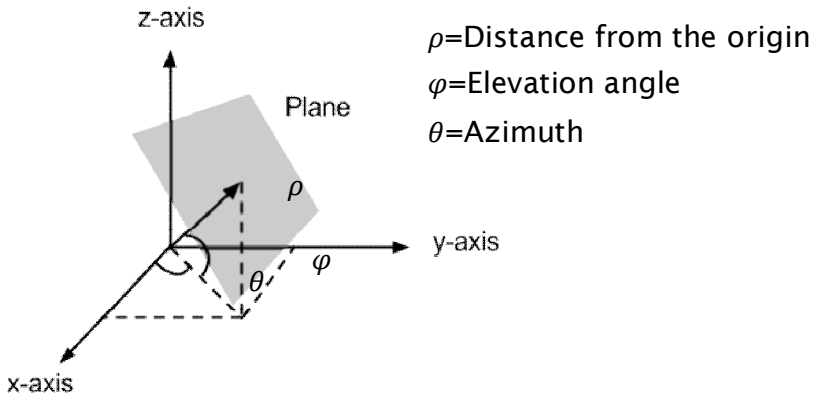

Figure 3.18 Parameters initialization for plane in 3D space.

The duality inherent in the Hough transform for planes in images is that planes map to points (and vice versa). In 3D space, voxels in an *xyz* parameterisation map to planes, whereas voxels in $\rho\theta\varphi$ map to multiple sinusoids. The direct expansion of the 2D parametric equation would result in a volumetric accumulator of sinusoidal waves expanding through the accumulator planes, which makes the visualization and the interpretation difficult. As this is an accumulator for plane detection, it would fail to detect lines (Sarti & Tubaro, 2002). To detect a line by this method, intersection between different planes has to be evaluated.

The line detection in 3D space has been addressed by investigating range images (Bhattacharya et al., 2000). The Hough space is based on the cosine of the angles of a fitted line resulting from shape edges without regard for line size or location. Also the detected edges of the range images were based on the definition of the edge (perimeter) of the object, which is in 3D expanded to surface using the second derivative. In following the trail of the original Hough transform for line detection, the proposed method is designed to tolerate missing gaps on the object surface and noise.

3.3.1 Methodology

Each voxel in a volumetric image of an object surface was investigated to yield its relationship with the surrounding voxels to create an easy to interpret accumulator. If the voxel under study $p_{i,j,k}$ is set to foreground then it is subtracted from every voxel $p_{x,y,z} \in \mathbf{V}$. As a result for the subtraction, the origin is shifted at the current point $p_{i,j,k}$ and this can be presented as:

$$\boldsymbol{New\ Origin} = \boldsymbol{p_{x,y,z}} - \boldsymbol{p_{i,j,k}} \qquad \forall\, \boldsymbol{p_{x,y,z}} \in \mathbf{V} \qquad 3.15$$

A coordinate transform was applied to convert from Cartesian to Spherical coordinates, which in turn simulates the effect of an analog sphere with varying radius centred at $p_{i,j,k}$. The radius here matters little, as the prime interest is the direction of the normal on the surface of the sphere. A planar accumulator $S_i(\theta, \varphi)$ was formed based on the azimuth (θ) and the elevation (φ) angles of the transform, each pair of (θ, φ) contribute in a vote. The number of votes in each plane is equivalent to the number of voxels in a line

passing through a pair of angles. The process of origin shifting was then repeated for each voxel $p_{x,y,z}$ in the volume to create a stack of planes $\mathbf{S}$.

$$\boldsymbol{S}_i(\theta,\varphi) \quad where \quad i = 1{:}\,\#voxels\ in\ \mathbf{V}, \theta = 0{:}\,360\,, \varphi = -90{:}\,90 \tag{3.16}$$

$$\mathbf{S} = [S_{\mathbf{1}}, S_{\mathbf{2}}, S_{\mathbf{3}}, \dots\dots\dots, S_{\#\text{voxels in } \mathbf{V}}\,] \tag{3.17}$$

A vector $\boldsymbol{L}$ of the detected line magnitudes was created and a histogram based on the unique line magnitudes $\boldsymbol{L}_i$ and number of voxels corresponding to it in $\mathbf{S}$ was used to initialize the size of the accumulator $\boldsymbol{A}$ by identifying the maximum line length detected**.** Each plane in the accumulator $\mathbf{A}$ defines a line magnitude and contains the number of lines for each pair of (θ,φ) angles.

$$\boldsymbol{A} = [\,L_1(\theta,\varphi), L_2(\theta,\varphi), L_3(\theta,\varphi), \dots\dots\dots, L_{\text{maximum line length}}(\theta,\varphi)] \tag{3.18}$$

Once the desired peak has been identified and based on the line magnitude and the pair of angles, the address of each voxel contributed into the voting process was called and then fitted into a line using the equation for lines in 3D space.

$$\begin{bmatrix} X \\ Y \\ Z \end{bmatrix} = \begin{bmatrix} i \\ j \\ k \end{bmatrix} + t \begin{bmatrix} a \\ b \\ c \end{bmatrix} \tag{3.19}$$

Where

The Normal Vector = (a, b, c)

i, j, k the coordinates of a point contributed in the votes passing through the detected line.

$a = cos\theta * cos\varphi, b = sin\theta * cos\varphi\ and\ c = sin\varphi$

To illustrate the process visually, Figure 3.19 shows an image of a line consisting of three voxels. The normal vector angles to the spheres centred at the voxel location are accumulated in planar accumulator $\mathbf{S}$ for each voxel. Based on the magnitudes detected, which in this case one and two, a new volumetric accumulator $\boldsymbol{A}$ was formed, based on the line magnitude was formed.

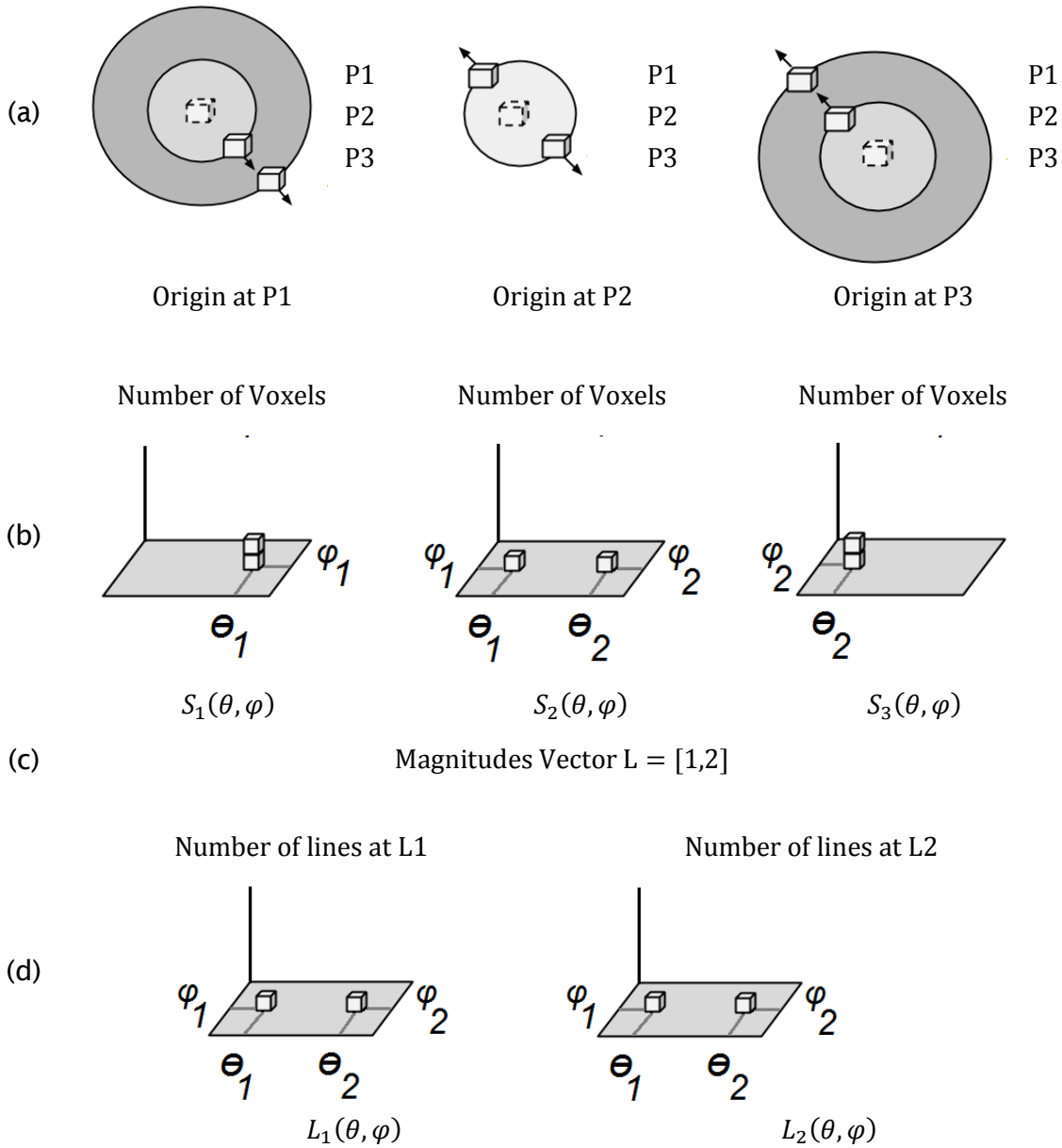

Figure 3.19 The process of line detection using the proposed method on a line consisting of three voxels, (a) Origin shifting and coordinate transform at each voxel P1,P2 and P3, (b) Plane accumulators $S_1(\theta,\varphi), S_2(\theta,\varphi)$ and $S_3(\theta,\varphi)$ for voxels P1,P2 and P3 respectively, showing the number of voxels at each pair of (θ,φ), (c) The magnitude vector L which contain all the magnitudes within the plane accumulators **S**, (d) The planes $L_1(\theta,\varphi)$ and $L_2(\theta,\varphi)$ of the accumulator **A** showing the number of lines at each pair of (θ,φ).

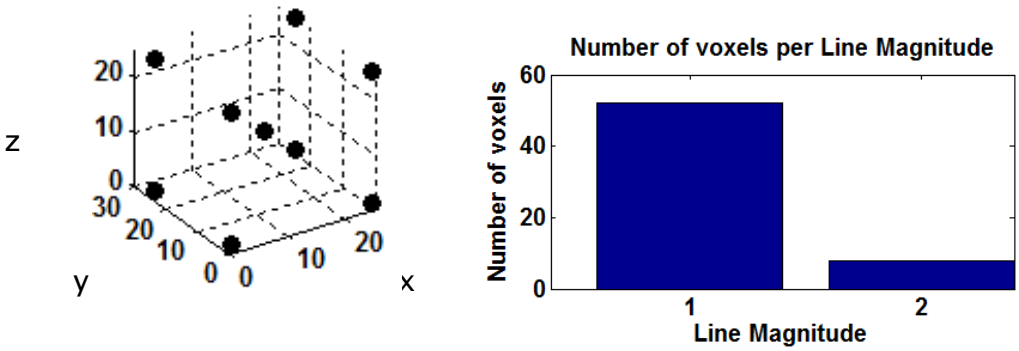

(a) (b)

Figure 3.20 Synthesised cube $\mathbf{V}$ with size of *25x25x25* which consists of nine voxels, (a) 3D scatter of the nine voxels presenting the volume $\mathbf{V}$, (b) Histogram of the number of voxels forming detected lines versus the detected line magnitudes.

3.3.2 Results

To study the performance of the proposed method, a cube $\mathbf{V}$ with size of *25x25x25* and consists of nine voxels was synthesised (Figure 3.20a). The proposed method was used to detect all the possible lines passing through each voxel. The planar accumulator $\mathbf{S}$ has nine planes for each voxel in the volume .The histogram of the detected line magnitudes L in $\mathbf{S}$ indicate that two magnitudes lengths were found Figure 3.20b.

The accumulator $\mathbf{A}$ had two planes, each showing the number of lines detected at each pair of (θ,φ) for every line magnitude Figure 3.21. A sample of the extracted information at every peak in the accumulator $\boldsymbol{A}$ is shown in Figure 3.22, the method performed very well in detecting the lines in the volumetric image.

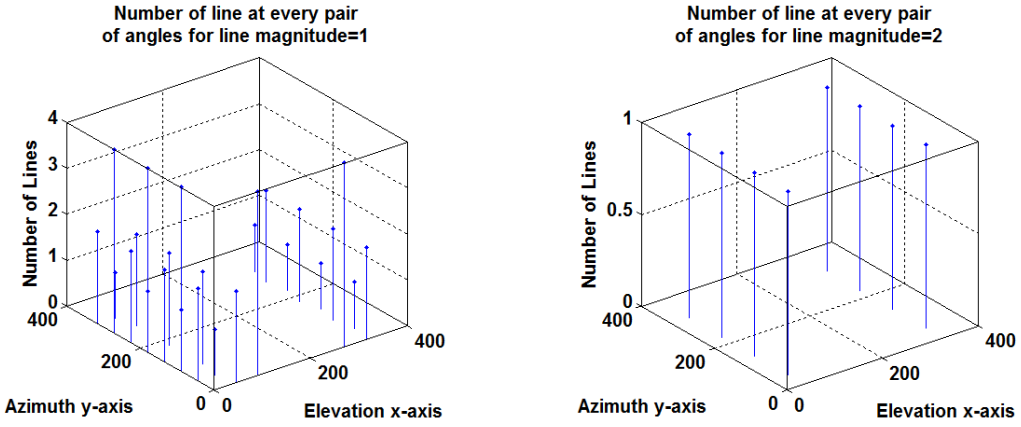

$L_1(\theta, \varphi)$ $L_2(\theta, \varphi)$

Figure 3.21 The planar accumulator S of the synthesized cube of Figure 3.20a showing the number of lines detected at each line magnitude of Figure 3.20b.

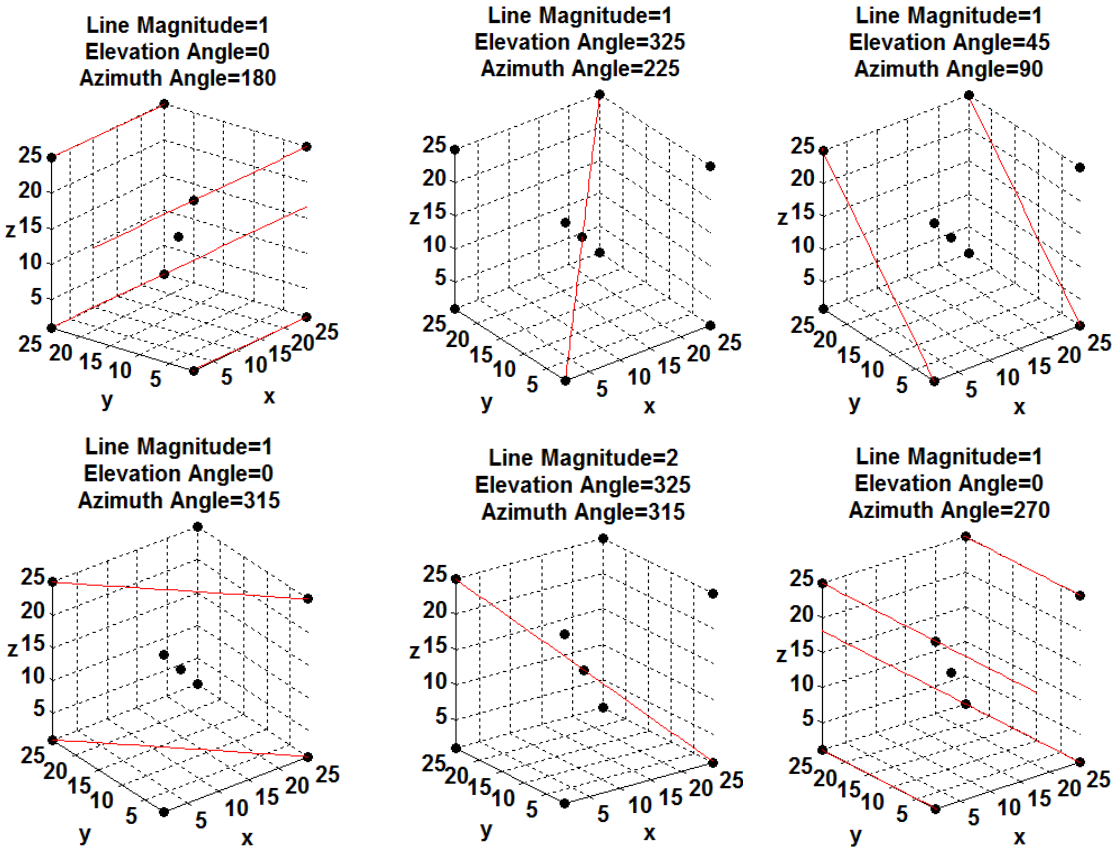

Figure 3.22 Reconstructed lines from accumulator **A** at every line magnitude L_i and the angle pair (θ, φ) associated with it. See Appendix A.

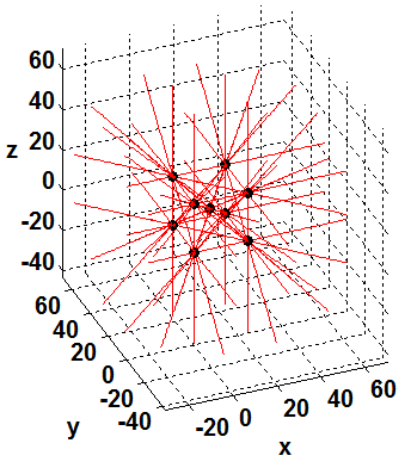

Figure 3.23 Reconstructed lines from the accumulator A at every line magnitude $\mathbf{L_i}$ and the angle pair $(\boldsymbol{\theta}, \boldsymbol{\varphi})$ associated with it combines in one figure.

The result of the combined lines shows that all the possible lines indeed have been successfully detected as shown in Figure 3.23.

To further study the performance of the proposed method, a line **V2** were synthesised in *25x25x25* volume to study the effect of adding salt and pepper noise to an image Figure 3.24 . The line of interest was expected to have the largest magnitude (As there are other scattered lines all other directions in the image with smaller magnitudes).

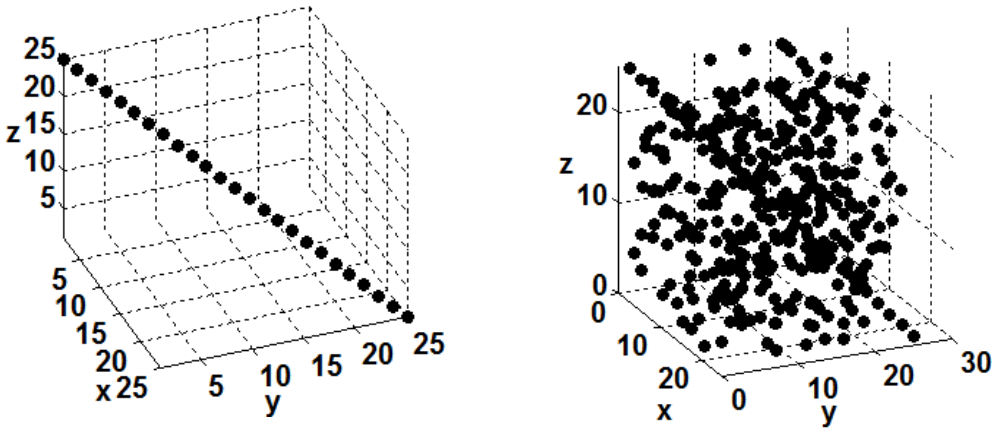

(a) (b)

Figure 3.24 Synthesised line **V2** with size of *25x25x25* (a) 3D scatter of **V2**, (b) 3D scatter of **V2** in salt and pepper noise.

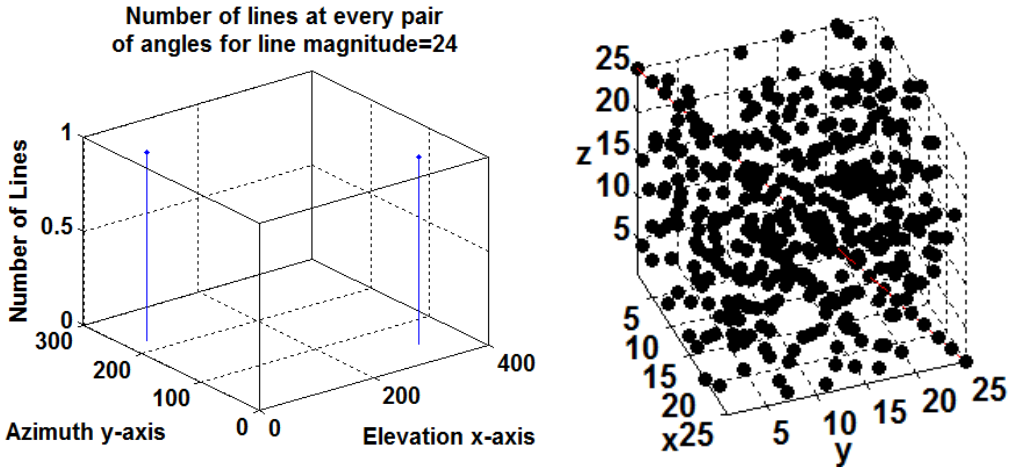

(a) (b)

Figure 3.25 Analysis of the detected lines of **V2** (a) The plane with the largest line magnitude L_{24} in A2, (b) Reconstructed line from the peaks in (a) (red).

The plane of the largest magnitude L_{24} in A2 shows two peaks with size of one, which indicated a single line, detected with two different sets of angles (Figure 3.25a). One of those peaks was reconstructed using the line equation. The reconstructed line was the desired line and indicated a successful detection (Figure 3.25b). In conclusion, the proposed method carries the same noise tolerance by Hough transform.

Another study for the performance took place on an image with zigzag shape spanning through the three-dimensional space as in Figure 3.26. The lines in this zigzag shape show a challenging problem for any line detection because they form a plane rather than scattered set of lines in different directions. Moreover, the lines parallel to one of three axes do not suffer from the digitization as other lines through other angles, which would introduce some error. The magnitude vector suggested seven line magnitudes were detected.

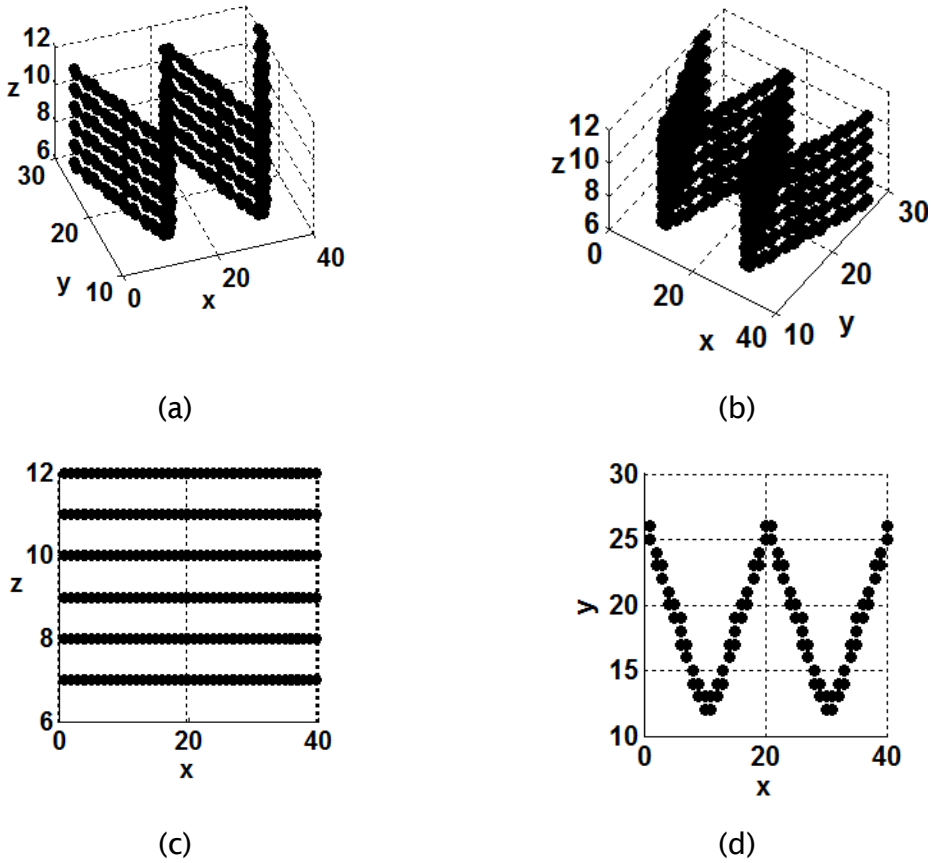

Figure 3.26 Volumetric zigzag shape **V3** with different views

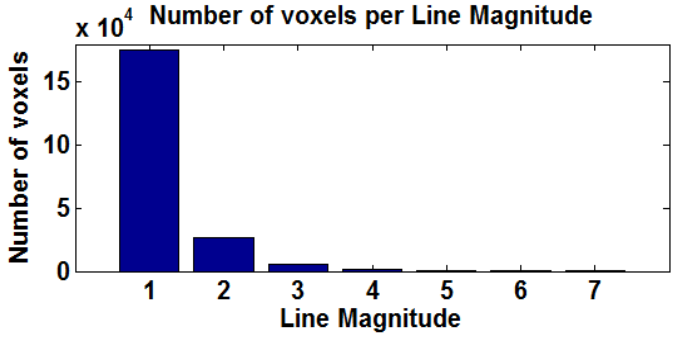

Figure 3.27 The line magnitude vector of the shape in Figure 3.26 shown as a histogram of line magnitude versus the number of voxels

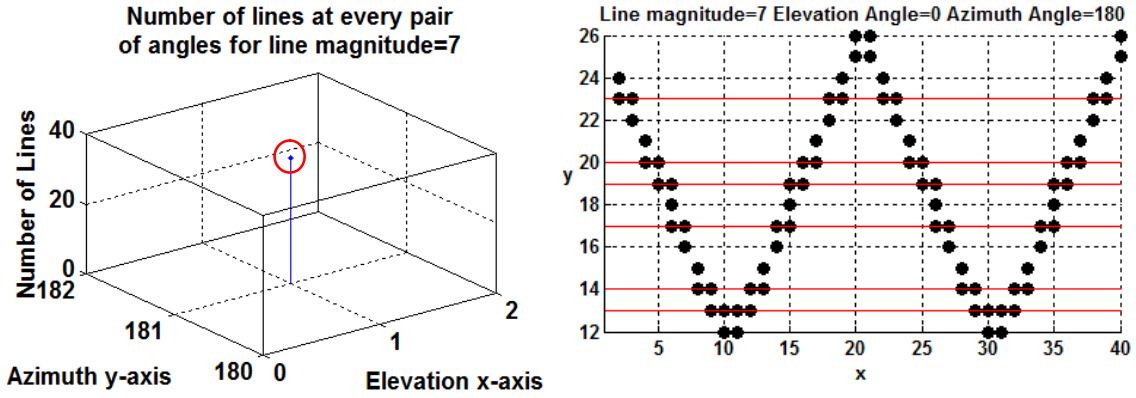

(a) (b)

Figure 3.28 Analysis of the detected lines of **V3** (a) A plane from in *A3* with the line magnitude L_7 (b) Reconstructed lines from the highlighted peak $L_7(180,0)$ in (a)

The top plane in the $A3$ accumulator gave the largest line magnitude detected at $L_7(\theta,\varphi)$ Figure 3.28. Thirty-six lines were found sharing the same pair of angles (0,180). Those Lines were detected using the method proposed and highlighted them as significant lines with a large magnitude on the other hand for the untrained human eye this line can be rejected as insignificant line.

Plane $L_6(\theta,\varphi)$ introduced other marginally significant peaks with number of lines detected of twelve (Figure 3.29). Those lines show the effect of digitization on lines that are not parallel to one of the axes. The line could be described by the detected line but with some error. The next Plane $L_5(\theta,\varphi)$ introduced important peaks with large number of eighty four lines. The lines present the planes forming the zigzag shape. Again those lines lay on one of the axes hence the large number of lines detected (Figure 3.30).

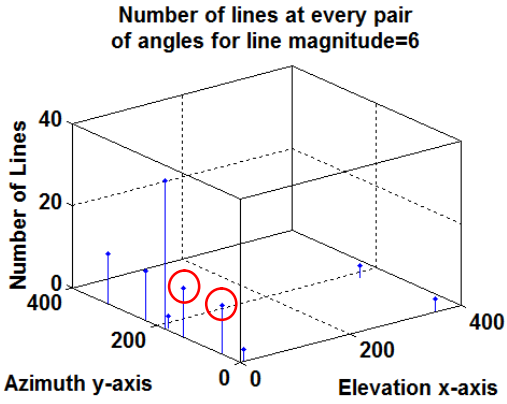

(a)

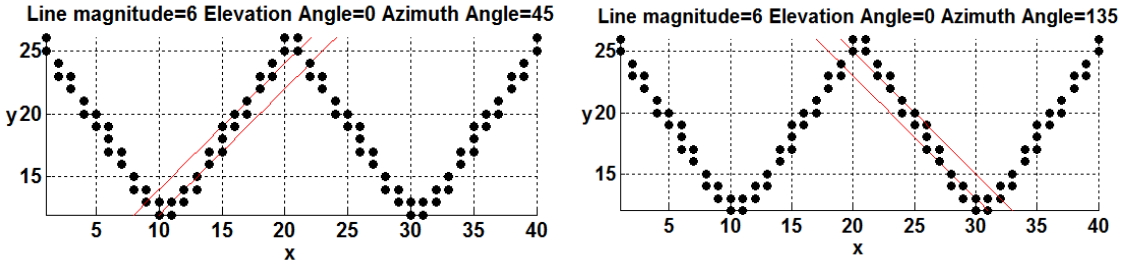

(b)

Figure 3.29 Analysis of the detected lines of **V2** (a) A plane from in A3 with the line magnitude L_6 (b) Reconstructed lines from the highlighted peaks $L_6(45,0)$ and $L_6(135,0)$ in (a)

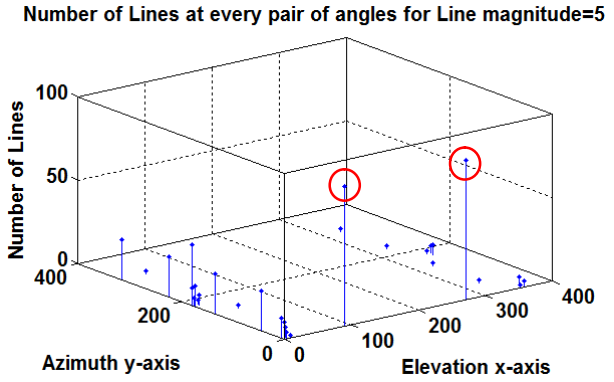

(a)

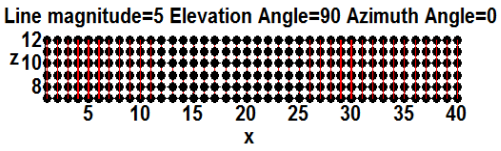

(b)

Figure 3.30 Analysis of the detected lines of **V2** (a) A plane from in A3 with the line magnitude L_5 (b) Reconstructed lines from the highlighted peak $L_5(0,90)$ in (a)

Now the most interesting plane $L_4(\theta,\varphi)$, which shows a significant increase in the number of lines detected at the same pair of angles of line peaks detected in $L_6(\theta,\varphi)$ and two new peaks at new locations all with number of lines detected of forty two (Figure 3.31). The new peaks showed the most accurate interpretation for the direction of the lines forming the zigzag that we are interested in. The analysis on the given zigzag shape showed that the digitization causes the straight line to be interpreted by the proposed method as smaller lines, which affect the expected magnitude.

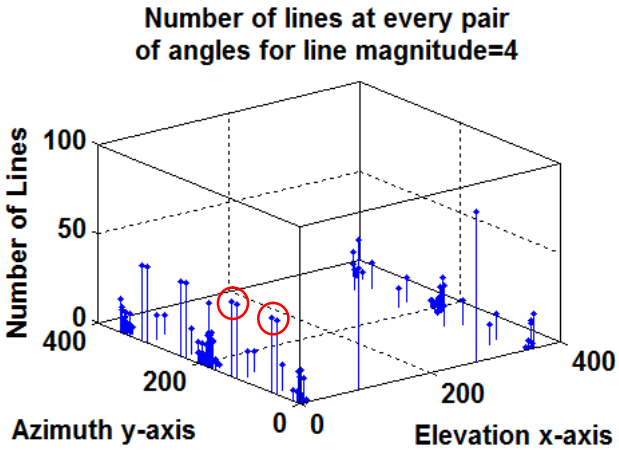

(a)

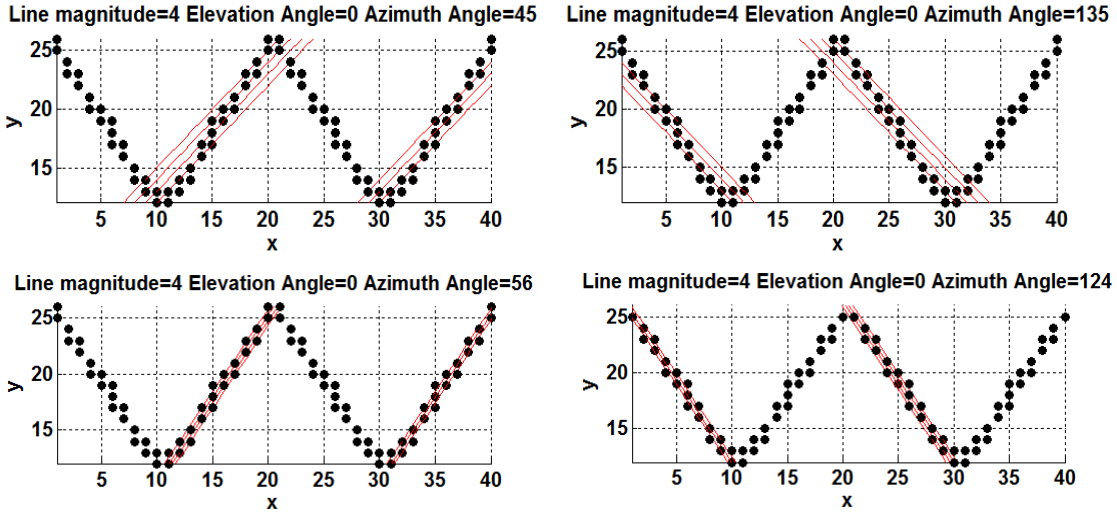

(b)

Figure 3.31 Analysis of the detected lines of **V2** (a) A plane accumulator of line magnitude L_4 (b) Reconstructed lines from the highlighted peaks $L_5(45,0), L_5(135,0), L_5(56,0)$ and $L_5(124,0)$ in (a).

The proposed method is then applied to a real CT image (Figure 3.32), after applying 3D Sobel operator and simple manual threshold to separate the piston from the block engine. The piston magnitude and direction are the main objects of interest, as they were expected to form a relatively large line. The surrounding material is likely to interfere with the detected line magnitude and direction especially at the extreme angles with an increment of 90 degrees from the axis in all directions. The magnitude vector L (Figure 3.33) showed that the largest line magnitude detected is 19 but the line corresponding to this magnitude laid on one of the extreme angles. The only significant peak with a direction other than the extreme angles was highlighted in (Figure 3.34).

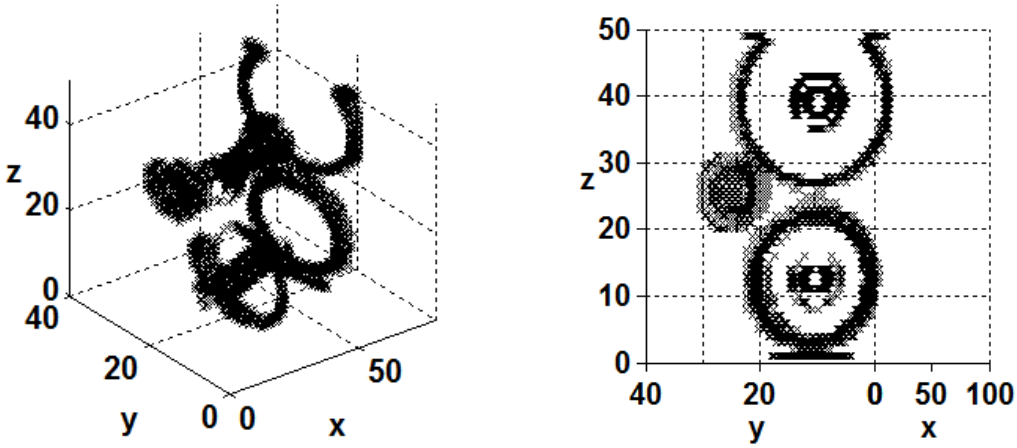

Figure 3.32 Different views of 3D scatter for computed tomography of an engine block **V4** after applying Sobel operator and a manual threshold.

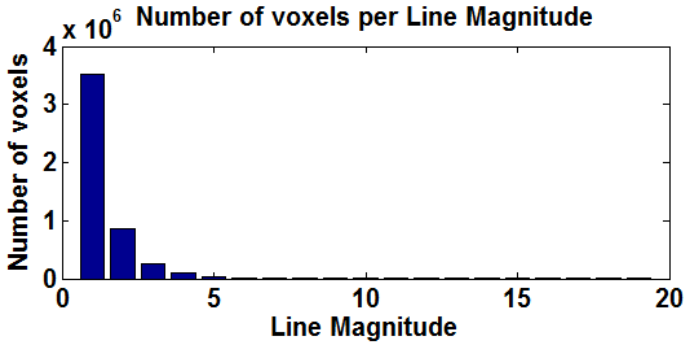

Figure 3.33. The line magnitude vector of the shape in Figure 15 shown as a histogram of line magnitude versus the number of voxels

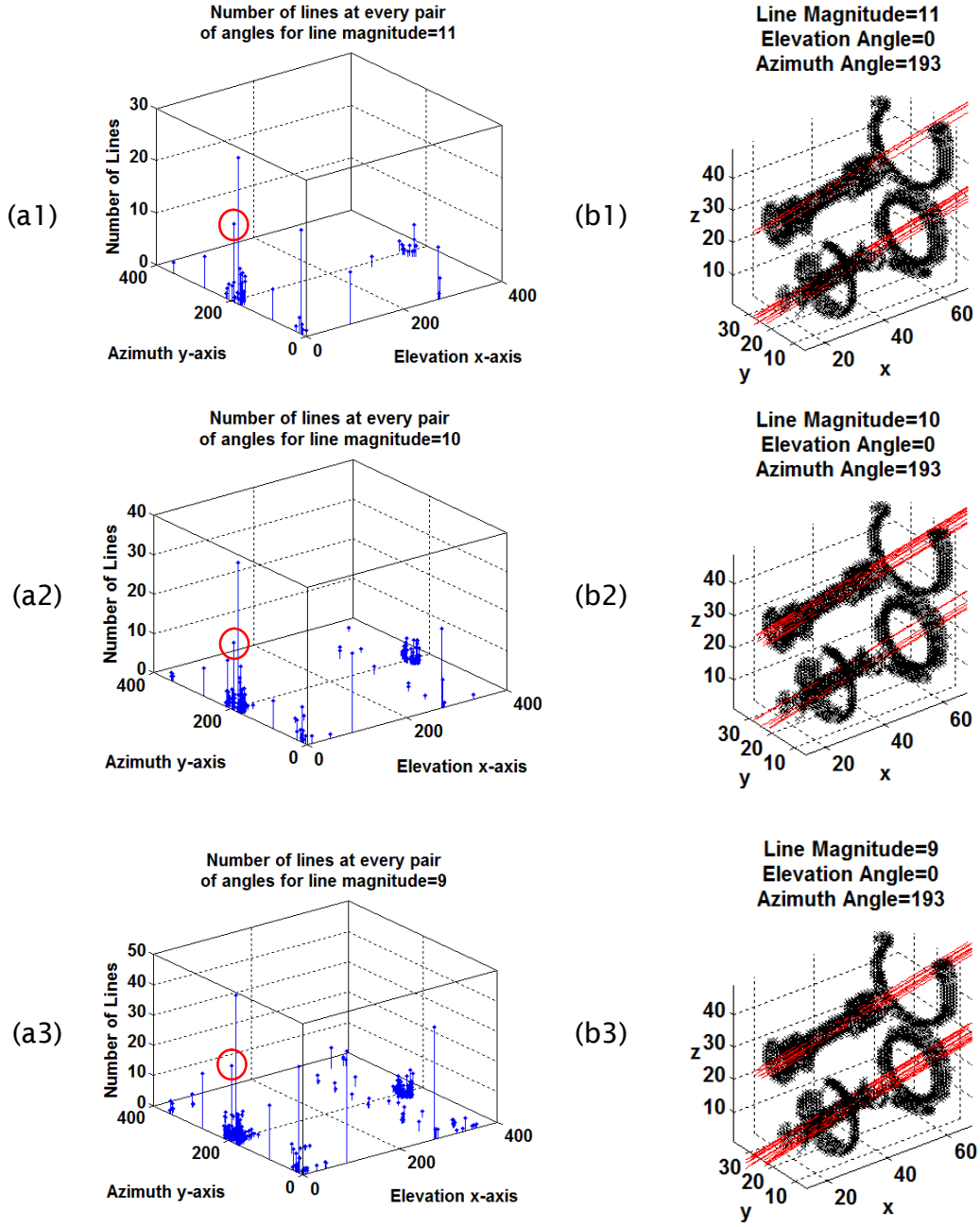

Figure 3.34 Analysis of the detected lines of **V4** (a1)-(a3) planes from a with the line magnitude ranging from L_{11} to L_9 (b1)-(b3) reconstructed lines from the highlighted peaks from (a1) to (a3) respectively

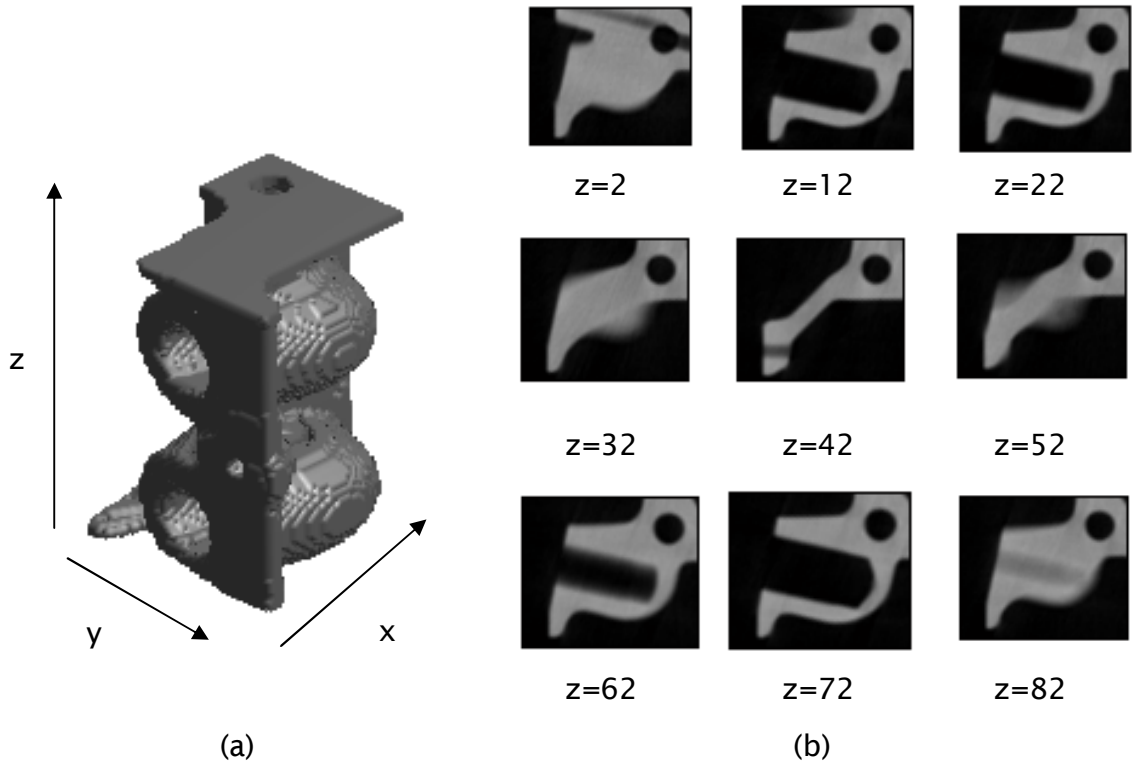

Figure 3.35 Engine segment with two cylinders of the same radius (a) 3D render (b) nine slices through the segment

This peak was traced and appeared at magnitudes from 11 and smaller at the same pair of angles. Lines forming the piston cylinder were reconstructed and their magnitude range and direction were found.

The proposed line Hough transform can also be employed to the axis detection in Sections 3.2.1 and 3.2.2. The cylinder axis detection methods have been applied to the engine block of (Figure 3.35).

By setting the radius to 11 voxels to decrease the computational expense, the axis of each cylinder has been detected and shown in (Figure 3.36a-b). Applying line Hough transform to the detected axis revealed the cylinder length and the cylinder pair of angles in 3D space as in Figure 3.36c-e.

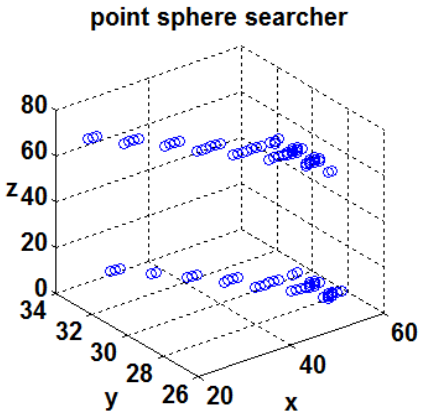

(a)

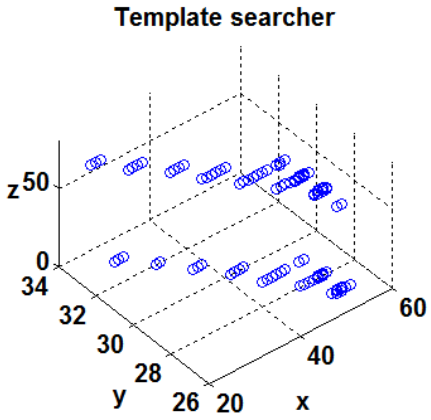

(b)

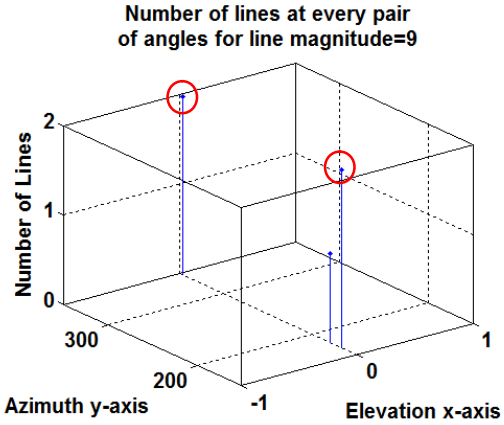

(c)

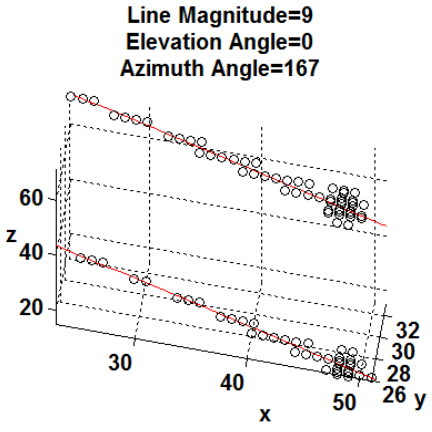

(d)

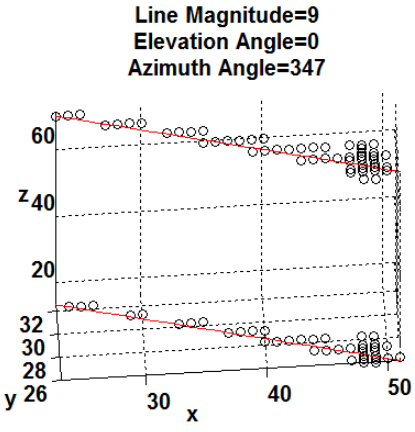

(e)

Figure 3.36 The results of applying the Line Hough transform on detected axis of the cylinders in (Figure 3.35), (a)-(b) Thresholded accumulators of point sphere searcher and template searcher, respectively.(c) The largest lines detected based on Line Hough. (d) and (e) Reconstructed lines based on the angle pairs in highlighted in (c).

3.3.3 Discussion

As mentioned in the literature overview, many have proposed Hough transform based methods for plane detection in three-dimensional space but few have tackled the problem of line detection due to its complexity, which require by definition a four-dimensional accumulation space. The method proposed here gives a new perspective to the problem different than what has been proposed by other authors (Bhattacharya et al., 2000; Sarti & Tubaro, 2002; Overby et al., 2004)

The novelty of the proposed method concerns a new technique that simulate the effect of fitting an infinite sphere at every point in the three-dimensional space and accumulate the normal to the surface of the sphere. The process takes place by shifting the origin at every point and converting the coordinate system to spherical coordinate. The results were significant and reliable.

The present results are significant in two major respects; the mining for line existence within a noisy volume image, and detection of lines with a good tolerance for gaps. The present findings appear to be consistent with the original Hough transform. The main advantage for Hough transform is the ability to extract information in a scene where the line is contaminated by noisy data, which is where computers can offer excellent performance, in comparison with the human vision. The other advantage is the tolerance for any shortcomings in the data and the missing information omitted by occlusion. Both advantages were inherited by the proposed method; the only key difference is the Hough space complexity due to the used framework to simplify the visualization.

One of the issues that emerges from the results is lines that are parallel to an axis can result in extreme peaks in the accumulator which can affect the visualisation and detection processes. Another issue is how accumulator space enhancement is not possible through filtering processes (such as smoothing) since the peaks are discrete and any change in the accumulator would affect reconstruction. One solution could be to use another version of the accumulator to aid peak detection but this is beyond the scope of this research and is left for future research.

It should be noted that the memory demand (storage and speed) for the proposed method depends on the number of voxels in the image. The linear relation between the number of voxels and the size of the stack of planes $\mathbf{S}$ is a new problem unique to the proposed method and cannot be avoided if line length is needed as a parameter. The stack of planes $\mathbf{S}$ holds the voxels addresses and the votes (or magnitude) for each pair of angles (θ, φ). The literature was only concerned with finding line direction hence an easier computation expense.

3.4 Conclusions

In this chapter, several new ideas have been proposed to detect geometrical shapes in volumetric images based on accumulating votes from the parameters of the target shapes. The current increasing interest in 3D imaging systems due to the decrease in their memory demand, price and size is likely to translate to the desire for a standard method that can provide results that are as reliable and accurate as the well-established spatial methods. Three-dimensional volumetric methods are not yet available in standard image programming libraries unlike their two-dimensional counterparts. The literature is still developing those ideas to bring them to operational capability. The proposed ideas in this chapter seek to detect geometrical shapes from their voxel information as it was originally introduced in (Duda & Hart, 1972; Illingworth & Kittler, 1987) rather than surface normals of segmented image (Rabbani & Heuvel, 2005; Camurri et al., 2014).

The shape detection process can be much easier in terms of computational demand if aided by segmentation methods. Segmentation as pre-step for shape detection can be of great benefit and in the next chapter, we proposed a new intuitive three-dimensional segmentation method based on pressure analogy.

Chapter 4: Pressure Analogy in Feature Extraction

This chapter concerns the automated analysis of multiple objects in volumetric scans. The analysis will not focus on shape, as in the previous chapter, but on methods to separate the shapes for later analysis. The chapter will first describe a basic approach, and then its extended version. As the vehicle for analysis, we shall use the Roman hoard of coins described earlier Figure 1.1 and analyse it aiming to count the number of objects that can be disconnected within the volume. In the extended version, we shall analyse volumetric scans of femur bones, aiming to separate the bones from the tissue and objects that surround them when scanned on patients. We shall show how this separation process can be achieved; leading to accurate automated measurement of femoral bone parameters. We shall also describe how the extended technique can provide enhanced operation on the Roman hoard. We shall start by describing the use of pressure as an analogy used for developing an image processing operator that can separate objects in volumetric scans without knowledge of their shape.

4.1 Simple Pressure Analogy

Computed tomography (CT) imaging is an increasingly popular source of information about three-dimensional objects, with many applications ranging from medical to industrial. Scans can contain multiple objects with the same density or single objects containing smaller ones with similar density. The placement of the objects in the 3D space can be random and in some cases the surfaces of those objects touch which makes it difficult to separate them for analysis/ visualisation using conventional thresholding and segmentation techniques, motivating development of a higher-level process. An example of such a problem is the CT scanned jar (Figure 1.1), which contains the set of Roman coins, described earlier. This set of data contains coins with similar density randomly placed with different

orientations and locations within the jar. The problem associated with this particular set of data relies in the high attenuation factor for the material from which the coins are made which in turn increases the chance of touching surfaces in the volumetric image especially for the coins in the centre of the jar. Separating objects with the same density and texture is challenging due to the absence of techniques for detecting the regions of intersection between the objects in 3D, impeding the possibility of counting the coins.

Many approaches have been developed to solve the problem of separating touching objects in two-dimensional (2D) space. The two main applications are concerned about separating rice grains (Yao, Zhou, & Wang, 2010) and counting cells in microscope images (Nasr-Isfahani, Mirsafian, & Masoudi-Nejad, 2008). A traditional approach involves thresholding, corner detection and joining points of interest to create a binary image of disconnected objects. However, so far no attention has been paid for techniques to separate touching objects in 3D images (Wirjadi, 2007). The literature provides some model-based methods that have been used to separate left and right lungs (Hu, Hoffman, & Reinhardt, 2001). The search for regions of interest uses images where lungs intersect, to minimize the computational demands. Other methods such as edge or surface detection can be used to properly segment objects in 3D space such as 3D Marr-Hildreth operator (Bomans, Hohne, Tiede, & Riemer, 1990) but unfortunately those methods do not address the touching regions. Using approaches based on connectivity would consider both surfaces as a single entity. It might be possible to achieve some results by morphological analysis but such procedures are isotropic and do not adapt to local scenarios. Three-dimensional Watershed segmentation is another candidate for such problems, it provides water analogy in which the objects in the image contain basins that would be flooded with water to define an image segment (Meyer, 1994; Russ, 2006). A comparison between what is introduced in this chapter with watershed will be presented later on in this chapter.

We present a novel 3D approach based on using a physical analogy (M. S. Nixon, Liu, Direkoglu, & Hurley, 2009) to separate intersecting regions. The approach is anisotropic and does not require a model or previous knowledge about the regions of interest. It can be applied automatically so as to delineate intersecting structures by adapting locally to image content. As such the images are then rendered suitable for later analysis procedures. The analogy used is pressure, and the approach does

not mimic application of pressure precisely, and more to develop a new method to separate touching objects, in 3D, which allows in this case for the automated analysis of the Roman hoard of coins. Unlike the Watershed analogy, which tackles the segmentation process by considering the shape, the proposed analogy is applied to the background that surrounds the objects.

4.1.1 Method Development

Multiple objects in a volumetric image, which have the same intensity, are common in CT scan. Separating them can usually be achieved by using a thresholding operation, such as (Otsu, 1979), unless the objects surfaces are close together or touching. The area between touching objects in a CT scan image defines a very fine gradient caused by X-ray refraction exacerbating difficulty in segmenting the individual objects.

On the other hand, Otsu thresholding can remove the background well. Since the objects of interest are solid, the histogram will show a well-defined peak where the objects exist, extracting this peak would help in creating a consistent background. Having separated the background, the objects need to be separated. To achieve this, a physical analogy has been used to measure the local pressure in the background which, has been considered to be filled with an ideal gas and governed by the following equation:

$$PV = nRT \tag{4.1}$$

Here the number of moles (n), temperature (T) and ideal gas constant R are constant. An inversely proportional relation between the pressure and the volume is created. To use this as an image processing operator, the pressure at each background point $\mathbf{P}_{x,y,z}$ is accumulated within a window $\mathbf{W}$ as

$$\mathbf{P}_{x,y,z} = {}^{1}\Big/_{\sum_{x,y,z\in\mathbf{W}} \mathbf{V}_{x,y,z}} \quad \forall \mathbf{V}_{x,y,z} \in \text{background} \tag{4.2}$$

where $\mathbf{V}$ is the volume of interest. The values of $\mathbf{P}$ are then thresholded to suggest where maximum pressure occurs.

$$\mathbf{M}_{x,y,z} = \begin{cases} 0 & \text{if } \mathbf{P}_{x,y,z} \geq \text{threshold} \\ 1 & \text{otherwise} \end{cases} \quad 4.3$$

This provides a mask $\mathbf{M}$ which can be used to eliminate voxels in the original image $\mathbf{V}$. The separated image $\mathbf{S}$ is then

$$\mathbf{S}_{x,y,z} = \mathbf{M}_{x,y,z} \times \mathbf{V}_{\mathrm{x,y,z}} \quad 4.4$$

4.1.2 Results

To illustrate the proposed method, it has been applied to two touching synthetic disks (slices at different depths are shown in (Figure 4.1). Using Otsu thresholding revealed only a single object in the image. The pressure domain is then calculated for the disks using local pressure (Figure 4.2). The window size has been chosen to be *5x5x5* to have a relatively acceptable signal to noise ratio; smaller windows would endure high noise and low levels of pressure on the other side larger windows would provide larger pressure levels but less localized search. Based on the window size a proper threshold is applied to create a mask of the inverse of the touching area. The mask is then multiplied by the image to separate the disks (Figure 4.3). The histogram of elements shows a new object, which indicates a successful separation.

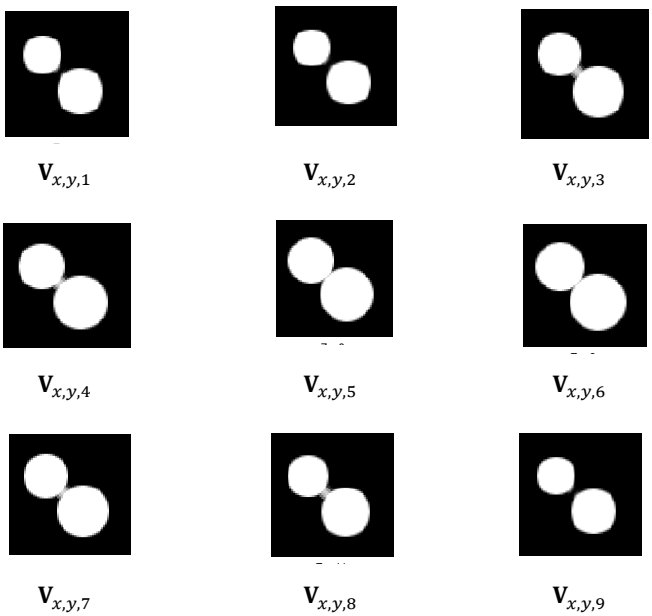

Figure 4.1 Nine slices through synthetic image of two touching disks with small gradient between them.

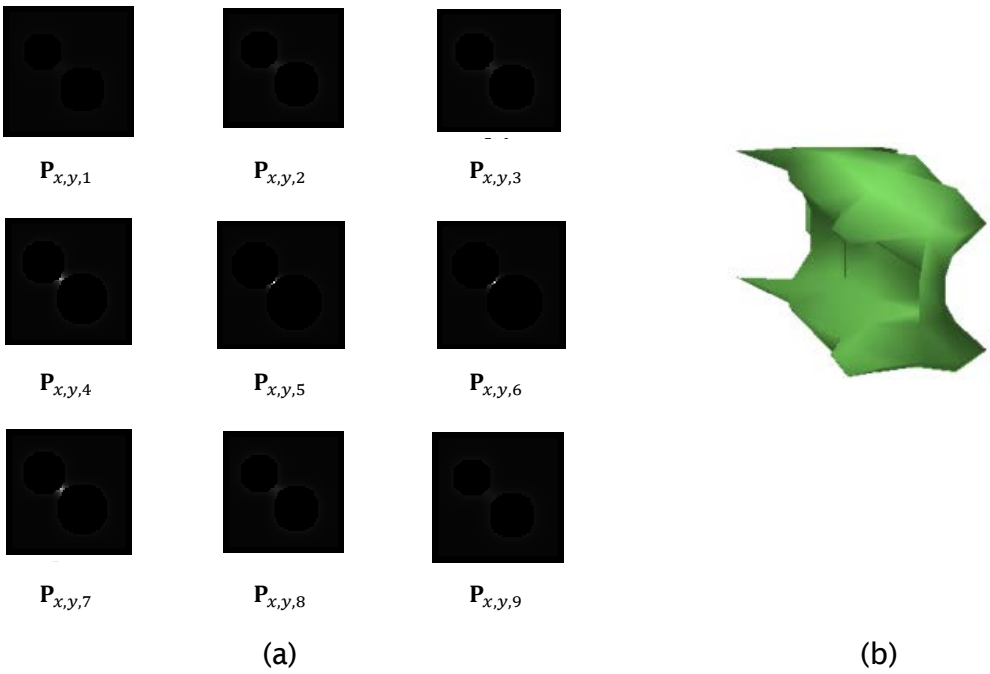

Figure 4.2 Pressure domain (a) Nine slices of pressure domain **P** (b) Rendered thresholded pressure domain **M**.

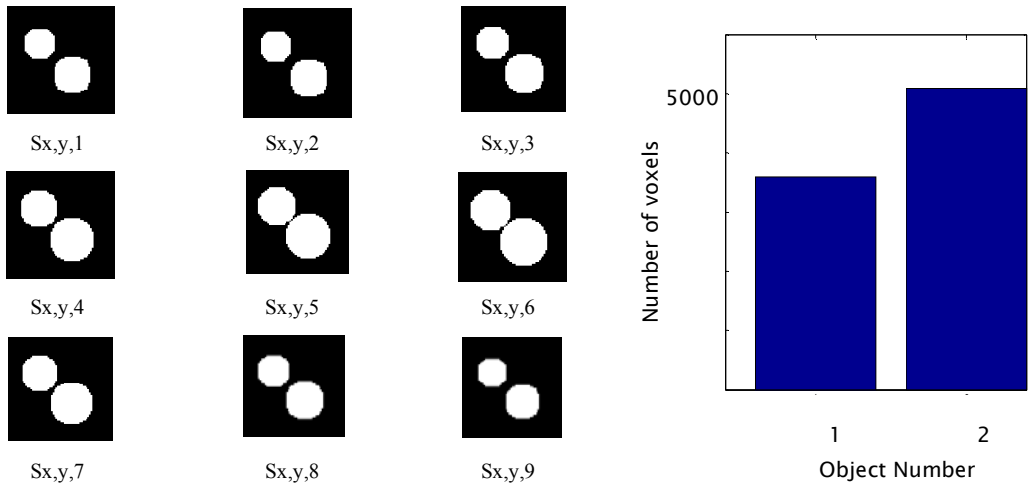

Figure 4.3 The result of multiplying the image with the pressure mask Figure 4.2b (a) nine slices through the separated image **S**, (b) Histogram of number of voxels per element after applying the pressure mask to the synthetic disks showing a detection of two objects.

For the image of Roman coins (Figure 1.1) the equal density of the coins and the noise present a great challenge. The volumetric image is of resolution $444 \times 463 \times 411$ and was derived using microfocus CT. The direct application of Otsu thresholding detects only a single object (Figure 4.4), which shows detection of a

single, large, object). Otsu thresholding was applied as a first step to the proposed method to remove the background. Additionally, a peak-based threshold was applied to the intensity histogram to further separate the object from the background.

The pressure domain was calculated and thresholded to create a logical mask, Figure 4.5a, which is used to discard areas with certain pressure and thus the touching regions. Finally, labelling and connectivity check performed to present the detected objects in a histogram, derived from Figure 4.5b. The new histogram of objects shows that a large number of objects are detected within the set of Roman coins now that the regions where the coins touch have been excised. Objects with volume smaller than the mean volume have been removed to clearly identify significant elements among the histogram Figure 4.6. A sample of the objects related to those points is rendered in (Figure 4.7). This shows that the coins separation has indeed been successful and that single coins are now derived. Beyond selection of an appropriate threshold there are no other parameters associated with the new technique.

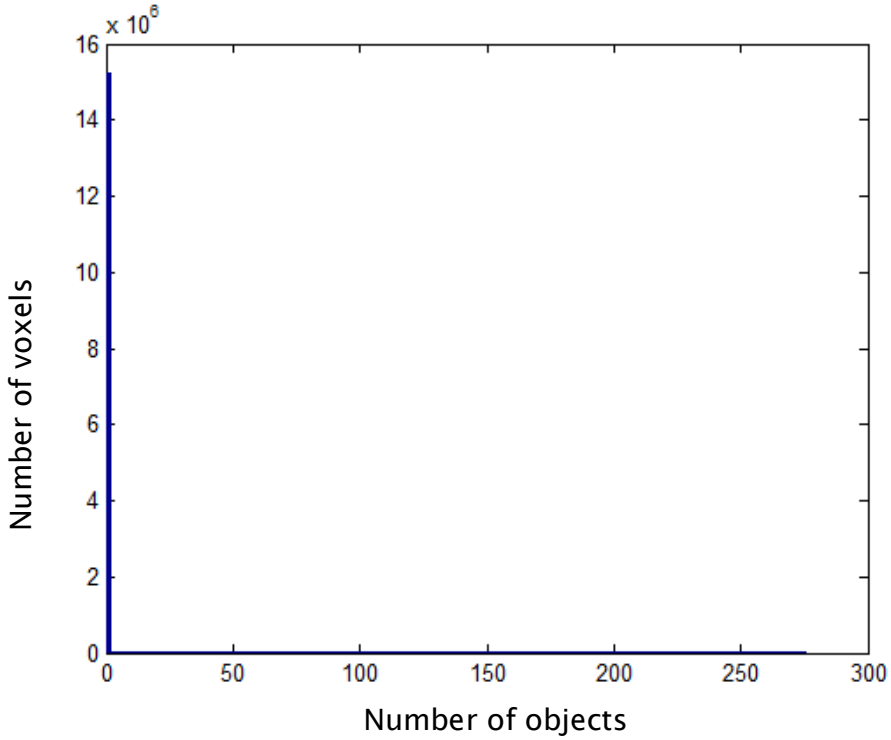

Figure 4.4 Histogram of the connected objects after applying Otsu threshold to the Roman coins.

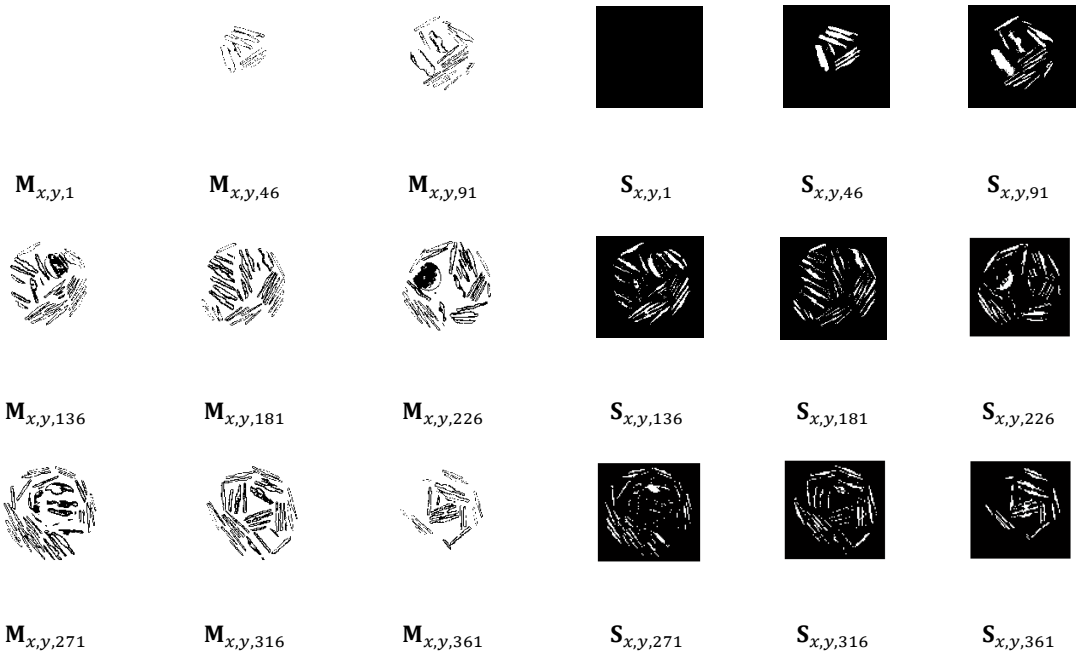

Figure 4.5 Nine slices through (a) Thresholded pressure mask $\mathbf{M}$, (b) Roman coins after application of the pressure mask $\mathbf{S}$.

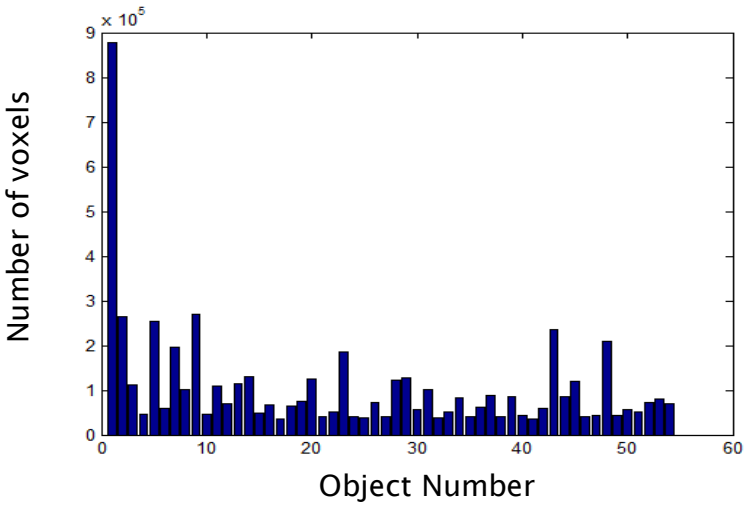

Figure 4.6 Histogram of the connected objects after applying the pressure mask to the roman coins and removing the mean volume.

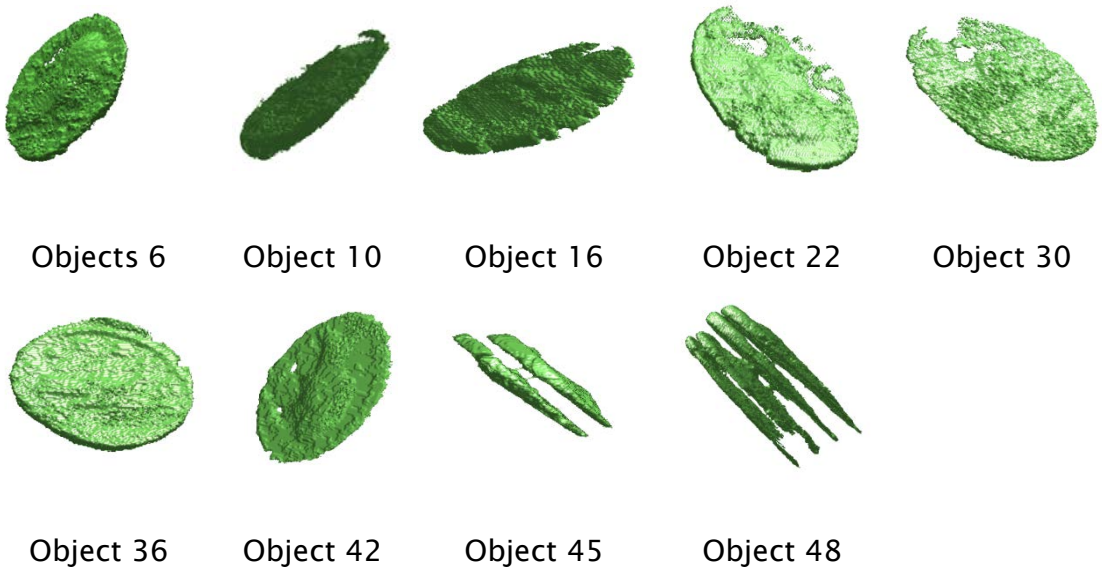

Figure 4.7 Nine roman coins extracted from the peaks in Figure 4.6

CT images usually suffer from two types of noise: random noise caused by photon generation and noise introduced by the sensitivity of receptor but to furthermore study the effect of noise on the new method, volumetric Gaussian noise has been added to the volumetric image with increasing variance, Figure 4.8a. The number of correctly segmented objects is inversely proportional with the increase of noise (Figure 4.8b) and within acceptable tolerance. The noise does naturally affect segmentation, but clearly is not bad.

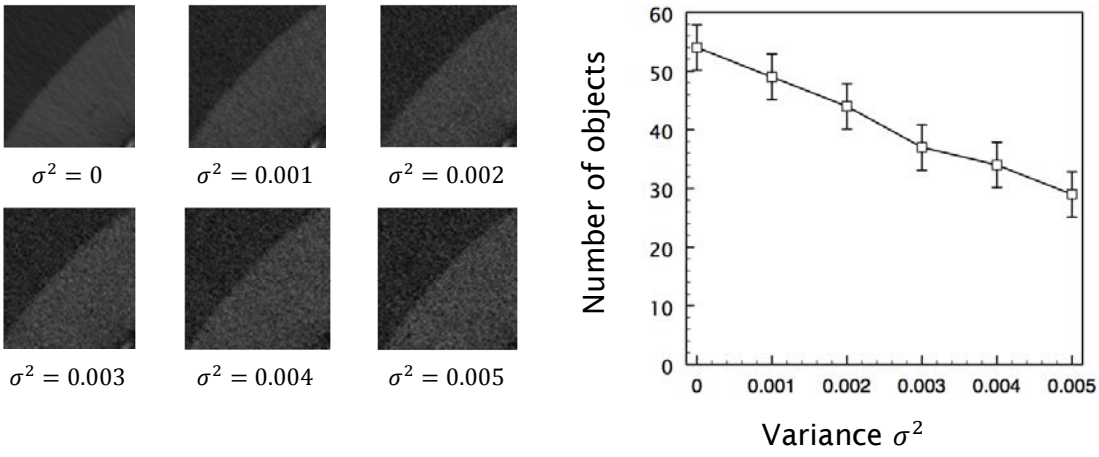

(a) (b)

Figure 4.8 Noise analysis on the performance of the proposed method (a) A crop of coins image after noise introduction with different variance values, (b) Number of objects detected versus the noise variance

A slice from the result of segmentation using 3D watershed segmentation is presented in (Figure 4.9). Several techniques exist as a pre-processor to Watershed segmentation; one method depends on the distance transform of the thresholded image (Gonzalez, Woods, & Eddins, 2002) and the other relies on minimal suppression to decrease the over-segmentation by discarding shallow basins (Russ, 2006). Watershed without suppression showed over-segmentation that divided the shape into smaller parts, on the other hand the suppression method showed better result toward the over segmentation but inaccurate outlining for the shape of interest.

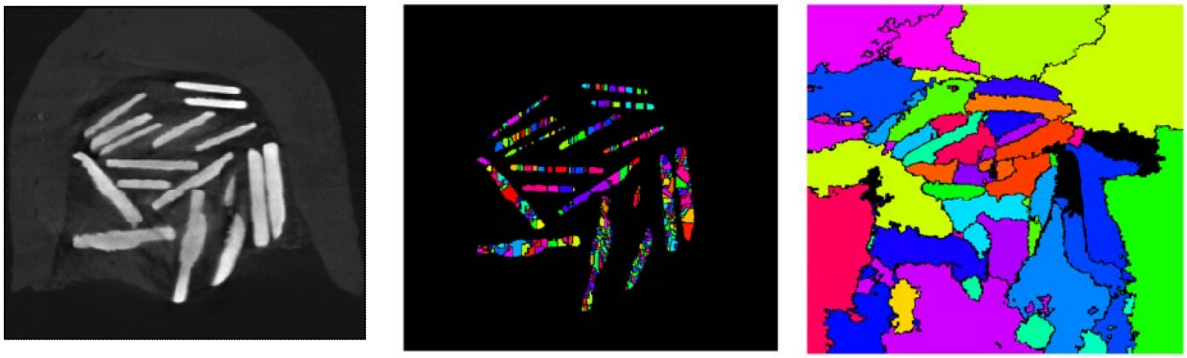

Figure 4.9 Watershed segmentation applied on the coins of Figure 1.1 (a) Slice number 85 investigated from the original volume, (b) Watershed segmentation after thresholding and application of distance transform, and (c) Watershed segmentation after minima suppression to decrease the effect of over segmentation.

In comparison with the result of pressure method for the same slice (Figure 4.10), pressure presented better results in terms of labelling the object but failed in areas where the connection between the objects has similar density, which caused under-segmentation. Also the pressure results showed an eroded object surface caused by the pressure mask, which can be easily overcome by growing the result on the thresholded image (this will be discussed further in Section 4.2.

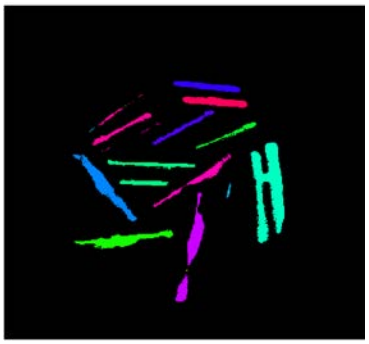

Figure 4.10 Slice 85 from the pressure analogy segmentation applied to Figure 1.1 showing each object detected in specific colour.

The main concern associated with the proposed method is the dependence on the local features and consistency in the density of the object of interest; however the application on a CT scanned orange (which has a low density and tightly connected pieces (Figure 4.11a) also demonstrated successful segmentation results as shown by the number of segmented objects in the histogram in Figure 4.11b and the render of those segmented objects Figure 4.11c.

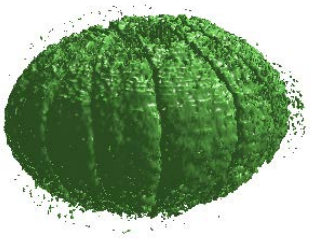

(a)

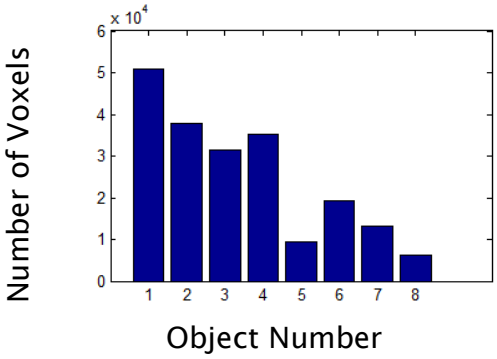

(b)

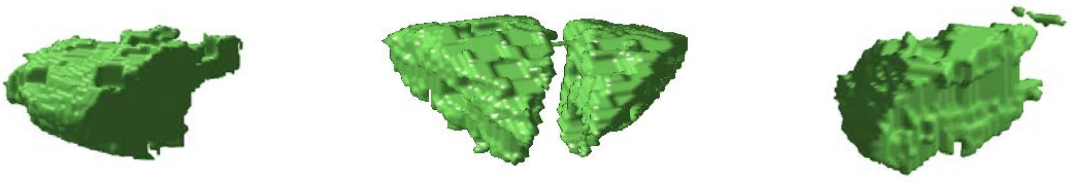

Object 3 Object 4 Object 7

(c)

Figure 4.11 An example to show the effectiveness of the proposed method on a CT scan on a pealed orange (a) Rendered CT scan of an orange, (b) Histogram of the connected objects after applying the pressure mask to the orange image, (c) Rendered objects extracted from histogram (b).

4.1.3 Discussion

Pressure analysis has shown promising results for separating touching objects with the same density in CT images given that the touching is has different density. The results show that it can clearly improve analysis over traditional techniques, on a selection of images. The new method is automatic, anisotropic, non-iterative and does not require a template nor knowledge of a target objects' shape. The results depend significantly on the local features in the original image and the threshold used for the pressure domain. One observation would be the objects with smaller touching surface area appear to have been extracted better than the others with larger areas of intersection. As such, by using the analogy of gas pressure we have a new technique, which can be used to approach a known problem in (3D) image analysis.

The only limitation of the proposed method is the inability to discriminate an area between two objects with a density value similar to the objects' own density. One example of such a problem can be seen in CT image of the area between the femur bone and the hipbone, where the cartilage diminishes with time. Several slices of the connected areas between the femoral head (which is near spherical, near planar in cross section) and the acetabulum (which is its socket) of one volume are shown Figure 4.12. Both the acetabulum and the femoral head (and some veins) are shown to be white and the remainders of the CT images are shown in grey. In these images, the connections appear in different places, so a technique to separate them requires information from local features. Another problem also arises, in that there are multiple contact areas between the veins in the surrounding soft tissue which touching the femur, especially when a contrast agent is present. However, veins have little impact on the total surface area, as in Figure 4.13.

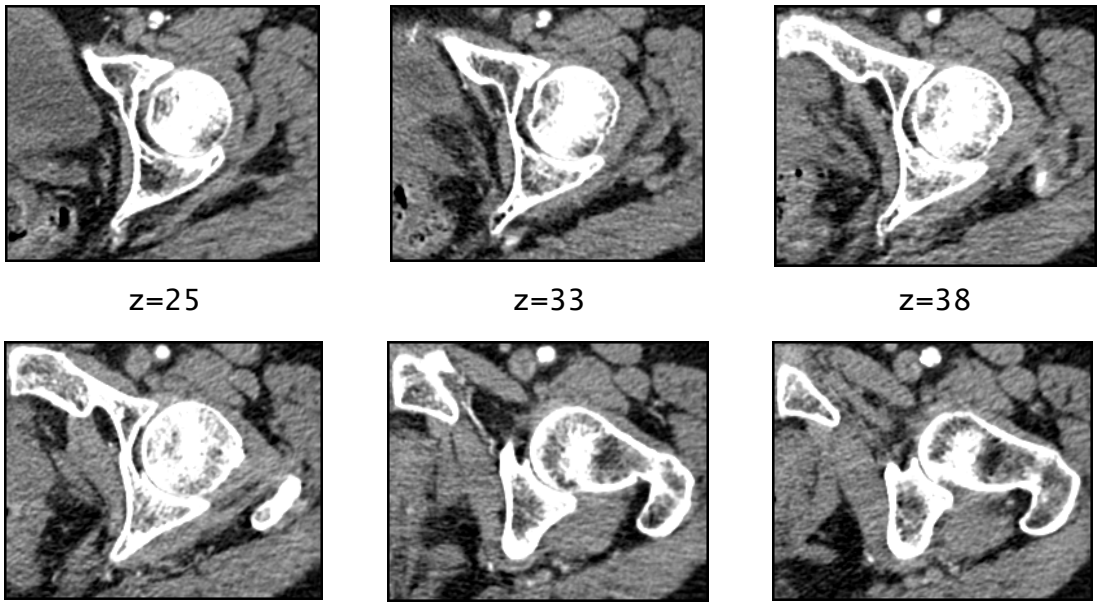

Figure 4.12 Different slices through the hip showing the contact area between the femoral head and the acetabulum

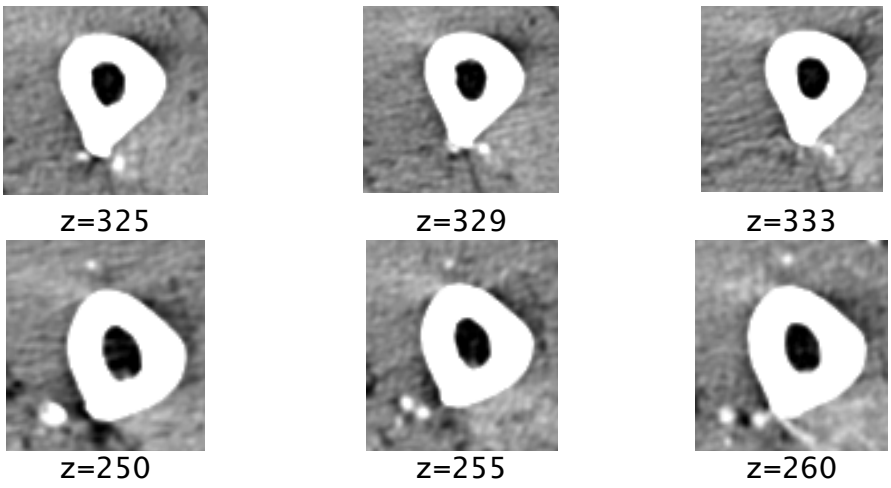

Figure 4.13 Different slices showing the different contact areas between the femur bone and the surrounding veins that may interfere.

The pressure approach presented in this section does not provide a mask capable of separating those areas as shown in Figure 4.14. Here, the thresholded pressure is highlighted in pink and not all of the intersecting area is highlighted, shown in particular in the image for z = 33 and z=38. The inability to distinguish this area of intersection motivated enhancements to overcome this problem, which are proposed in the next section.

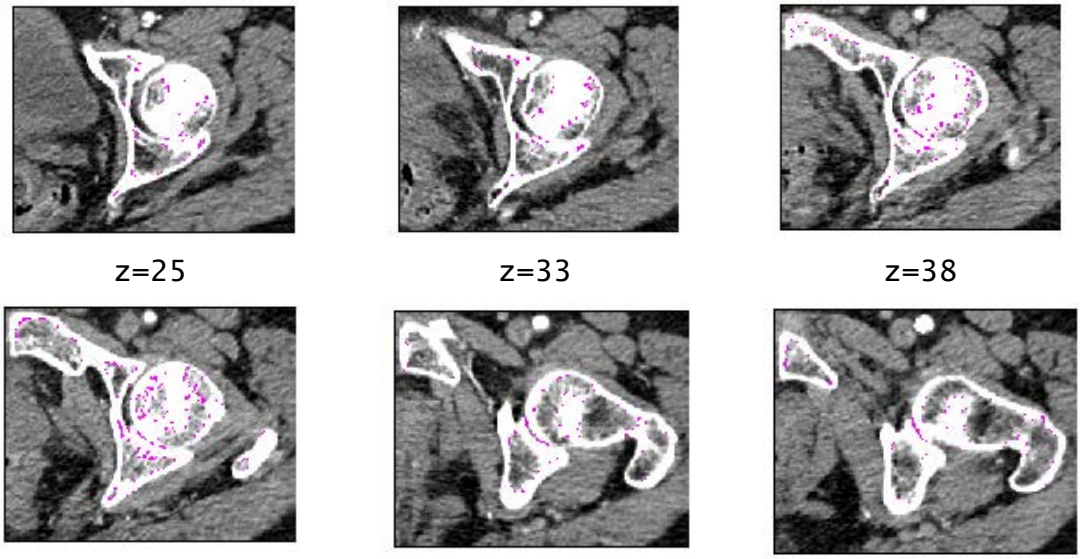

Figure 4.14. Thresholded pressure highlighted in pink on the slices of Figure 4.12 with, showing how the pressure incapable of disconnecting the joined area between the femoral head and the acetabulum.

4.2 Enhanced Pressure

Image segmentation is a valuable source of information for pre-clinical procedures. Due to the limitations in some scanners like the low resolution and low contrast, separate objects may appear as a single entity with exactly the same intensity value. The pressure analogy proposed in Section 4.1 provides a solution for the case in which there exist a small gradient between the two objects but would face a challenge if the objects are connected with the same intensity value between them.

Hip replacement operation is a great example for such preclinical operation. Osteoarthritis, which is one of the most common types of arthritis, is a disease that causes the distance between the femur bone and the acetabulum (pelvis socket) to become very small due to the degradation of the articular cartilage and the overgrowth of the bone. For successful implant placement, a proper study for the positioning is essential to get the best results and to distribute the forces exerted by the body weight. To get this important information a statistical shape model needs to be calculated. In this work, we are interested in the phase that precedes the model creation where the standard approach is still manual segmentation.

The problem of image segmentation in this scenario is illustrated in (Figure 4.15) which shows one slice of a stack of CT-scanned images of the hip. The image shows the femoral head and the acetabulum, together with some surrounding tissue. We seek to process the whole volume image to visualize the femoral bone, and the image shows that the two bones appear to be connected.

Previous research has tackled this problem using manual segmentation as prerequisite such as; statistical shape methods to describe the femur bone (Schmid, Kim, & Magnenat-Thalmann, 2011) (Yokota, Okada, Takao, Sugano, Tada, & Sato, 2009), generalised Hough transform to construct the optimum model (Seim, Kainmueller, & Heller, 2008) and an iterative deformable model to match the femur shape (Pettersson, Knutsson, & Borga, 2006). Other methods relied on initial parameters chosen by an operator to refine boundary

information between the acetabulum and the femoral bone (Zoroofi, Sato, Sasama, Nishii, Sugano, Yonenobu, Yoshikawa, Ochi, & Tamura, 2003).

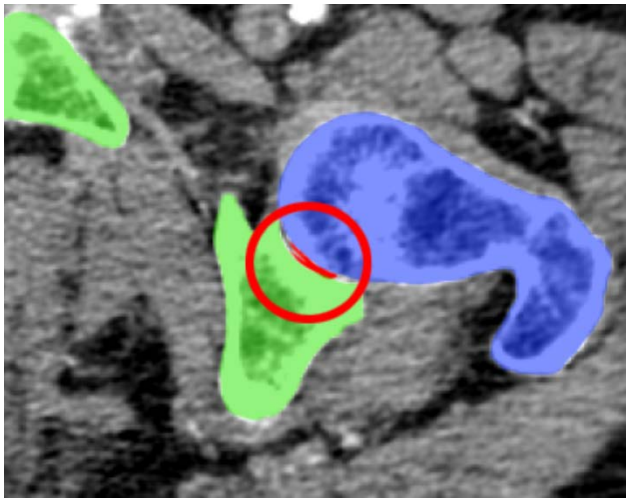

Figure 4.15 The intersection between the femoral head (blue) with the acetabulum (green) circled and labelled in (red).

There are two automated approaches for bone segmentation in the literature, one is based on the Graphcut method using geometrical analysis, statistical analysis and morphology (Krcah, Szekely, & Blanc, 2011b) and the other one hinged on local adaptive thresholding conditioned on Bayesian rules (J. Zhang, Yan, Chui, & Ong, 2010).

In this chapter, we extend the pressure analogy introduced in section 4.1 (Alathari & Nixon, 2013) to include fully automatic segmentation of touching objects with similar density between them. Pressure is used as a volumetric analogy to provide an operator to analyse and refine features in volume data. Again, only the principles of pressure are used to motivate an image analysis operator: precise detail is not needed. Pressure domain data has been enhanced by a new mapping technique followed by morphological operations to expand the pressure mask effect. This is not possible using conventional morphological operations (Lohmann, 1994) (without the pressure analogy) since these are isotropic and lack capability to separate gaps whilst retaining overall shape. Logical operations are applied to the pressure mask to separate the femur bone from the acetabulum. Labelling has been aided by using statistical operations. The proposed method is intuitive, anisotropic, non-

iterative and requires no previous knowledge and can fully automatically separate connected structures of similar density in CT images.

4.2.1 Methodology

Extracting the femur bone presents a great challenge for segmentation methods due to the existence of similar density bones surrounding and touching its surface. The pressure analogy presents a new perspective into the problem of separating connected objects in volumetric images. Unlike the previous work, which depends on the small gradient between objects, this method addresses the separation of objects, which have a similar density and which appear to be touching in that the space between them is often small and occasionally zero. The same basis as the original pressure approach (Alathari & Nixon, 2013) was adopted, one-sided threshold followed by a convolving cube to calculate the volume of the background to obtain the pressure domain. The pressure domain provides valuable information about connected areas between the objects.

$$\mathbf{P}_{x,y,z} = 1/\sum_{x,y,z\in\mathbf{W}} \mathbf{V}_{x,y,z} \quad \forall \mathbf{V}_{x,y,z} \in background \tag{4.5}$$

Where $\mathbf{W}$ is a window of size *5×5×5*, $\mathbf{V}$ is the volume that is thresholded so as to remove background data, retaining the high-density values, and $\mathbf{P}$ is the pressure domain. The pressure data is then mapped using a high pass filter response to retain consistency and to provide a smooth transform, mainly to provide better visualization. The filter is derived by arranging the pressure levels p_f in ascending order and deriving a mapping function extracted from a high-pass filter:

$$\boldsymbol{V_o} = v_i \frac{Z_R}{Z_R + Z_C} \tag{4.6}$$

where $v_i = 180$, $Z_C = -j(1/2\pi p_f C)$, $Z_R = 1500$ and $C = 1.06 \times 10^{-6}$ with a cut-off frequency $p_{f\ cut\ off} = 100$, for $p_f \in [1,125]$, so the high pressure values in the top 25 levels are retained and emphasized. This mapping function is used to derive $\mathbf{P}' = \mathbf{P}(\boldsymbol{V_o})$ which is then thresholded.

$$\mathbf{M}_{x,y,z} = \begin{cases} 1 & \text{if } \mathbf{P'}_{x,y,z} \geq \text{threshold} \\ 0 & \text{otherwise} \end{cases} \quad 4.7$$

After that, a connectivity check was applied on the thresholded mask; each element labelled defines a structured element $\mathbf{M}_i$ stored in 4D matrix $\mathbf{M}_{\text{L}}$. Each element is dilated $\oplus$ three times to increase its mass and close the gap between elements using structure **S** of size *3×3×3* with all voxels turned on.

$$\mathbf{M'}_i = \mathbf{M}_i \oplus \mathbf{S} \quad 4.8$$

$$\forall\ i\ \in 1{:}\ size\ \mathbf{M}_L\ in\ the\ 4th\ dimension$$

The next step is to erode $\ominus$ the whole mask in an attempt to minimize its effect.

$$\mathbf{M}_{sum} = logical\left(\sum_{i=1}^{\#elements} \mathbf{M'}_i\right) \quad 4.9$$

$$\mathbf{M}_{final} = \mathbf{M}_{sum} \ominus \mathbf{S} \quad 4.10$$

The final mask M_{final} is then inverted and applied to the thresholded volume V, separating the objects.

$$\mathbf{S}_{x,y,z} = \neg\, \mathbf{M}_{final\ x,y,z} \times \mathbf{V}_{\text{x,y,z}} \quad 4.11$$

The objects were labelled individually to describe each object uniquely. The mask discards a small amount of data, which is implicit in these operations. To recover this data, the mask was multiplied by a logical thresholded volume to obtain only the areas in the mask (used to separate objects), which do not exist in the background.

$$\mathbf{R}_{x,y,z} = \mathbf{M}_{final\ x,y,z} \times logical(\mathbf{V}_{\mathrm{x,y,z}}) \quad 4.12$$

Skeletonization (Lam, Lee, & Suen, 1992) was applied per slice on the recovered volume $\mathbf{R}$ to create the equivalent of a small creek or fissure between the mask segments to aid the reconstruction process. The labelled mask is then grown on those areas using the statistical mode. Each object in the volume $\mathbf{F}$ can now be labelled uniquely with no lost data.

$$\mathbf{F}_{x,y,z} = Mode\left(\mathbf{S}_{\boldsymbol{x,y,z}\in \boldsymbol{W}}\right) \quad \forall \boldsymbol{R_{x,y,z}} \in \text{foreground} \quad 4.13$$

Three morphological closing operations have been applied to every labelled object and close any open gaps in the detected object.

$$\mathbf{B}_{final,i} = \mathbf{F}_i \bullet \mathbf{S} \qquad \forall\, i \in 1\text{: Number of labels} \quad 4.14$$

where B_{final} is a 4D matrix which contains the volume of each segmented object. An illustration showing the whole process is shown in Figure 4.16.

Step 1 – Use pressure analogy to find the trace of the cartilage	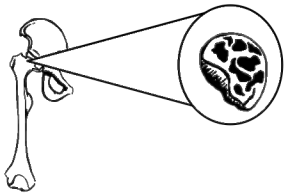	Degradation caused by Osteoarthritis highlighted using pressure analogy $\mathbf{P}_{x,y,z} = 1/\sum_{x,y,z \in \mathbf{W}} \mathbf{V}_{x,y,z} \quad \forall \mathbf{V}_{x,y,z} \in$ background
Step 2– Re-map the pressure domain to have better consistency	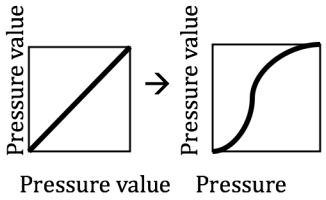	$\boldsymbol{V_o} = v_i \frac{Z_R}{Z_R + Z_C}$ $v_i = 180,\ Z_C = -j(1/2\pi p_f C),\ Z_R = 1500$ and $C = 1.06 \times 10^{-6}$ with a cut-off frequency $p_{f\ cut\ off} = 100$, for $p_f \in [1,125]$
Step 3 – Threshold the remapped pressure domain		$\mathbf{M}_{x,y,z} = \begin{cases} 1 & \text{if } \mathbf{P'}_{x,y,z} \geq \text{threshold} \\ 0 & \text{otherwise} \end{cases}$
Step 4 – Label and dilate each element extracted and store the results in 4D matrix	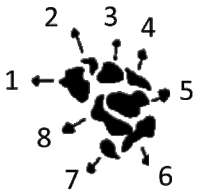	$\mathbf{M'}_i = \mathbf{M}_i \oplus \mathbf{S}$ $\forall\ i \in 1: size\ \mathbf{M}_L\ in\ the\ 4th\ dimension$
Step 5 – Combine the elements and erode them		$\mathbf{M}_{sum} = logical\left(\sum_{i=1}^{\#elements} \mathbf{M'}_i\right)$ $\mathbf{M}_{final} = \mathbf{M}_{sum} \ominus \mathbf{S}$
Step 6 – Use the eroded mask to separate the connected objects and identify each with a label	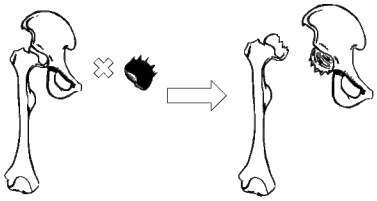	$\mathbf{S}_{x,y,z} = \neg\, \mathbf{M}_{final\ x,y,z} \times \mathbf{V}_{x,y,z}$
Step 7 – Grow the resulted labeled objects on the original thresholded volume	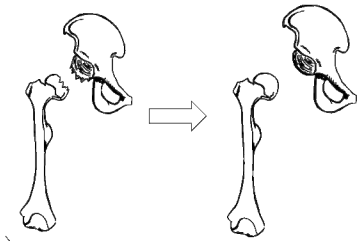	$\mathbf{R}_{x,y,z} = \mathbf{M}_{final\ x,y,z} \times logical(\mathbf{V}_{x,y,z})$ $\mathbf{F}_{x,y,z} = Mode(\mathbf{S}_{x,y,z \in W}) \quad \forall \boldsymbol{R}_{x,y,z} \in$ foreground $\mathbf{B}_{final,i} = \mathbf{F}_i \bullet \mathbf{S} \qquad \forall\ i \in 1:$ Number of labels

Figure 4.16 An illustrations showing the pressure enhancement methodology of Section 4.2

To analyse the validity of the results, the surface area was calculated for the proposed method results a_p and the manually segmented data a_m. The manual segmentation took place by thresholding then removing surrounding bones and soft tissue. The Dice similarity coefficient (dc) (Sørensen, 1948), which is used to measure the union of two sets to the average sample size. It was used to compare the results of segmentation by (Grau, Mewes, Alcañiz, Kikinis, & Warfield, 2004; Ben Younes, Nakajima, & Saito, 2014).

$$dc = 2a_p/(a_p + a_m) \tag{11}$$

Our work describes a solution that is based on the original basis of the pressure analogy. Virtually the same advantages have been accrued as in the literature; a non-iterative, anisotropic method that depends on local features of the objects in the scene. The novel step is the high-level refinement and the extension towards separating connected objects of similar density.

4.2.2 Results

As discussed previously, the method provides a mask that is used to separate the connected objects. In this section, we evaluate the performance of the proposed method on 51 volumetric cropped images of femur bone acquired using CT scanner. The images were cropped to concentrate the feature extraction process. To illustrate the problem, several slices of the connected areas between the acetabulum and the femoral head of one volume are shown Figure 4.12. In these images, the connections appear in different places, so the technique requires information from local features. Another problem also arises, in that the multiple contact areas between the veins in the surrounding soft tissue touching the femur, especially when a contrast agent is present. However, veins have little impact on the total surface area Figure 4.13.

(a) (b)

Figure 4.17 A render of the final segmented image of femur bone shown in Figure 4.12 and Figure 4.13 (a) Render showing the largest 6 objects, (b) The largest object labelled hence the femur bone. See Appendix B for the full set of segmented data.

A rendering of the final labelled objects, with each label identified by a unique colour, is shown Figure 4.17a Once the femur bone is labelled and identified, it can be extracted by choosing the desired label as in Figure 4.17b Successive slices through the segmented data are shown in Figure 4.18.These show that the acetabulum is correctly identified as separate from the femur even when they are in contact and that the perimeters of the bones (the surfaces) are extracted correctly.

The proposed method has been applied to the 51 femur volumes; a small sample of the results is shown in Figure 4.19. The segmentation proved to be successful and the femur bone was extracted properly. Nevertheless, some of the results showed less than perfect segmentation as in Figure 4.20. In some cases, some segments of the femur head were joined with the hip, in other cases the whole head of the femur bone is lost and the worst was the difficulty of separating the hip and the femur bone. Table 4.1 shows the performance of the proposed method on the 51 femur bones, the effect of veins have been omitted due to their minor contribution to the total surface of the segmented femur bone. This shows that a clear majority of the femurs (64.7%) have been successfully extracted, that many of the remainders have small segments missing (23.52%), some case the mask acted on the femoral neck rather than the femoral head which result in a femur with missing head (9.8%), and that only one is extracted with connections remaining (1.9%).

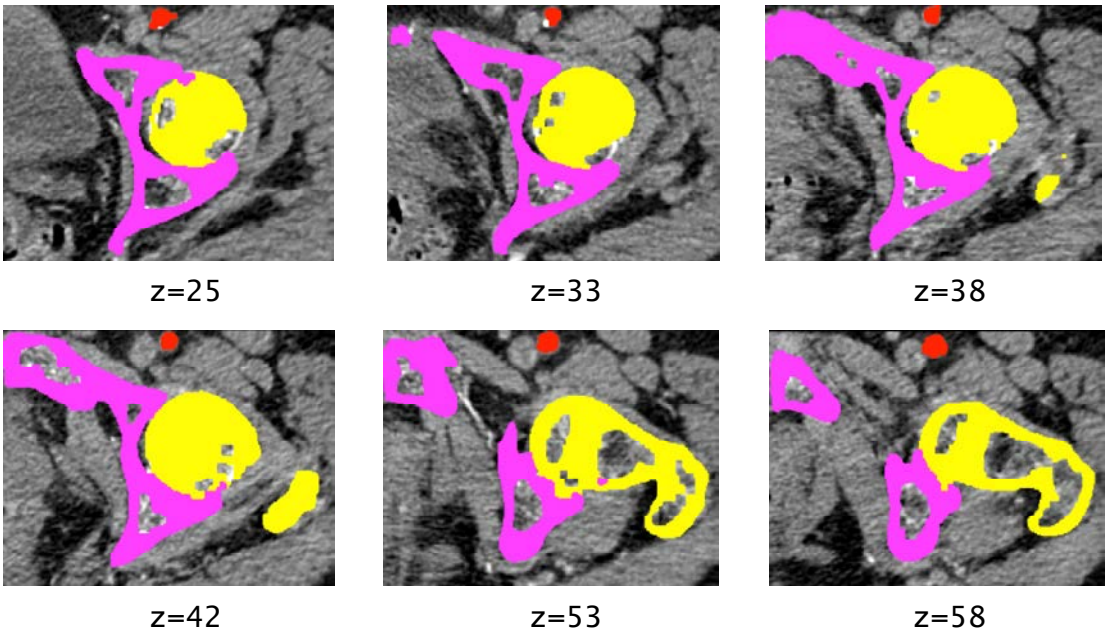

Figure 4.18 Different slices though the hip showing the contact area between the femoral head and the acetabulum

Figure 4.19 Sample of four segmented femur bones using the proposed method. See Appendix B for the full set of segmented data.

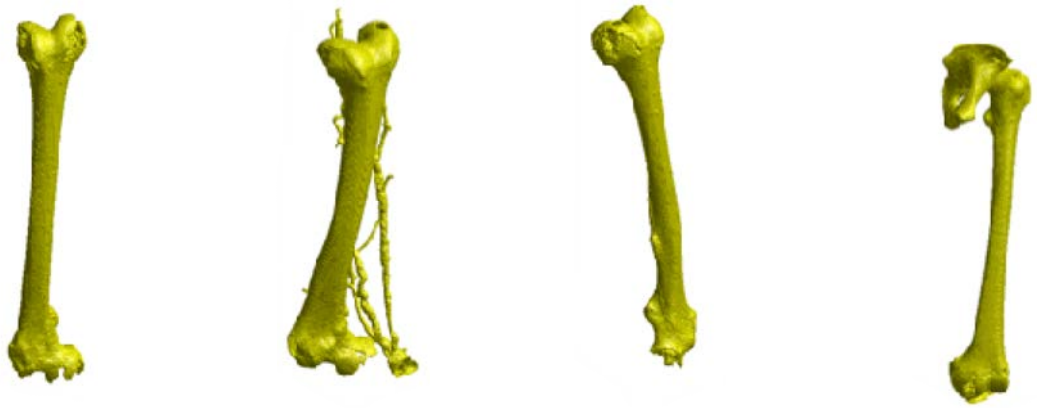

(a) (b) (c) (d)

Figure 4.20 Example of several situations where the proposed method did not perform well, (a) and (b) Some segments missing from the femoral head, (c) Femoral head completely lost, (d) Complete failure to separate the femur bone from the hip. See Appendix B for the full set of segmented data.

Notes on segmented data	Percentage of the data processed with proposed pressure analogy
Femur bones Fully segmented	64.7%
Femur bones with missing Femoral head	9.8%
Femur bones with missing bits from Femoral head	23.52%
Femur bones connected to pelvis	1.9%

Table 4.1 The performance of the proposed method based on visual inspection of segmented femur.

Due to the absence of the source code for the state of the art methods such as (Krcah et al., 2011b) and (J. Zhang et al., 2010) a fair comparison would be difficult especially with the variety of parameter choices that is necessary for correct operation. The Dice coefficient of each sample of 9 volumetric images has been calculated. To verify the amount of loss in the total surface area in the results, the manual segmentation was used as the ground truth (Figure 4.21). An average of dc = 0.907 has been calculated which indicate a minor loss in the total surface area and a successful segmentation.

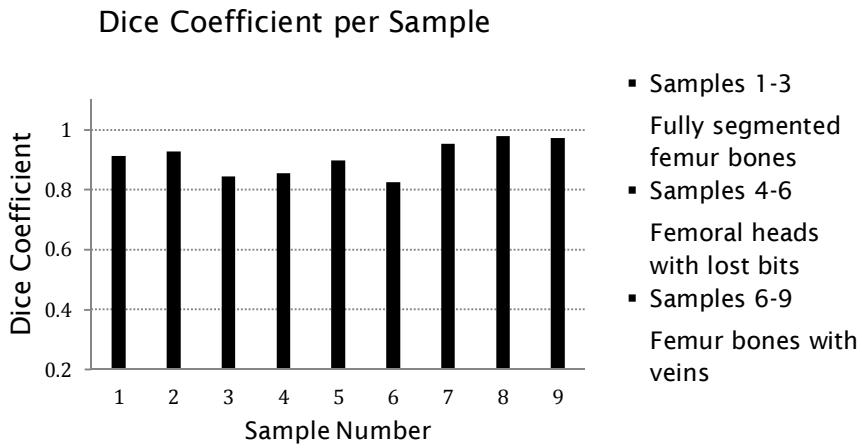

Figure 4.21 Dice coefficient for a sample of the results based on the total surface area compared to the surface area of the manually segmented data to determine the similarity between the two.

It is also worth noting that the Dice coefficients of the femur bone extracted together with veins and arteries have introduced false-positive information. This arises from the larger surface area of the combination of bone with blood vessels and could lead the Dice coefficient to exceed unity, which has not occurred here (some segments have been omitted, but cannot be observed in these renderings).

As anticipated, the proposed method showed promising results in segmenting and visualizing other bones such as the tibia and fibula bones in Figure 4.22 where the only variable changed is the threshold used for the pressure (Eqn. 4.7). Figure 4.23 shows images of the complete pelvis, Figure 4.23a, includes some blood vessels, two femoral heads and the lower lumbar region. Figure 4.23b shows the labelled pelvis extracted alone from this data. Again, the only variable changed is the pressure threshold and the remainder of the technique is fully automatic.

(a) (b) (c) (d)

Figure 4.22 Other bones segmented using the proposed method, (a) and (c) Rendering of segmented tibia bone, (b) and (d) Rendering of segmented fibula bone.

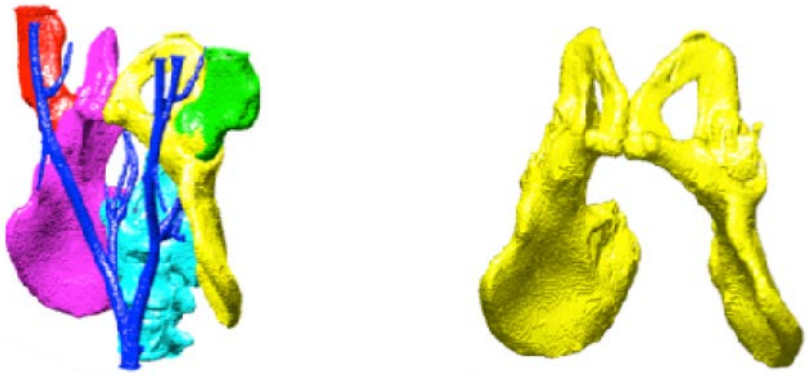

(a) (b)

Figure 4.23 Other bones segmented using the proposed method (a) Rendering of the hip area including some blood vessels, two femoral heads and the lower lumbar region, (b) Rendering of the final segmented pelvis.

4.2.3 Discussion

Segmenting and visualizing the femur bone is the first step for future preclinical analysis in arthritis. The literature flourishes with machine learning techniques that depend on manually segmented data. The problem with those techniques is the general problem of machine learning, they are data oriented.

Morphology operations alone would introduce or neglect some of the valuable information by acting in an isotropic manner, which would result in undesirable results. On the other hand, the new pressure analogy depends on local image features; it is anisotropic, non-iterative. The technique could even provide a mask without the need for training or learning. The proposed method based on the pressure analogy and carries the same advantages; it can also handle similar density connection between the objects. This would benefit the automation of the other techniques discussed in literature such as providing an automatic large set of data for machine learning and presenting the general Hough transform with a standard template. The results can also be of great help to the preclinical studies of hip replacement, and help determining the optimum positioning of the femur bone implant to achieve a perfect fit. The proposed method has shown encouraging results for separating touching objects with the same density in computer tomography volumes.

Analysis on the resulted femur bone have been divided into three main categories; fully segmented femur bones, segmented bones with missing bits and segmented bone with veins attached. The categorization is based on the visual inspection of the data manually. The reason behind this classification is to study the effect of every shortcoming in the results caused by the segmentation artefact. The analysis were based on six criteria; femur length, femoral bone neck length defined by the distance from head-centre to neck-axis intersection, femoral shaft area which is the area of the diaphysis at 2cm below lesser trochanter, the femoral head radius and the two radiuses of the shaft at 2cm below lesser trochanter. The results are compared side by side with manual segmentation provided by an expert which is considered by literature as the “gold standard” (Kaus, Warfield, Nabavi, Chatzidakis, Black, Jolesz, & Kikinis, 1999; Babalola, Patenaude, Aljabar, Schnabel, Kennedy, Crum, Smith, Cootes, Jenkinson, & Rueckert, 2008).

The fully segmented results showed a very close relationship with the manually segmented data Figure 4.24. The consistency can be seen in all areas of investigation (Table 4.2), which indicate a proper overall segmentation for the femur bone based on the mean value comparison between the results of the proposed method and the manually segmented data. The standard deviation

indicates how each sample vary from the mean, due to the individuality and the variety of the samples (different ages and genders), the error would indicate the percentage difference between the samples in each group of results. The overall errors were in acceptable range.

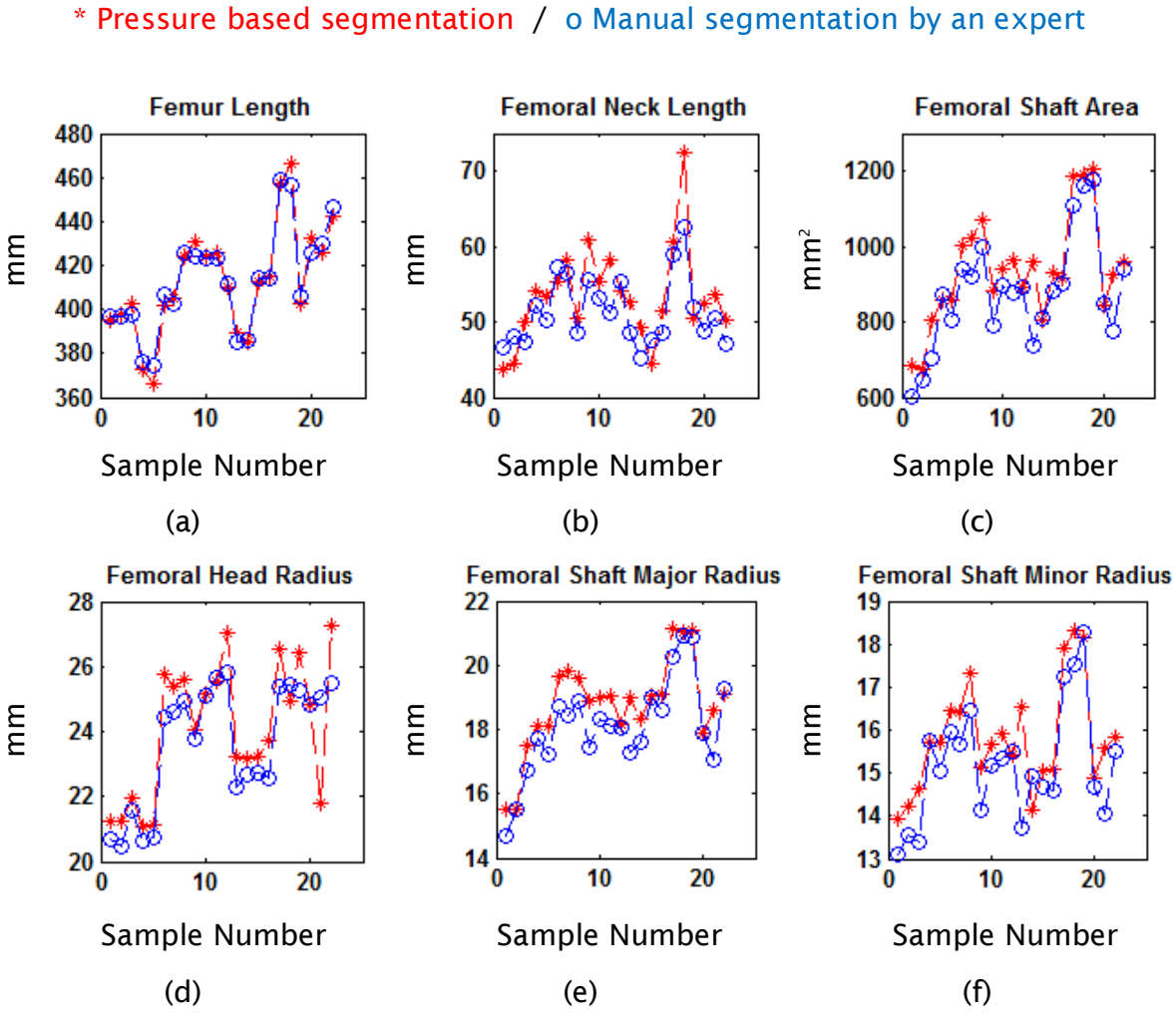

Figure 4.24 Analysis on the fully segmented data (a) femur length, (b) femoral bone neck length defined by the distance from head-centre to neck-axis intersection, (c) femoral shaft area which is the area of the diaphysis at 2cm below lesser trochanter, (d) the femoral head radii and the two radii of the shaft at 2cm below lesser trochanter, (e) the major and (f) the minor.

On the other hand, the data classified as segmented femurs with missing bits showed less consistent results and that is due to the small amount of voxels available for fitting the femoral head sphere radius, which in its turn affect the neck calculations (Figure 4.25). Those bones also include some veins attached to the shaft and that is reflected in the femoral shaft area and its major and minor radiuses as seen in sample 1 and 4. The statistical analysis Table 4.3

showed an increase in the mean error hence the difference between the pressure segmented and the manually segmented data in the majority of areas of study. The small size of the data sample has also contributed in the increase in the standard deviation.

		Fully Segmented Samples		
		Pressure Analogy	Manual Segmentation	% error
Femoral Head Minor Radius	mean (mm)	15.78	15.17	4.01
	std (mm)	1.20	1.29	6.98
Femoral Neck Length	mean (mm)	53.92	51.95	3.79
	std (mm)	6.34	4.62	37.21
Femoral Shaft Area	mean $(mm)^2$	955.87	873.84	9.39
	std $(mm)^2$	169.28	140.91	20.14
Femoral Shaft Major Radius	mean (mm)	19.22	18.07	6.40
	std (mm)	2.60	1.44	80.30
Femur Length	mean (mm)	413.57	412.79	0.19
	std (mm)	24.22	22.34	8.42
Mean Femoral Head Radius	mean (mm)	23.70	23.85	0.63
	std (mm)	3.45	1.93	78.22

Table 4.2 Statistical analysis of the fully segmented samples in Figure 4.24

The shaft area and the shaft major radius suffered from a severe increase in the error that is also caused by the attached veins, which are translated in incorrect automatic measurements.

The segmented data with veins attached to it (Figure 4.26), showed even less consistent results. The veins would contribute in all of the analysis, which in turn provided inaccurate analysis. To study how strong the effect of the veins, simple morphological opening has been applied to this data set followed by labelling the largest object as the femur. Five out of nine femurs have been separated using this technique as shown in (Figure 4.27). The improvements were significant in all areas except for one sample where the femoral head has been affected by the morphological operation and bits has been lost and the femoral head could not be reconstructed. The statistical comparison between the two samples of connected vein and removed veins are shows in (Table 4.4) and (Table 4.5) respectively, an improvement in the mean error is demonstrated in all areas of study. The deviation in the sample has also seen an improvement in most areas.

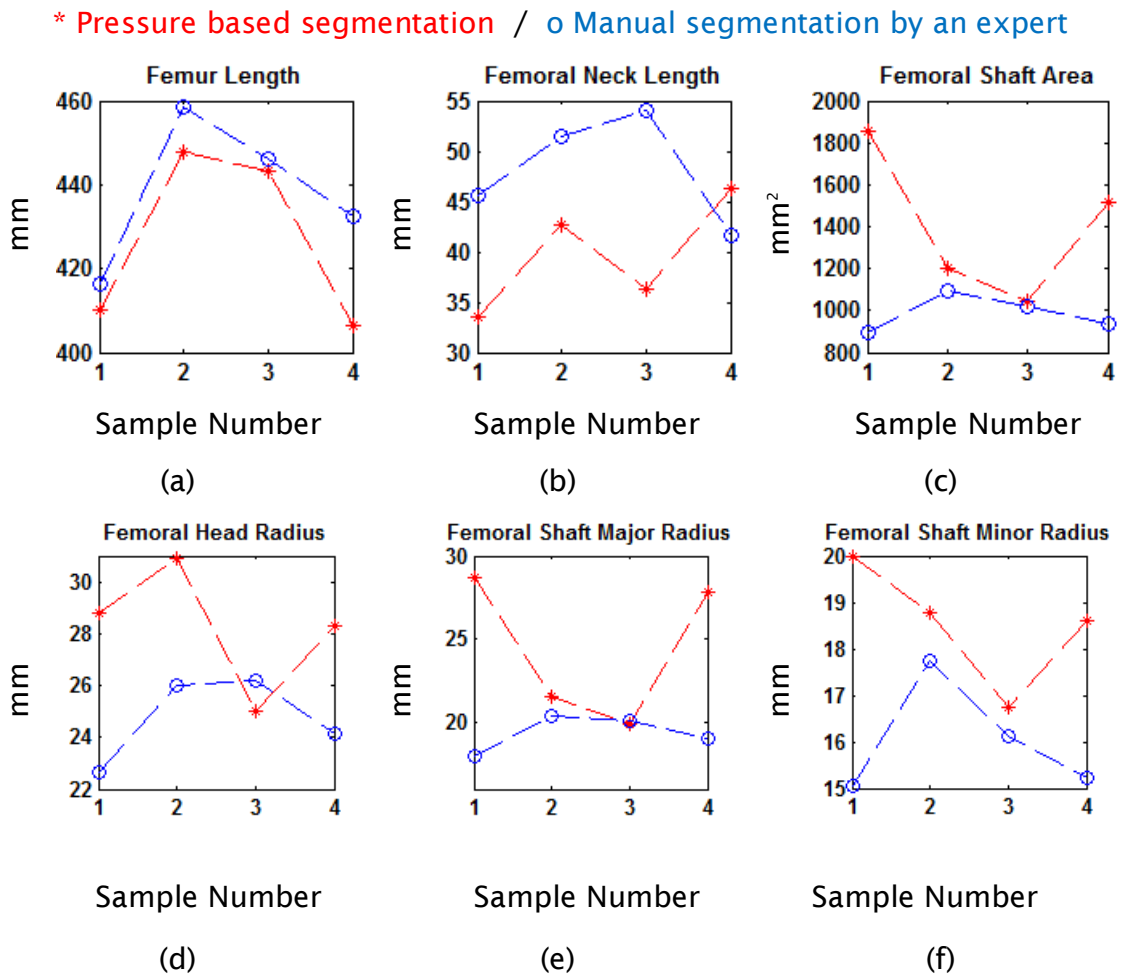

Figure 4.25 Analysis on femur bones segmented with missing bits (a) femur length, (b) femoral bone neck length defined by the distance from head-centre to neck-axis intersection, (c) femoral shaft area which is the area of the diaphysis at 2cm below lesser trochanter, (d) the femoral head radius and the two radii of the shaft at 2cm below lesser trochanter, (e) the major and (f) the minor.

		Femur Bones Segmented with Missing Bits		
		Pressure Analogy	Manual Segmentation	% error
Femoral Head Minor Radius	mean (mm)	18.53	16.03	15.57
	std (mm)	1.33	1.23	8.51
Femoral Neck Length	mean (mm)	39.68	48.16	17.62
	std (mm)	5.84	5.66	3.19
Femoral Shaft Area	mean $(mm)^2$	1403.97	985.16	42.51
	std $(mm)^2$	359.73	86.27	316.97
Femoral Shaft Major Radius	mean (mm)	24.49	19.37	26.42
	std (mm)	4.40	1.09	305.08
Femur Length	mean (mm)	426.85	438.41	2.64
	std (mm)	21.79	18.16	19.99
Mean Femoral Head Radius	mean (mm)	28.25	24.75	14.15
	std (mm)	2.43	1.67	46.03

Table 4.3 Statistical analysis of the femur bones segmented with missing bits samples in Figure 4.25

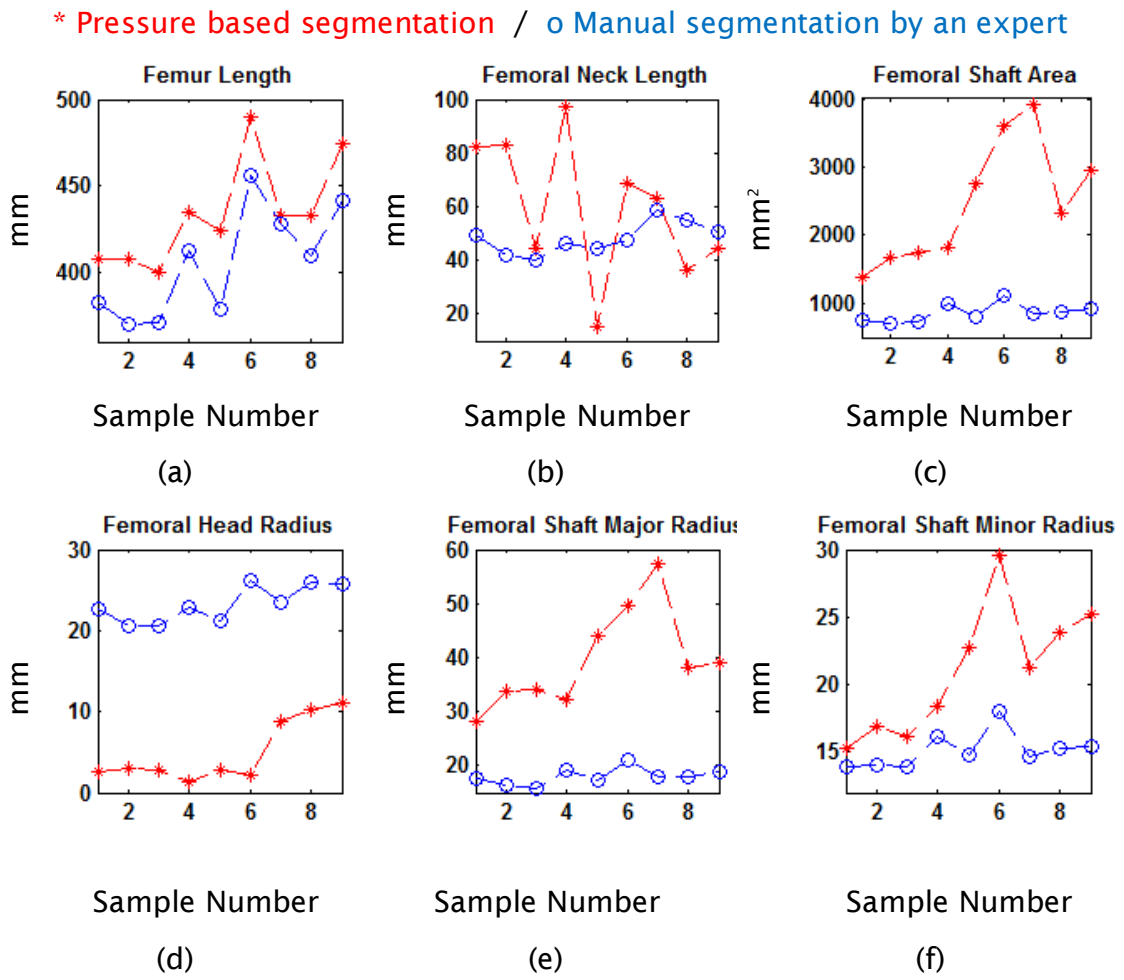

Figure 4.26 Analysis on femur bones segmented with vein (a) femur length, (b) femoral bone neck length defined by the distance from head-centre to neck-axis intersection, (c) femoral shaft area which is the area of the diaphysis at 2cm below lesser trochanter, (d) the femoral head radius and the two radii of the shaft at 2cm below lesser trochanter, (e) the major and (f) the minor.

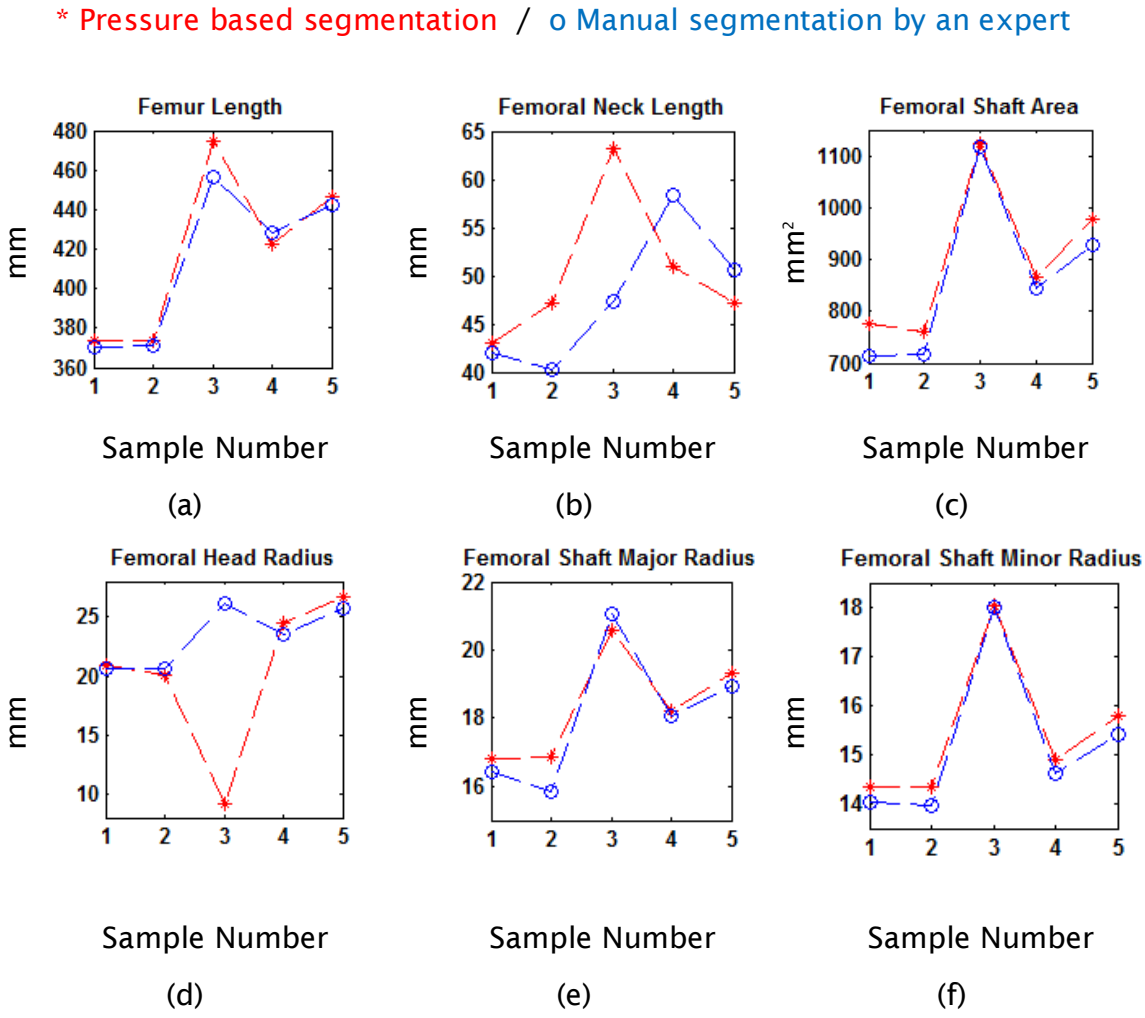

Figure 4.27 Analysis on femur bones segmented in Figure 4.26 after successful veins removal using morphology (a) femur length, (b) femoral bone neck length defined by the distance from head-centre to neck-axis intersection, (c) femoral shaft area which is the area of the diaphysis at 2cm below lesser trochanter, (d) the femoral head radius and the two radii of the shaft at 2cm below lesser trochanter, (e) the major and (f) the minor.

		Femur Bones Segmented with Vein		
		Pressure Analogy	Manual Segmentation	% error
Femoral Head Minor Radius	mean (mm)	21.53	14.94	44.09
	std (mm)	4.62	1.26	268.19
Femoral Neck Length	mean (mm)	62.16	48.26	28.81
	std (mm)	24.84	5.30	368.92
Femoral Shaft Area	mean $(mm)^2$	2593.40	839.66	208.86
	std $(mm)^2$	861.63	130.12	562.20
Femoral Shaft Major Radius	mean (mm)	41.12	17.82	130.79
	std (mm)	9.02	1.45	520.21
Femur Length	mean (mm)	429.06	402.69	6.55
	std (mm)	29.31	29.47	0.54
Mean Femoral Head Radius	mean (mm)	5.04	23.09	78.17
	std (mm)	3.72	2.07	80.20

Table 4.4 Statistical analysis of the femur bones segmented with missing bits samples in Figure 4.26

		Femur Bones Segmented with Vein Removed		
		Pressure Analogy	Manual Segmentation	% error
Femoral Head Minor Radius	mean (mm)	15.24	15.04	1.34
	std (mm)	1.51	1.56	3.25
Femoral Neck Length	mean (mm)	50.74	47.86	6.00
	std (mm)	7.00	6.52	7.25
Femoral Shaft Area	mean $(mm)^2$	877.62	844.45	3.93
	std $(mm)^2$	147.26	158.46	7.07
Femoral Shaft Major Radius	mean (mm)	18.23	17.87	2.04
	std (mm)	1.48	1.92	23.09
Femur Length	mean (mm)	416.24	410.60	1.37
	std (mm)	40.09	36.79	8.98
Mean Femoral Head Radius	mean (mm)	19.99	23.10	13.47
	std (mm)	6.07	2.45	147.56

Table 4.5 Statistical analysis of the femur bones segmented with missing bits samples in Figure 4.27

Figure 4.28 Several Samples of the segmented coins show effectiveness of the pressure enhancement.

The proposed method by (Krcah et al., 2011b) provides a good solution for automating the process of graph cut through providing a automatic seeds and sources using morphology. The only drawback of their proposed method is that it would detect a single object in the volumetric image and would face a great challenge dealing with volume similar to the one in Figure 1.1 where the object might be removed by morphology operations. Using the same method described in this section and by combining the pressure from the surface information with the pressure from the thresholded volume to increase the probability of the pressure point close to surface, the results show a much better segmentation (Figure 4.28) compared to the original pressure (Figure 4.7) described in the section 4.1 in terms of the number and quality of

segmented objects. Segmented coin of (Figure 4.29) is used to illustrate the quality difference between the coin segmented using enhanced pressure analogy and the same coin using simple pressure analogy. The enhanced pressure provided more detail on the coin face, thicker volume and sharper edges noting that the coin in Figure 4.29a appears to show the head of the person and some letters which cannot be seen and only inferred from the surface in Figure 4.29b.

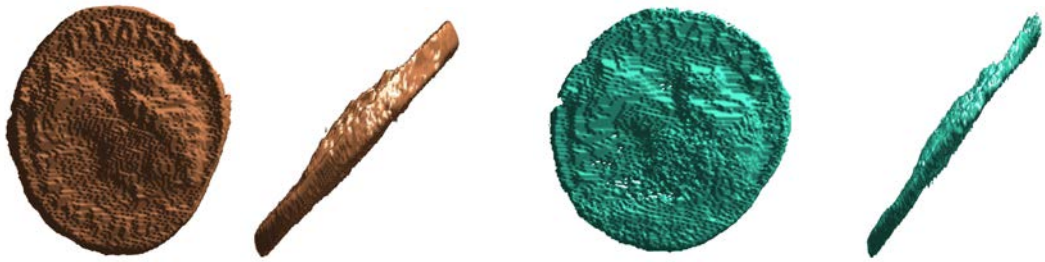

(a) (b)

Figure 4.29 Single coin from the set of (Figure 1.1) segmented using (a) Enhanced pressure, and (b) Simple pressure.

A single slice of Watershed segmentation and the simple pressure are compared to the same slice resulted from the enhanced pressure in (Figure 4.30). The enhanced pressure provided full detection of the object and less eroded surface than the simple pressure. Also compare to the Watershed segmentation far much better identification of the object of interest.

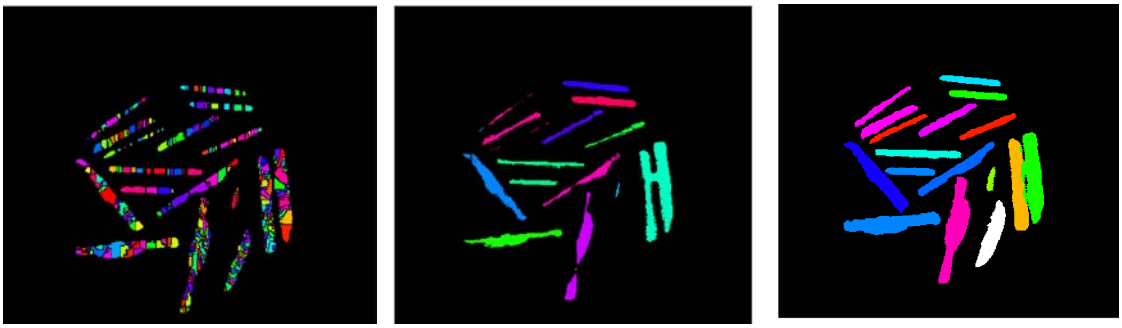

(a) (b) (c)

Figure 4.30 Single slice of the final segmented volume of the coins in (Figure 1.1) using (a) Watershed, (b) Simple pressure analogy, and (c) Enhanced pressure.

4.3 Conclusion

The concept of using physical analogy (Mark S Nixon et al., 2009) has been available for years now; introducing new concept based on scientifically approved parameterizations. Several analogies have been introduced in literature; force field (Hurley, Nixon, & Carter, 2002) ,water flow (Liu & Nixon, 2006) and heat flow (Direko & Nixon, 2006), which have introduced new perspective into image segmentation area. In this chapter pressure is used as a volumetric analogy to provide an operator to analyse and refine features in volume data. The main goal of the current chapter was to provide three dimensional segmentation method that is automatic, not iterative, connectivity based or model based. The findings have shown that such method is possible and depends on the understanding of the volumetric image nature and by applying the physical analogy in a virtual environment. The results indicate that the segmentation was successful except in some cases, which is expected to happen in any operator-based method. The method does not require any previous knowledge, which makes is applicable for small data sets. Despite the adventurous and exploratory nature of this method it shows that a physical analogy can provide results comparable with manual segmentation. An arguable weakness of the presented method is inherent from its main strength, which is the fact that it depends on the local features of the image. However, direct application on patient CT data, which is a real life situation, showed very promising results with no issues with noise. Further work might be to explore the possibility of using other image local features.

Chapter 5: Conclusions and Future Work

5.1 Conclusions

The main goal of the current study was to develop a set of sequential model based methods to identify and segment objects in volumetric images. This study has shown that extending well-established methods in literature from 2D to 3D using the original basis should consider the increase in dimensionality. The current results highlight the importance of developing and expanding 2D operators before applying them into 3D space to make use of the extra information provided by the volumetric image. The current findings add to a growing body of literature on expanding what is already known into a higher dimension.

The second major finding was that objects could be identified from voxel information. The findings of this research provide insights for information hidden within the voxel data. The literature use evidence gathering with the assumption of having segmented surface rather than a set of voxel as intended in the original Hough transform. This work contributes to existing knowledge of evidence gathering by providing several methods based on the same original mind-set of Hough transform. This study was limited by the absence of image databases that can be used to further highlight the advantages of using voxel information.

The most obvious finding to emerge from this study is that studying the background rather than the objects themselves in thresholded image can aid in segmentation of the objects. The results of this research support the idea that physical analogy can help in solving image segmentation problems. This is the first time that pressure analogy has been used to segment objects in feature extraction. The study has gone some way towards enhancing our understanding of importance of the local feature in the volumetric image. The

scope of this study was limited to connected objects with the same high density. More research is required to further enhance the proposed method by including more local features in the study.

5.2 Future Work

Stacking the developed methods together would provide a new and one of the first methods to count objects in 3D volumetric images. The results would then be compared to other high level methods such as scale invariant feature transform (SIFT) and Speeded Up Robust Features (SURF). The comparison will be against the ability of detection of multiple simple geometrical shapes in one image. The search for other approaches will be continued along these lines in the literature as well as to refine techniques developed here.

Several aspects of future improvement can be considered for the proposed Hough transform (Chapter 3) such as the automation of threshold values used in the proposed evidence gathering methods and the use of an advanced edge detector that would take into account the high frequency noise surrounding the object of interest. Validation process to confirm the shape detection based on accumulator peaks reconstruction and other methods (in case of cylinder detection, line detection should be used to indicate axis detection). The local features and the geometric properties of the shape could also be used to develop a decomposed accumulator space to reduce the computational expense.

The use of edge information to enhance the pressure method (Chapter 4) proved to be a valuable guide through providing areas with higher priority in case of pressure point existence within the shape of interest. Further investigation will be considered on the ability of highlighted surface points to limit the erosion naturally inherited by the pressure analogy hence a better shape extraction.

The main motivation behind the pressure analogy is to provide a step to replace the manual segmentation to provide presentable data and to create a database, which seems to be the current interest of research to ravel the 2D imaging systems. The segmented data can be used to provide sets of criteria

to rapidly train machine intelligence algorithms with data extracted automatically.

Further future study will compare the statistical shape model will be created using the results of the proposed pressure analogy, after being registered and combined using principal component analysis, to a statistical shape model created using manual segmentation. Dice similarity coefficient will be used to compare the surface area of the two models and several cross sectional areas will be compared the specifics of the two models. Later on, the parameters of the presented line, cylinder and sphere detections can be used to guide the calculated statistical shape model into the correct position and direction to properly segment the femur bone.

Appendices

Appendix A

The full set of reconstructed lines of Figure 3.22 from the accumulator $\boldsymbol{A}$ of chapter 3 at every line magnitude $\boldsymbol{L_i}$ and the angle pair $(\boldsymbol{\theta}, \boldsymbol{\varphi})$ associated with it.

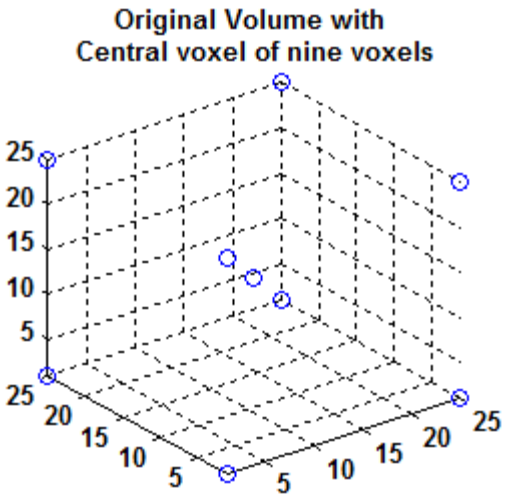

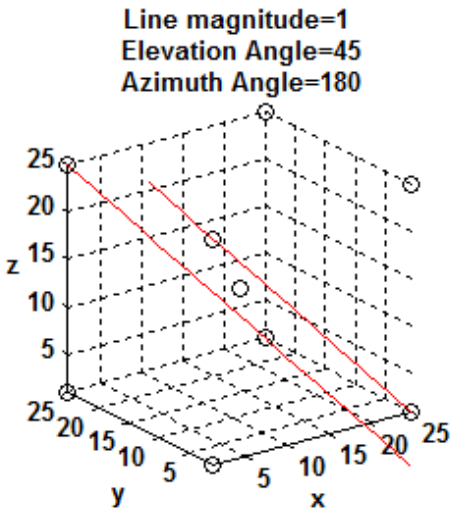

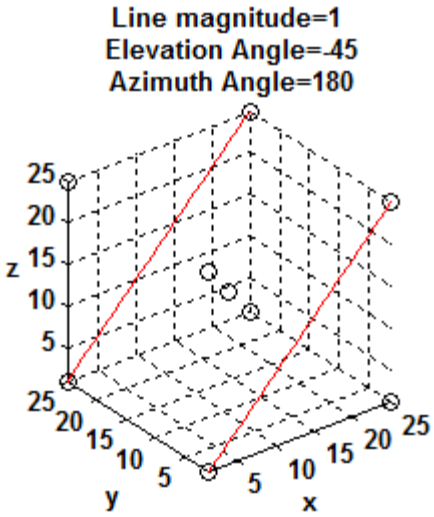

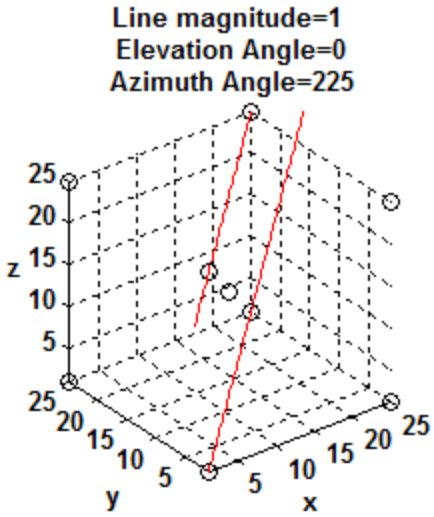

Line magnitude=1
Elevation Angle=35
Azimuth Angle=225

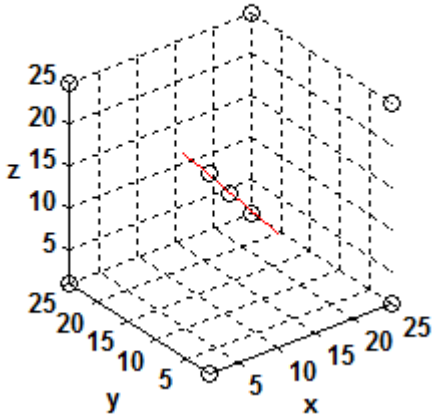

Line magnitude=2
Elevation Angle=35
Azimuth Angle=225

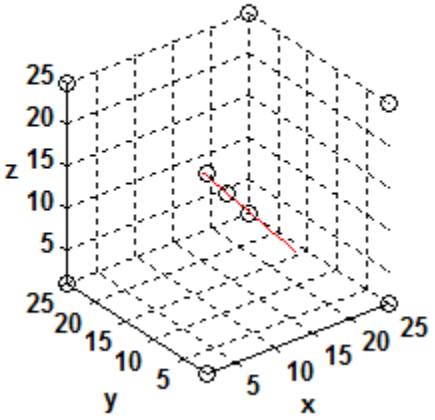

Line magnitude=1
Elevation Angle=-35
Azimuth Angle=225

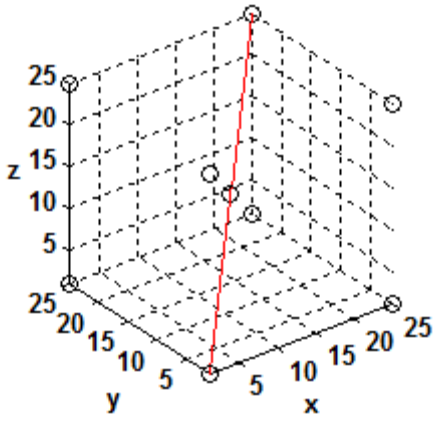

Line magnitude=2
Elevation Angle=-35
Azimuth Angle=225

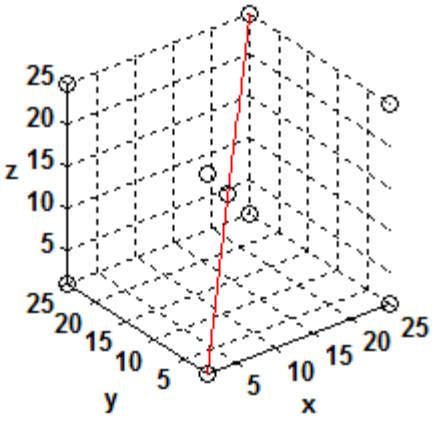

Line magnitude=1
Elevation Angle=0
Azimuth Angle=270

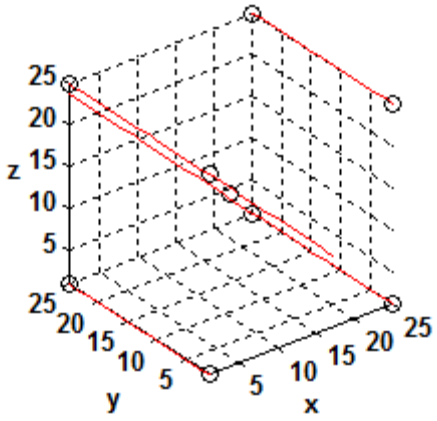

Line magnitude=1
Elevation Angle=45
Azimuth Angle=270

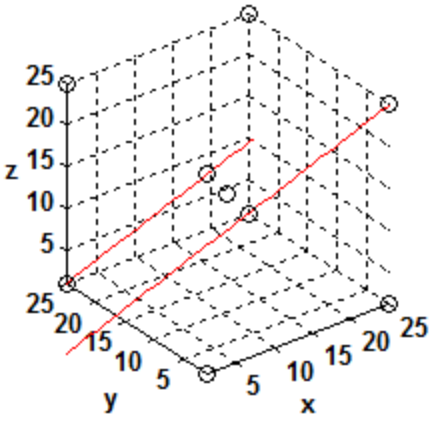

Line magnitude=1
Elevation Angle=-45
Azimuth Angle=270

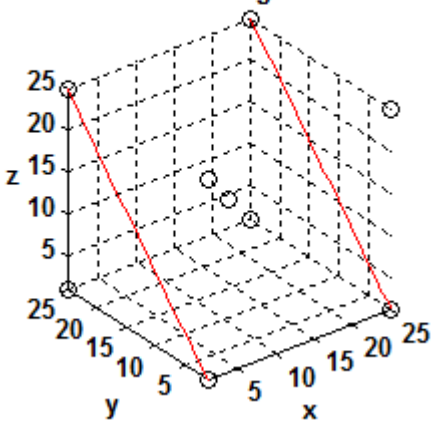

Line magnitude=1
Elevation Angle=0
Azimuth Angle=315

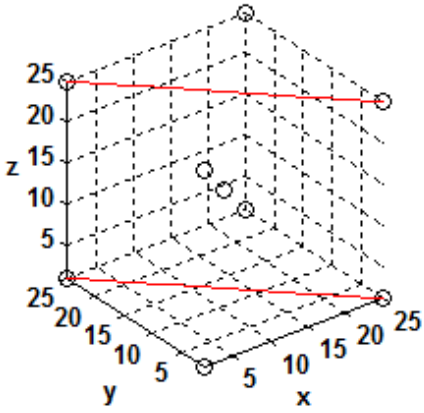

Line magnitude=1
Elevation Angle=35
Azimuth Angle=315

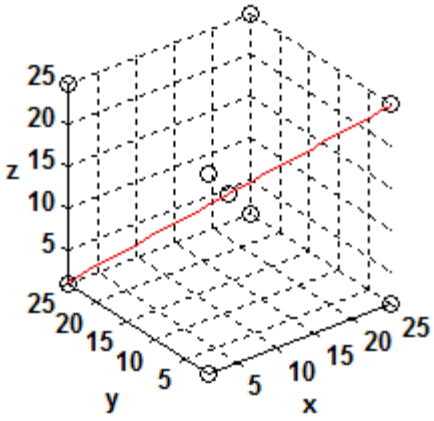

Line magnitude=2
Elevation Angle=35
Azimuth Angle=315

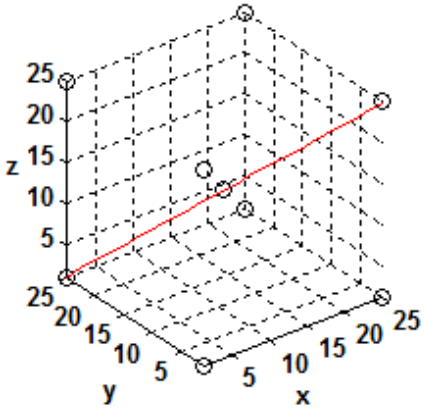

Line magnitude=1
Elevation Angle=-35
Azimuth Angle=315

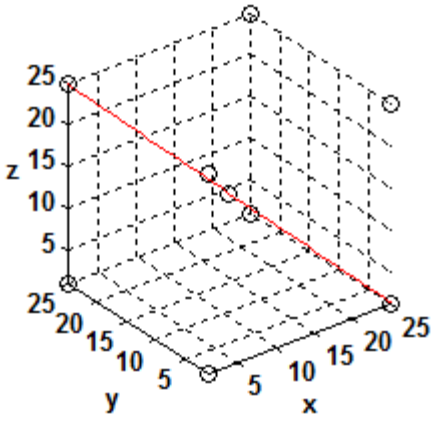

Line magnitude=2
Elevation Angle=-35
Azimuth Angle=315

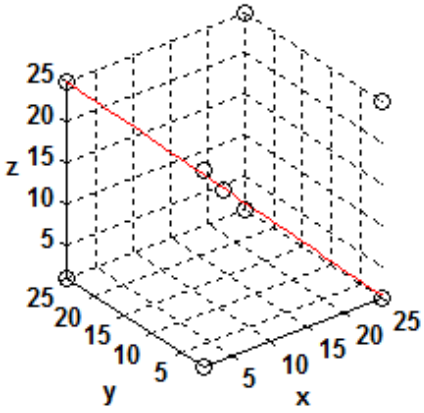

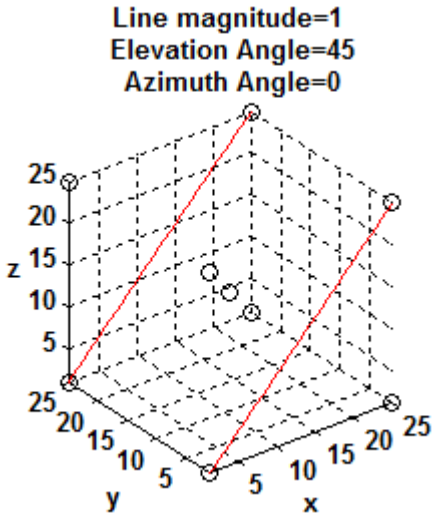
Line magnitude=1
Elevation Angle=45
Azimuth Angle=0
z
y
x

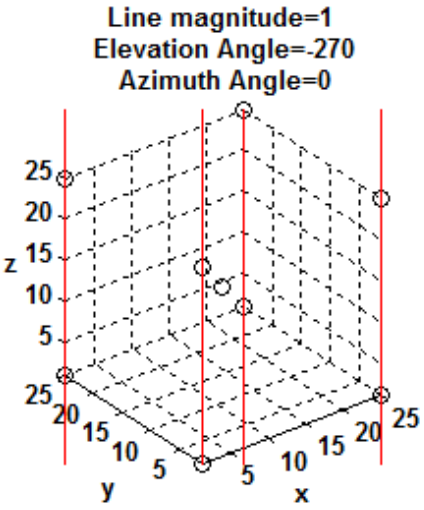
Line magnitude=1
Elevation Angle=-270
Azimuth Angle=0
z
y
x

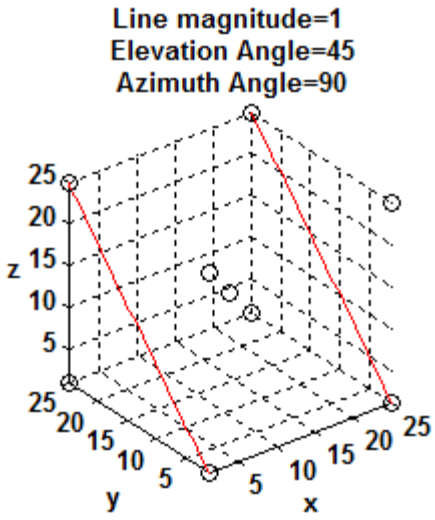
Line magnitude=1
Elevation Angle=45
Azimuth Angle=90
z
y
x

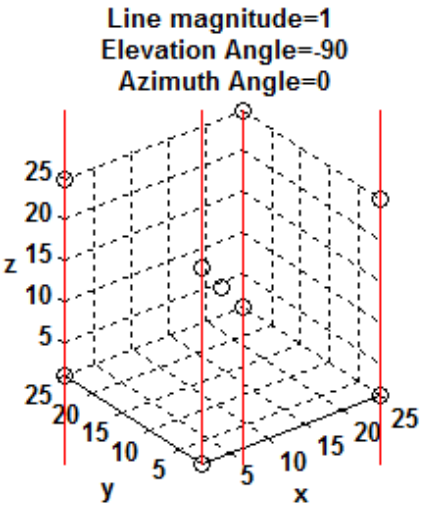
Line magnitude=1
Elevation Angle=-90
Azimuth Angle=0
z
y
x

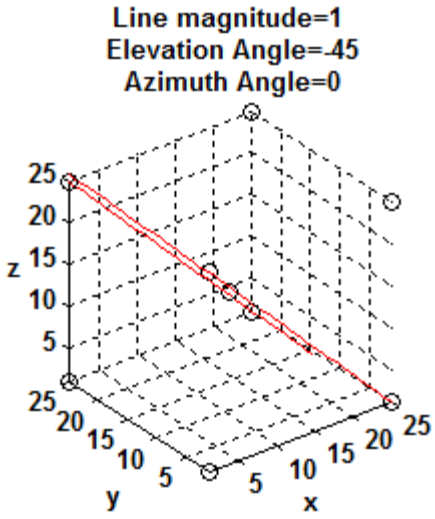
Line magnitude=1
Elevation Angle=-45
Azimuth Angle=0
z
y
x

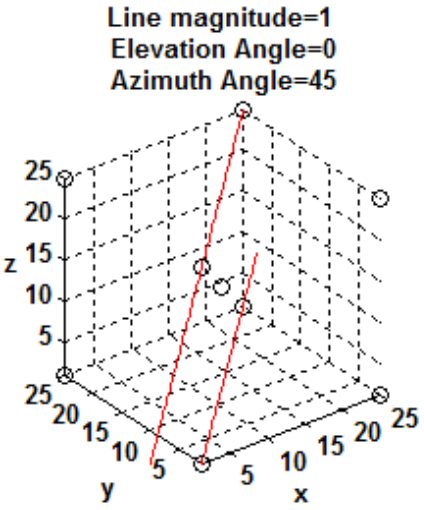
Line magnitude=1
Elevation Angle=0
Azimuth Angle=45
z
y
x

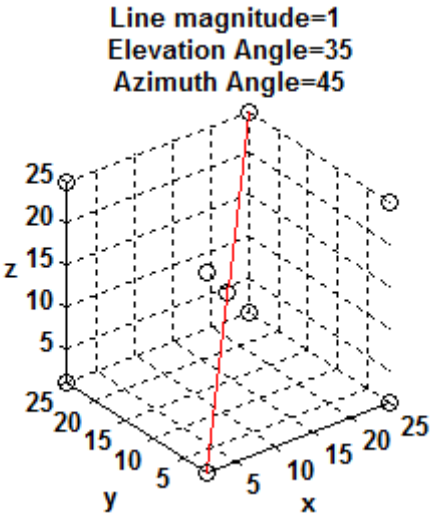
Line magnitude=1
Elevation Angle=35
Azimuth Angle=45
z
y
x

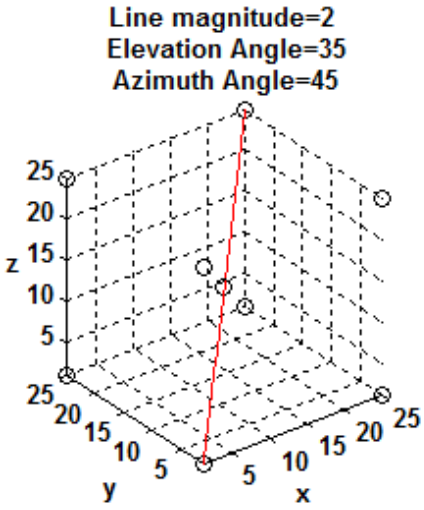
Line magnitude=2
Elevation Angle=35
Azimuth Angle=45
z
y
x

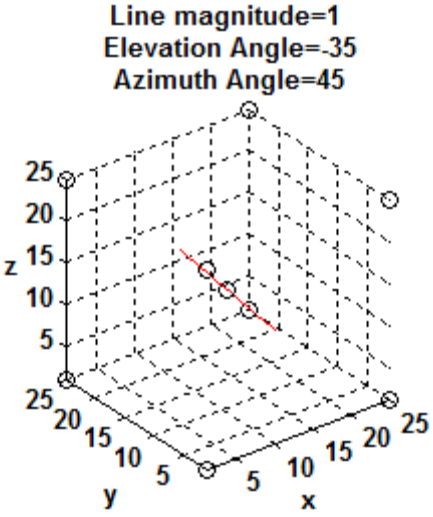
Line magnitude=1
Elevation Angle=-35
Azimuth Angle=45
z
y
x

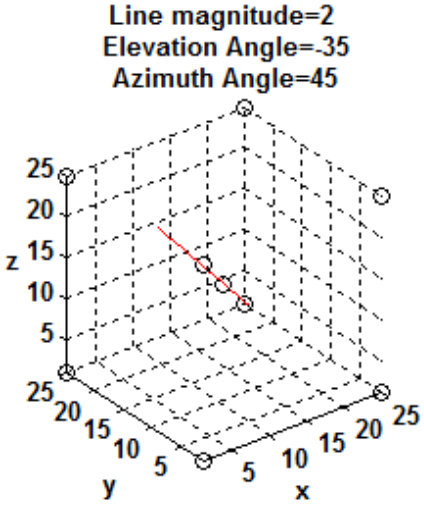
Line magnitude=2
Elevation Angle=-35
Azimuth Angle=45
z
y
x

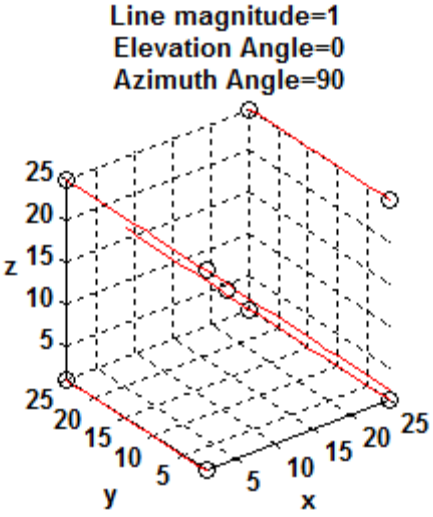
Line magnitude=1
Elevation Angle=0
Azimuth Angle=90
z
y
x

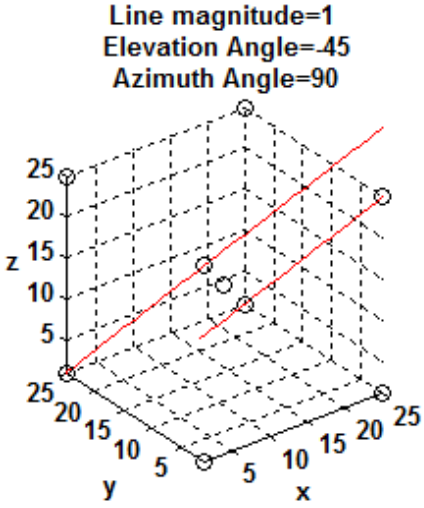
Line magnitude=1
Elevation Angle=-45
Azimuth Angle=90
z
y
x

Line magnitude=1
Elevation Angle=0
Azimuth Angle=135

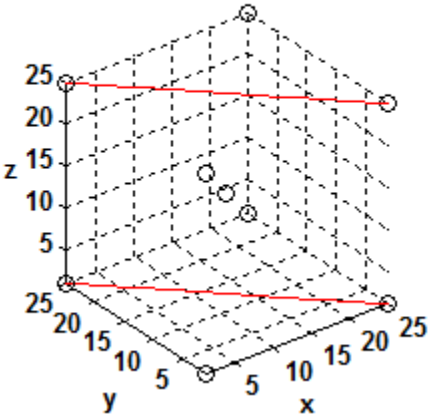

Line magnitude=1
Elevation Angle=35
Azimuth Angle=135

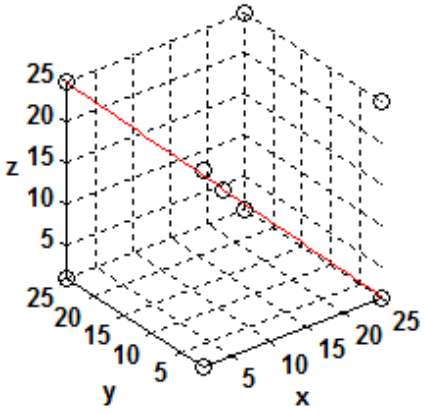

Line magnitude=2
Elevation Angle=35
Azimuth Angle=135

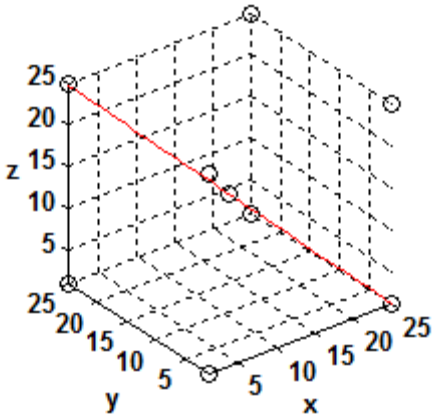

Line magnitude=1
Elevation Angle=-35
Azimuth Angle=135

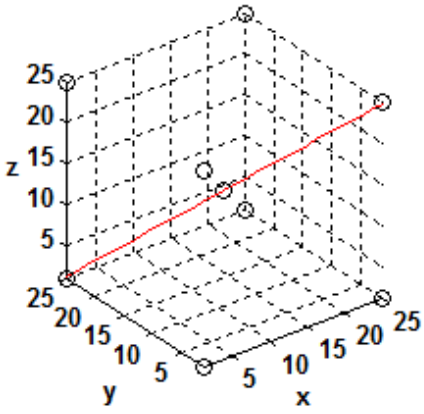

Line magnitude=2
Elevation Angle=-35
Azimuth Angle=135

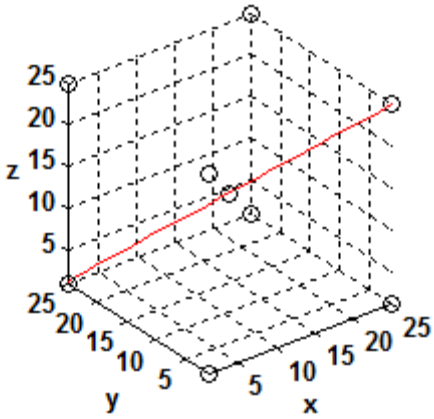

Line magnitude=1
Elevation Angle=0
Azimuth Angle=180

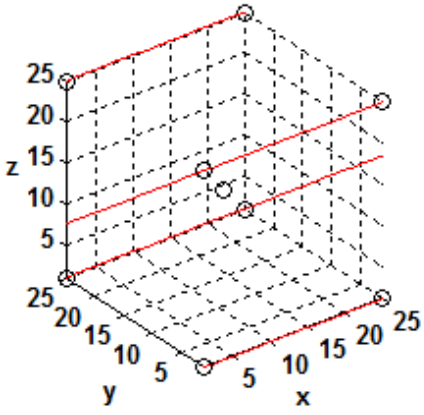

Appendix B

The full set of segmented femur bones using the proposed pressure analogy method.

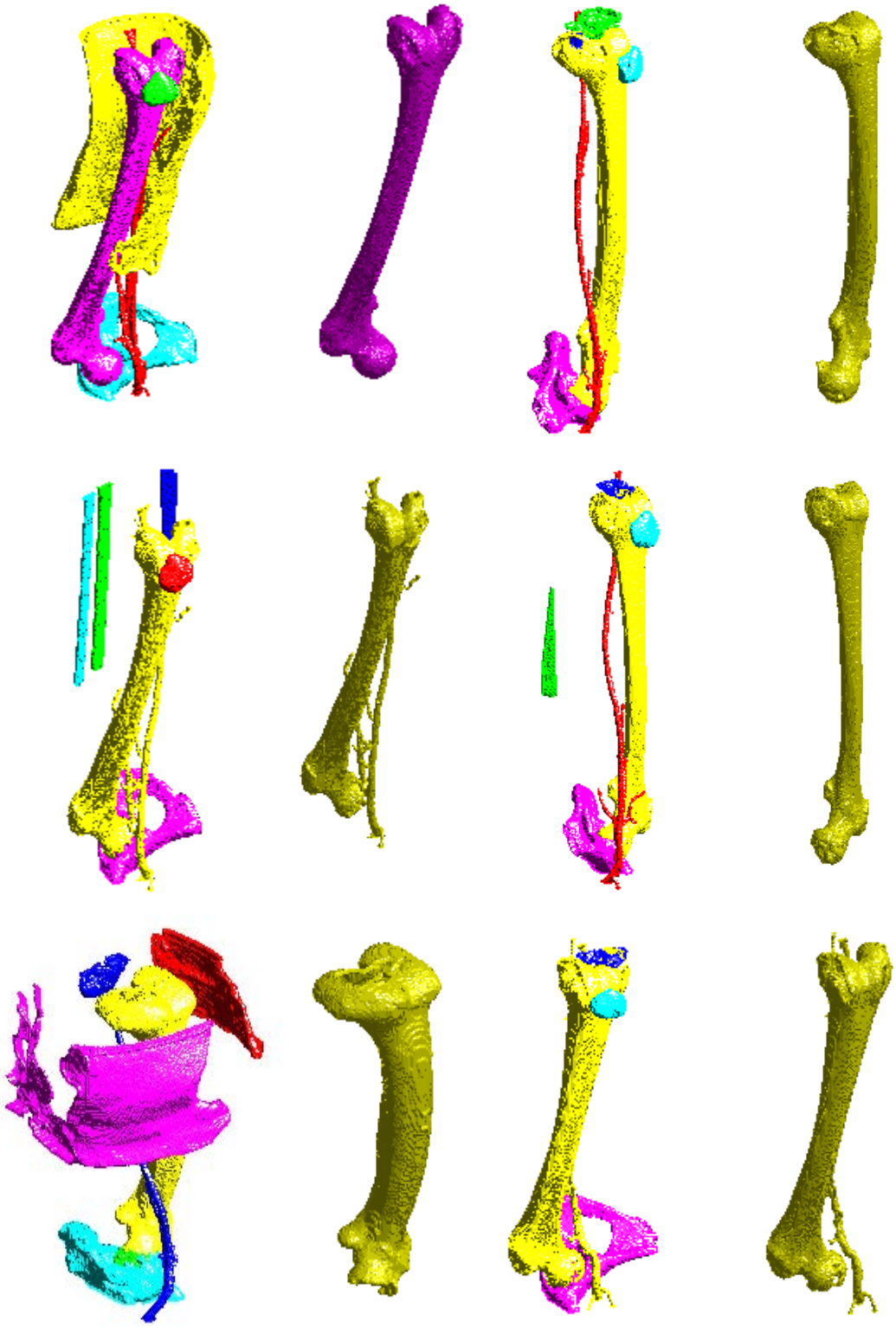

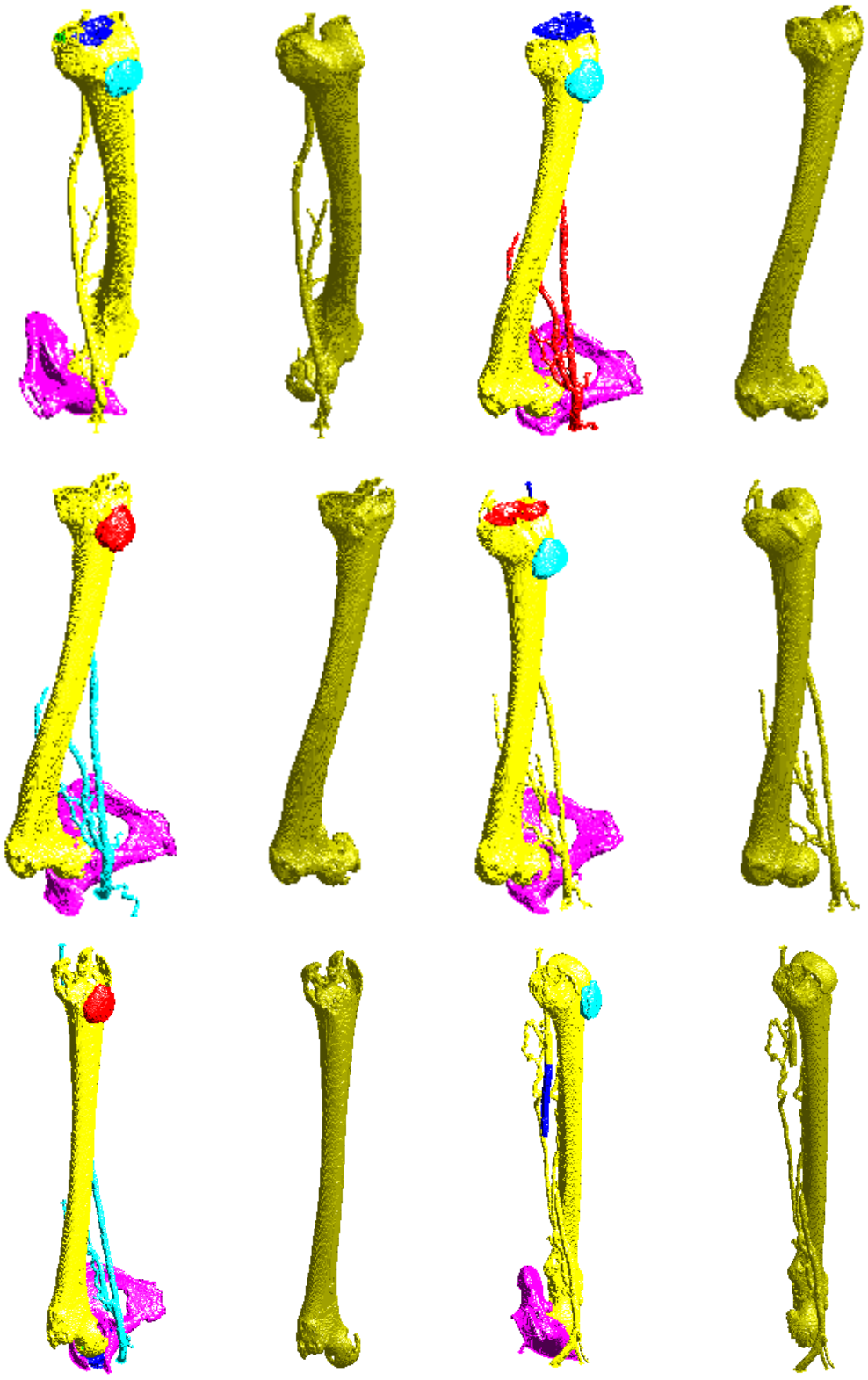

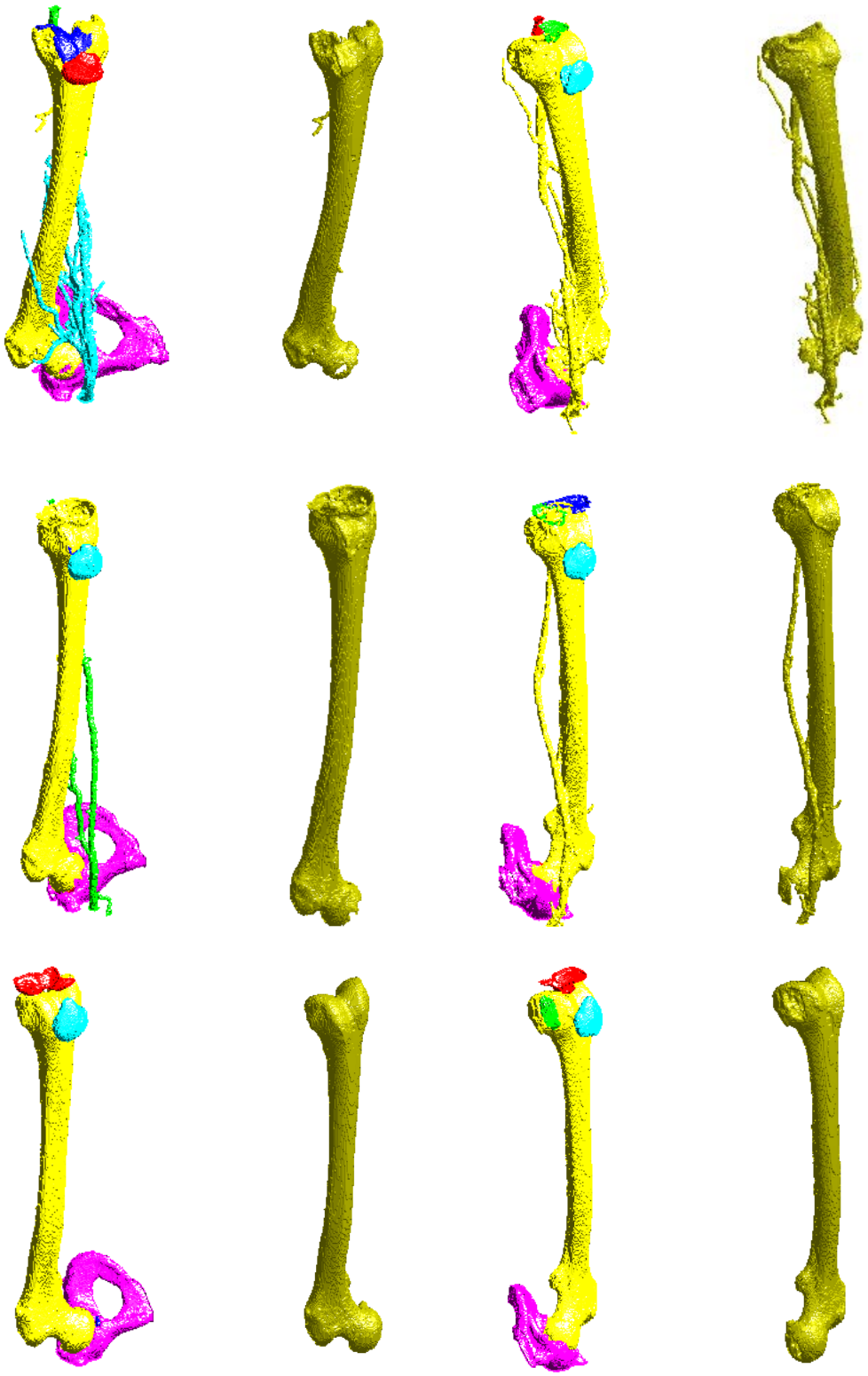

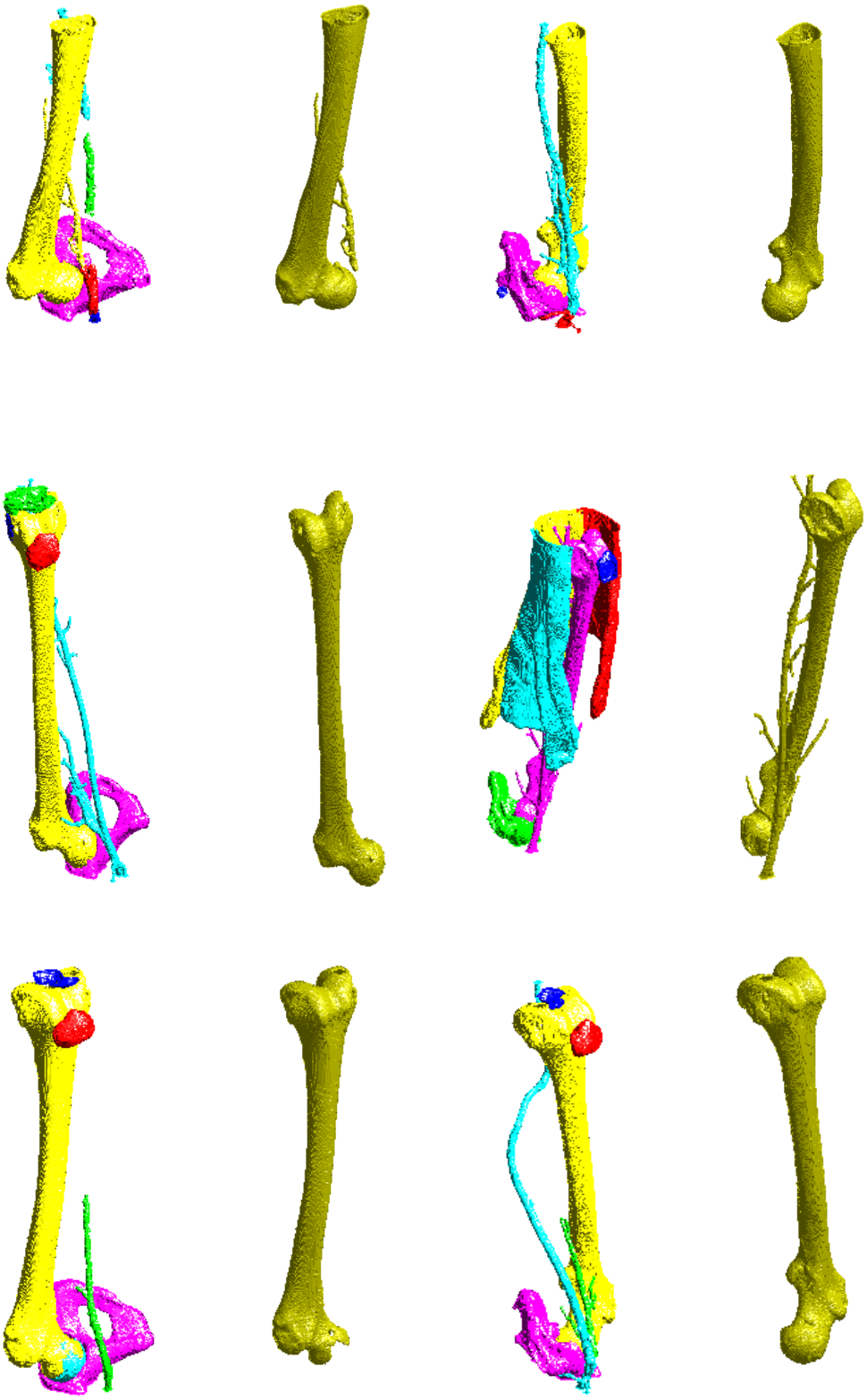

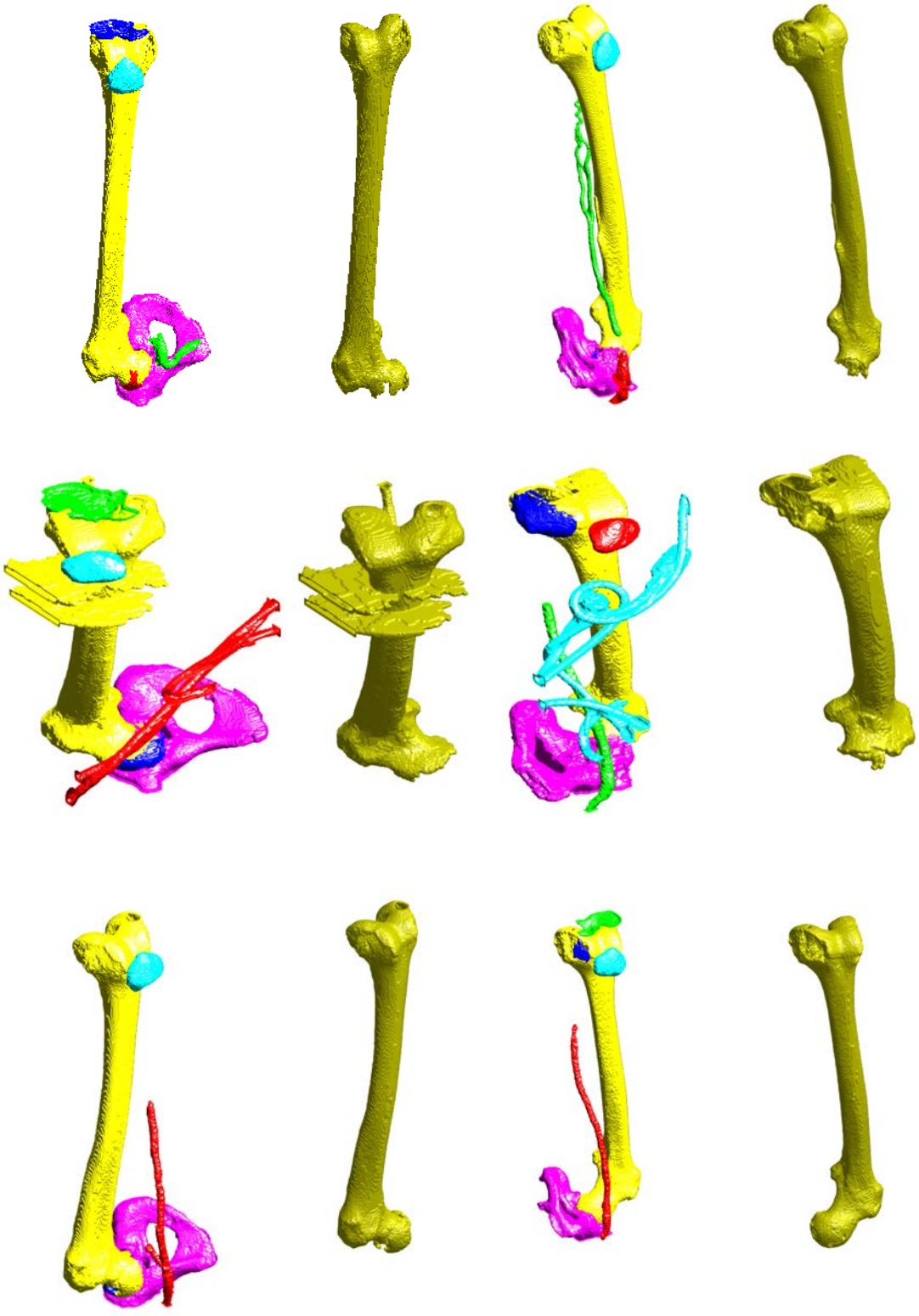

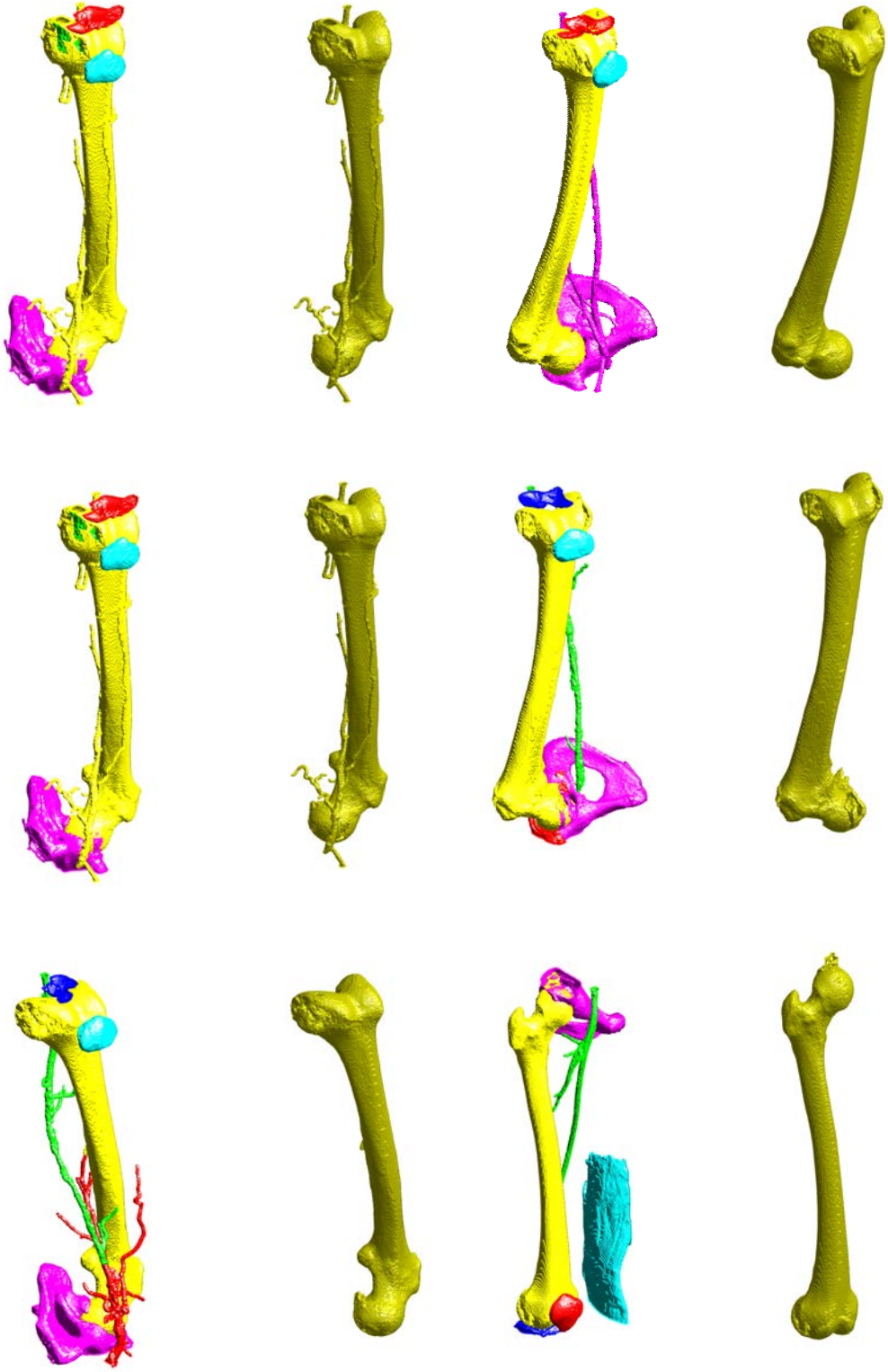

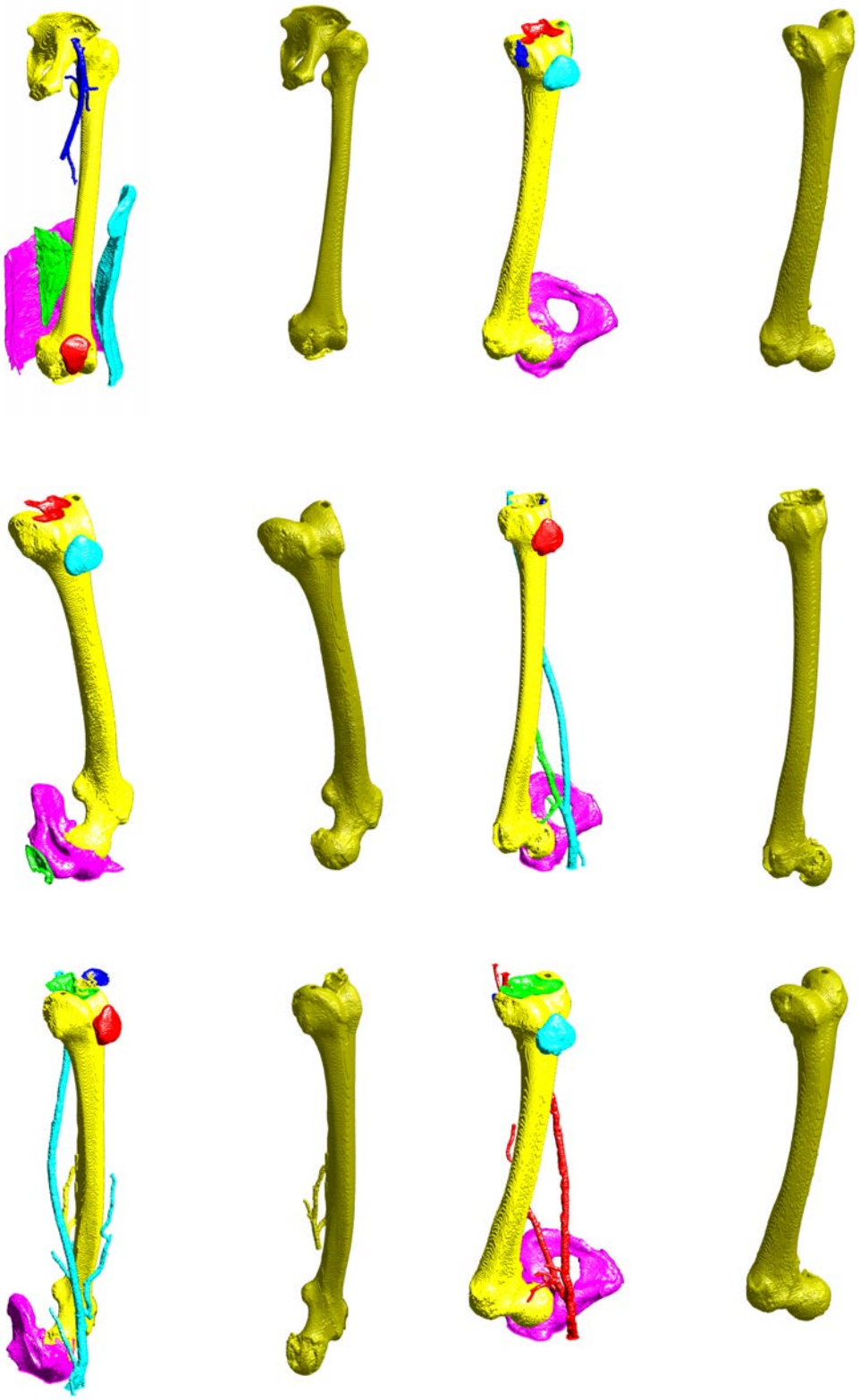

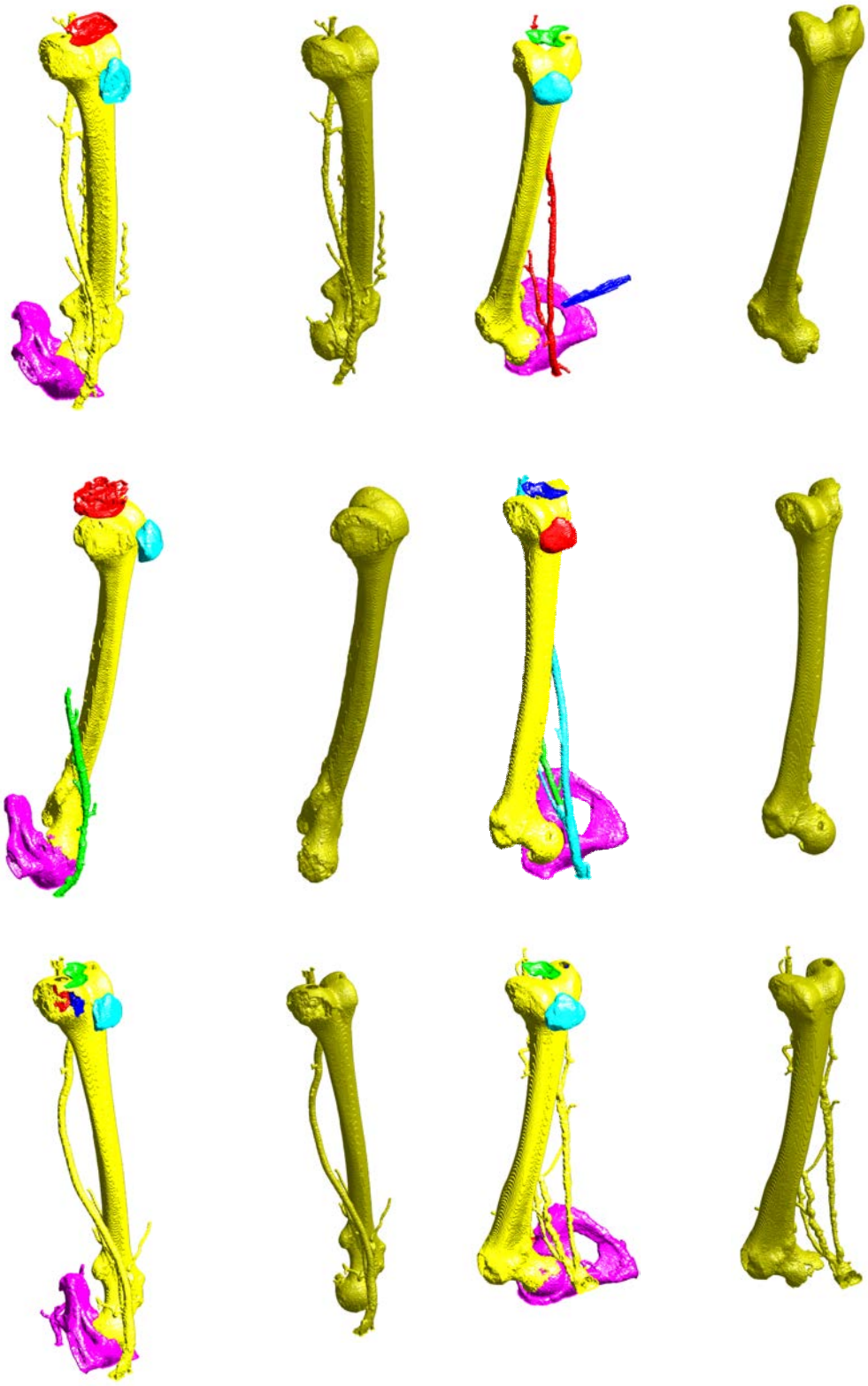

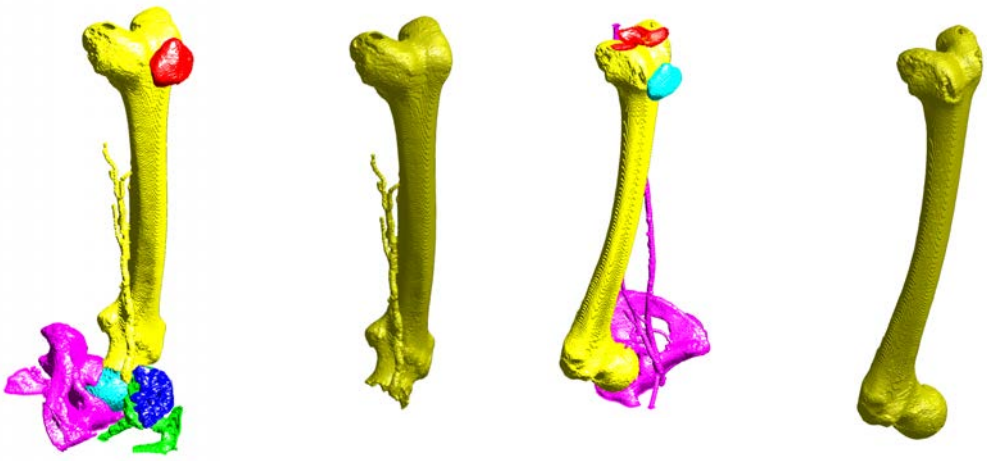

Appendix C

The full set of segmented coins of Figure 1.1 using the proposed pressure analogy of section 4.2.

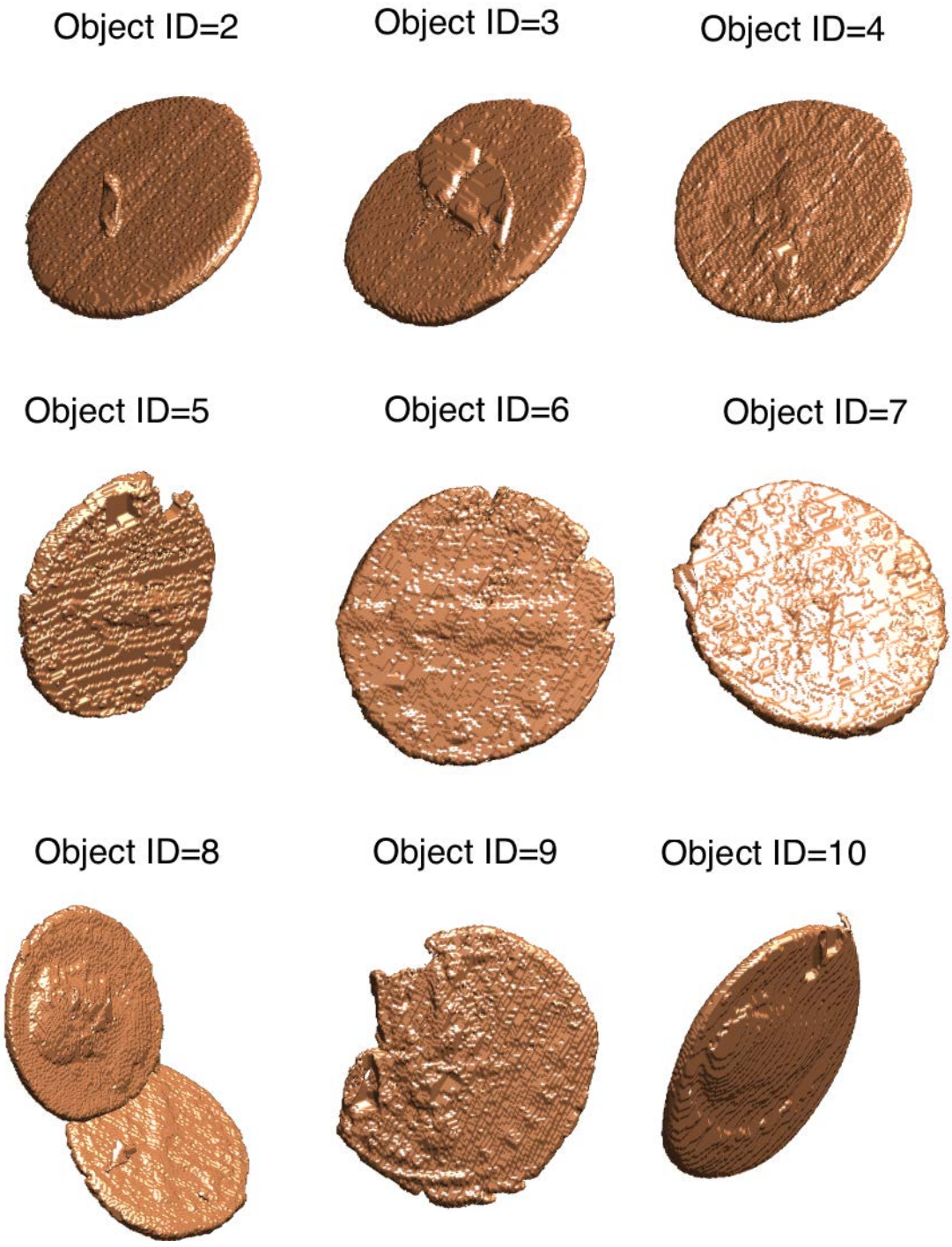

Object ID=11

Object ID=12

Object ID=13

Object ID=14

Object ID=16

Object ID=17

Object ID=19

Object ID=20

Object ID=21

Object ID=24

Object ID=25

Object ID=27

Object ID=29

Object ID=31

Object ID=37

Object ID=39

Object ID=40

Object ID=44

Object ID=46

Object ID=47

Object ID=56

Object ID=62

Object ID=76

Object ID=82

Object ID=83

Object ID=105

Object ID=108

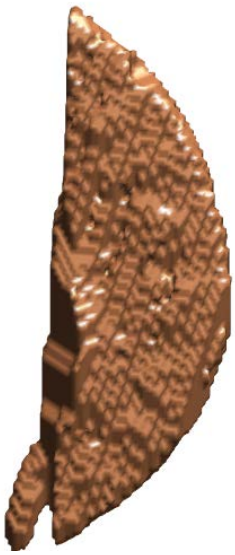

Object ID=134

Object ID=162

Object ID=174

Object ID=194

Object ID=213

Object ID=230

Object ID=235

Object ID=237

Object ID=284

Object ID=293

Object ID=297

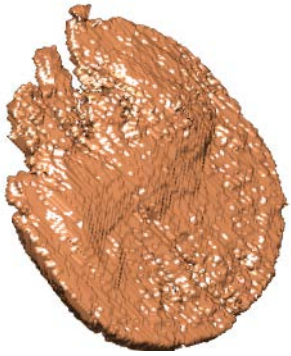

Object ID=299

Object ID=305

Object ID=308

Object ID=314

Object ID=338

Object ID=349

Object ID=357

Object ID=362

Object ID=377

Object ID=397

Object ID=426

Object ID=446

Object ID=504

Object ID=616

Object ID=634

Object ID=638

Object ID=639

Object ID=652

Object ID=667

Object ID=679

Object ID=1

List of References

Abuzaina, A., Alathari, T., Nixon, M. S., & Carter, J. N. (2013). Detecting Moving Spheres in 3d Point Clouds via the 3d Velocity Hough Transform. *11th IEEE IVMSP Workshop : 3D Image/Video Technologies and Applications*.

Alathari, T. S., & Nixon, M. S. (2013). Segmenting Objects in 3d Images by Volumetric Analysis. *Proc. ISVC 2013, LNCS, 8033*, 238–245.

Alathari, T. S., & Nixon, M. S. (2014). Femur Bone Segmentation using a Pressure Analogy. *22nd International Conference on Pattern Recognition*.

Avinash, G. (2009). Volumetric Image Enhancement System and Method. USA.

Babalola, K. O., Patenaude, B., Aljabar, P., Schnabel, J., Kennedy, D., Crum, W., Smith, S., Cootes, T. F., Jenkinson, M., & Rueckert, D. (2008). Comparison and evaluation of segmentation techniques for subcortical structures in brain MRI. *Medical Image Computing and Computer-Assisted Intervention : MICCAI*, *5241*, 409–416.

Ben Younes, L., Nakajima, Y., & Saito, T. (2014). Fully automatic segmentation of the femur from 3D-CT images using primitive shape recognition and statistical shape models. *International Cournal of Computer Assisted Radiology and Surgery*, *9*(2), 189–196.

Bhattacharya, P., Liu, H., Rosenfeld, A., & Thompson, S. (2000). Hough-Transform Detection of Lines in 3-D Space. *Pattern Recognition Letters*, *21*(9), 843–849.

Bomans, M., Hohne, K. H., Tiede, U., & Riemer, M. (1990). 3-D Segmentation of MR Images of The Head For 3-D Display. *IEEE Transactions on Medical Imaging*, *9*(2), 177–183.

Brejl, M., & Sonka, M. (2000). Directional 3D Edge Detection in Anisotropic Data: Detector Design and Performance Assessment. *Computer Vision and Image Understanding*, *77*(2), 84–110.

Camurri, M., Vezzani, R., & Cucchiara, R. (2014). 3D Hough Transform for Sphere Recognition on Point Clouds. *Machine Vision and Applications*, *25*(7), 1877–1891.

Carmo, M. Do. (1976). *Differential Geometry of Curves and Surfaces. Dover phoenix editions* (Vol. 2). Dover Phoenix Editions.

Cong, G., & Parvin, B. (2001). Robust and Efficient Surface Reconstruction from Contours. *The Visual Computer*, *17*(4), 199–208.

Direko, C., & Nixon, M. S. (2006). Low Level Moving-Feature Extraction via Heat Flow Analogy. *Advances in Visual Computing Lecture Notes in Computer Science* (Vol. 4291). Springer, 243–252.

Do Carmo, M. P. (1976). *Differential Geometry of Curves and Surfaces. Dover Phoenix Editions*.

Duda, R. O., & Hart, P. E. (1972). Use of the Hough Transformation to Detect Lines and Curves in Pictures. *Communications of the ACM*, *15*(1), 11–15.

Flitton, G., Breckon, T., & Megherbi, N. (2010). Object Recognition Using 3D SIFT in Complex CT Volumes. *BMVC*, 1–12.

Flitton, G., Mouton, A., & Breckon, T. P. (2015). Object classification in 3D baggage security computed tomography imagery using visual codebooks. *Pattern Recognition*, 1–11.

Franklin, P. (2012). Roman Coins, available at http://www.southampton.ac.uk/engineering/news/2012/07/10_roman_coins.page?

Gao, Y., Wu, L., Mao, Y., & Wang, J. (2014). A Curvature Filter and Normal Clustering Based Approach to Detecting Cylinder on 3D Medical Model. *Advances in Multimedia Information Processing–PCM*, 221–226.

Gonzalez, R., Woods, R., & Eddins, S. (2002). *Digital image processing using MATLAB*. Prentice Hall.

Grau, V., Mewes, a U. J., Alcañiz, M., Kikinis, R., & Warfield, S. K. (2004). Improved watershed transform for medical image segmentation using prior information. *IEEE Transactions on Medical Imaging*, *23*(4), 447–58.

Greig, G., & Klein, F. (1986). Fast contour identification through efficient Hough transform and simplified interpretation strategy. *Proceeding of International Conference: Pattern Recognition*, *1*, 498–500.

Hough, P. V. C. (1962). Method and Means for Recognising Complex Patterns. *US Patent 3,069,654*, *21*, 225–231.

Hu, S., Hoffman, E. a, & Reinhardt, J. M. (2001). Automatic Lung Segmentation for Accurate Quantitation of Volumetric X-Ray CT Images. *IEEE Transactions on Medical Imaging*, *20*(6), 490–498.

Hurley, D. J., Nixon, M. S., & Carter, J. N. (2002). Force Field Energy Functionals for Image Feature Extraction. *Image and Vision Computing* (Vol. 20). Elsevier, 311–317.

Illingworth, J., & Kittler, J. (1987). The Adaptive Hough Transform. *IEEE Transactions on Pattern Analysis and Machine Intelligence*, *9*(5), 690–698.

Itk.org (2014). Sobel Operator, available at http://www.itk.org/Doxygen/html/classitk_1_1SobelOperator.html.

Kass, M., Witkin, A., & Terzopoulos, D. (1988). Snakes: Active Contour Models. *International Journal of Computer Vision*, *1*(4), 321–331.

Kaus, M., Warfield, S., Nabavi, A., Chatzidakis, E., Black, P., Jolesz, F., & Kikinis, R. (1999). Segmentation of meningiomas and low grade gliomas in MRI. *Medical Image Computing and Computer-Assisted Intervention–MICCAI*, *1679*, 1–10.

Kimme, C., Ballard, D., & Sklansky, J. (1975). Finding Circles by an Array of Accumulators. *Communications of the ACM*, *18*(2), 120–122.

Knopp, J., Prasad, M., Willems, G., Timofte, R., & Van Gool, L. (2010). Hough Transform and 3D SURF for Robust Three Dimensional Classification.

Proceedings of the 11th European Conference on Computer Vision. Berlin, Heidelberg: Springer, 589–602.

Krcah, M., Szekely, G., & Blanc, R. (2011a). Fully Automatic and Fast Segmentation of the Femur Bone from 3D-CT Images with no Shape Prior. *2011 IEEE International Symposium on Biomedical Imaging: From Nano to Macro*. IEEE, 2087–2090.

Krcah, M., Szekely, G., & Blanc, R. (2011b). Fully Automatic and Fast Segmentation of The Femur Bone from 3D-CT Images with No Shape Prior. *IEEE International Symposium on Biomedical Imaging: From Nano to Macro*, 2087–2090.

Lam, L., Lee, S.-W., & Suen, C. Y. (1992). Thinning Methodologies-A Comprehensive Survey. *IEEE Transactions on Pattern Analysis and Machine Intelligence*, *14*(9), 879.

Liu, X. U., & Nixon, M. S. (2006). Water Flow Based Complex Feature Extraction. *Advances in Visual Computing Lecture Notes in Computer Science* (Vol. 4179). Springer, 833–845.

Lohmann, G. (1994). *Volumetric Image Analysis*.

Ma, Z., Tavares, J. M. R. S., Jorge, R. N., & Mascarenhas, T. (2010). A Review of Algorithms for Medical Image Segmentation and Their Applications to the Female Pelvic Cavity. *Computer Methods in Biomechanics and Biomedical Engineering*, *13*(2), 235–246.

Meyer, F. (1994). Topographic Distance and Watershed Lines. *Signal Processing*, *38*(1), 113–125.

Muvis. (2014). *MuVis at University of Southampton*.

Nasr-Isfahani, S., Mirsafian, A., & Masoudi-Nejad, A. (2008). A New Approach for Touching Cells Segmentation. *International Conference on BioMedical Engineering and Informatics*. IEEE, 816–820.

Nixon, M., & Aguado, A. (2012). *Feature Extraction and Image Processing*. Academic Press.

Nixon, M. S., Liu, X. U., Direko, C., & Hurley, D. J. (2009). On Using Physical Analogies for Feature and Shape Extraction in Computer Vision. *The Computer Journal*, 1–15.

Nixon, M. S., Liu, X. U., Direkoglu, C., & Hurley, D. J. (2009). On Using Physical Analogies for Feature and Shape Extraction in Computer Vision. *The Computer Journal*, *54*(1), 11–25.

Ogundana, O. O., Coggrave, C. R., Burguete, R. L., & Huntley, J. M. (2007). Fast Hough Transform for Automated Detection of Spheres in Three-Dimensional Point Clouds. *Optical Engineering*, *46*(5), 051002.

Otsu, N. (1979). A Threshold Selection Method from Gray-Level Histograms. *IEEE Transactions on Systems, Man, and Cybernetics*, *9*(1), 62–66.

Overby, J., Bodum, L., Kjems, E., & Iisoe, P. (2004). Automatic 3D Building Reconstruction from Airborne Laser Scanning and Cadastral Data Using Hough Transform. *International Archives of ….*

Palu, A., He, J., & Lu, Y. (2006). Identification of Alpha-Helices from Low Resolution Protein Density Maps. *Computational Systems Bioinformatics Conference*, 89–98.

Pettersson, J., Knutsson, H., & Borga, M. (2006). Automatic Hip Bone Segmentation Using Non-Rigid Registration. *18th International Conference on Pattern Recognition (ICPR'06)*, 946–949.

Rabbani, T., & Heuvel, F. Van Den. (2005). Efficient Hough Transform for Automatic Detection of Cylinders in Point Clouds. *ISPRS WG III/3, III/4*, *3*, 60–65.

Russ, J. C. (2006). *The Image Processing Handbook, Fifth Edition*. CRC Press.

Sarti, A., & Tubaro, S. (2002). Detection and Characterisation of Planar Fractures using a 3D Hough Transform. *Signal Processing*, *82*(9), 1269–1282.

Schmid, J., Kim, J., & Magnenat-Thalmann, N. (2011). Robust Statistical Shape Models for MRI Bone Segmentation in Presence of Small Field of View. *Medical Image Analysis*, *15*(1), 155–168.

Seim, H., Kainmueller, D., & Heller, M. (2008). Automatic Segmentation of the Pelvic Bones from CT Data Based on a Statistical Shape Model. *VCBM*, 93–100.

Sobel, I. (1970). *Camera Models and Machine Perception*. Palo Alto, CA: Stanford Artificial Intelligence Lab.

Sobel, I. (2014a). History of Sobel operator.

Sobel, I. (2014b). *History and Definition of the Sobel Operator*.

Sørensen, T. (1948). A Method of Establishing Groups of Equal Amplitude in Plant Sociology Based on Similarity of Species and its Application to Analyses of the Vegetation on Danish Commons. *Biol. Skr.*, *5*, 1–34.

Stevens, K. (1981). The Visual Interpretation of Surface Contours. *Artificial Intelligence*, *17*(1), 47–73.

Su, Y., & Bethel, J. (2010). Detection and Robust Estimation of Cylinder. *ASPRS Conference*.

Wählby, C., & SINTORN, I. (2004). Combining Intensity, Edge and Shape Information for 2D and 3D Segmentation of Cell Nuclei in Tissue Sections. *Journal of Microscopy*, *215*, 67–76.

Wang, X., Gillibert, L., Flin, F., & Coeurjolly, D. (2012). Curvature-driven Volumetric Segmentation of Binary Shapes: an Application to Snow Microstructure Analysis. *Pattern Recognition (ICPR), 2012 21st International Conference on*, 742–745.

Wikipedia (2012). Sobel Operator, available at http://en.wikipedia.org/wiki/Sobel_operator.

Wirjadi, O. (2007). *Survey of 3d image segmentation methods. Technical report No. 123, Fraunhofer ITWM, Kaiserslautern* (Vol. 123). Germany.

Yao, Q., Zhou, Y., & Wang, J. (2010). An Automatic Segmentation Algorithm for Touching Rice Grains Images. *International Conference on Audio, Language and Image Processing*, 802–805.

Yokota, F., Okada, T., Takao, M., Sugano, N., Tada, Y., & Sato, Y. (2009). Automated Segmentation of The Femur and Pelvis from 3D CT Data of Diseased Hip Using Hierarchical Statistical Shape Model of Joint Structure. *Medical Image Computing and Computer-Assisted Intervention–MICCAI 2009*. Springer Berlin Heidelberg, 811–818.

Yu-Qian, Z., Wei-Hua, G., Zhen-Cheng, C., Jing-Tian, T., & Ling-Yun, L. (2005). Medical Images Edge Detection Based on Mathematical Morphology. *27th Annual International Conference of the Engineering in Medicine and Biology Society (IEEE-EMBS)* (Vol. 6), 6492–6495.

Zhang, J., Yan, C.-H., Chui, C.-K., & Ong, S.-H. (2010). Fast Segmentation of Bone in CT Images Using 3D Adaptive Thresholding. *Computers in Biology and Medicine*, *40*(2), 231–236.

Zhang, Y. J. (1993). Quantative Study of 3D Gradient Operators. *Image and Vision Computing*, *11*(10).

Zhou, H., Qiu, W., Ding, M., & Zhang, S. (2008). Automatic Needle Segmentation in 3D Ultrasound Images Using 3D Improved Hough Transform. M. I. Miga & K. R. Cleary (Eds.), *Medical Imaging. International Society for Optics and Photonics* (Vol. 6918), 691821–691821.

Zhu, Y.-M., Cochoff, S. M., & Sukalac, R. (2012). Automatic Patient Table Removal in CT Images. *Journal of Digital Imaging : the Official Journal of the Society for Computer Applications in Radiology*, *25*(4), 480–485.

Zoroofi, R. a, Sato, Y., Sasama, T., Nishii, T., Sugano, N., Yonenobu, K., Yoshikawa, H., Ochi, T., & Tamura, S. (2003). Automated Segmentation of Acetabulum and Femoral Head from 3-D CT Images. *IEEE Transactions on Information Technology in Biomedicine*, *7*(4), 329–343.